DISSERTATION

Radial velocity modulation of an outer star orbiting an unseen inner binary: analytic perturbation formulae in a three-body problem to search for wide-separation black-hole binaries

(不可視連星を公転する恒星の視線速度変動：
三体問題における解析的摂動公式を用いた
長周期連星ブラックホール探査)

林 利憲

A thesis submitted to
the graduate school of science,
the University of Tokyo
in partial fulfillment of
the requirements for the degree
of
Master of Science in Physics

January, 2019

Abstract

Since the discovery of close-in binary black hole with LIGO, the origin and evolution of such systems are active research fields in astrophysics. Current formation scenarios usually require long-term evolution to achieve coalescence. It implies the presence of numerous wide-separation binary black holes as progenitors of LIGO's black hole analogs. However, the existence of this new population is not yet clear observationally. Both gravitational wave and direct photometry observations have difficulty in identifying this kind of systems since they are expected to have neither detectable gravitational wave signals nor electromagnetic radiations.

In this thesis, as a possible methodology, we propose a new approach to search for wide-separation binary black holes with radial velocity modulation of the outer star. Following the perturbation theory for a hierarchical three-body problem in celestial mechanics, we derive analytic approximation formulae to describe the motion of outer objects orbiting around an unseen inner binary, including wide-separation binary black holes. For simplicity, the formulation in this thesis focuses on a triple system with coplanar and near-circular orbits. This treatment clarifies the origin and characters of expected observation signals. Although it is for very ideal situations, the currnet observations imply the presence of such systems. There are a few known systems relevant for our model; 2M05215658+4359220 and PSR J0337+1715. These formulae can provide a directly applicable tool for this class of objects.

In order to confirm the validity, we compare the approximate formulae with N-body numerical simulation. Although these formulae are expected to be applicable for a variety of observational data, we particularly consider radial velocity as a specific example. We derive the approximate radial velocity formula of outer body and examine it with numerical simulation. As a practical application, we derive a constraint on an unseen companion inside a binary system 2M05215658+4359220 recently discovered through the radial velocity observation. This constraint reveals that if the unseen bodies constituting an inner binary have roughly equal masses, even the current data could exclude the inner binary with more than 12.5 day orbital period. Future radial velocity follow-up observation will either strengthen the constraint or even detect a signature of the inner binary.

Since *Gaia* and *TESS* are expected to find many binary systems with unseen companions in near future, this radial velocity formulae may be useful to either put a constraint on these or estimate radial velocity modulations before real follow-up observation. The detection of wide-separation binary black hole will contribute to the formation theory currently proposed. Finally, we discuss outlook and future prospects.

Contents

Chapter 1

Introduction

The first direct detection of a gravitational wave (GW) from a binary black-hole (BBH) merger (Abbott et al. 2016) has convincingly established the presence of very compact BBHs in the universe. The origin, evolution and distribution of such BBHs are hardly understood, but several scenarios have already been proposed. The isolated binary evolution scenario (e.g. Belczyński & Bulik 1999; Belczynski et al. 2012, 2016, 2002, 2007; Dominik et al. 2012, 2013; Kinugawa et al. 2014, 2016) considers that massive stars like Pop III stars are formed as binary systems, experience supernovae, and finally evolve into compact binaries including binary black holes. The dynamical formation scenario (e.g. O'Leary et al. 2009, 2006; Portegies Zwart & McMillan 2000; Rodriguez et al. 2016; Tagawa et al. 2016) considers that black holes in dense star clusters experience significant gravitational interactions and binary black holes can be formed due to occasional capture. The primordial origin scenario (e.g. Bird et al. 2016; Sasaki et al. 2016, 2018) proposes that abundant primordial black holes are formed in a very early universe and they finally interacts each other and form binary black holes through GW emission.

Regardless of such different formation scenarios, however, there should be abundant progenitor BBHs with wider separations and thus longer orbital periods. Detection of such unseen BBHs will not only constrain the formation and evolutionary channel towards the GW emitting BBHs, but also establish a yet unknown species of astrophysical objects.

Those BBHs do not generate a detectable GW signal until a few seconds before the final merger. Also they are difficult to be detected directly unless they are surrounded by appreciable accretion disks. Therefore, the presence of such unseen binaries have to be searched for through their dynamical influence on nearby visible objects.

Indeed there are a couple of examples that are relevant for such a strategy. One is a triple system consisting of a white dwarf-pulsar binary and an outer white dwarf orbiting around the inner binary (Ransom et al. 2014). The system was detected with the arrival time analysis of the pulsar. Quite interestingly, the inner and outer orbits of the triple system are near-circular and coplanar; the eccentricities of the inner and outer orbits are $e_{\rm in} \sim 6.9 \times 10^{-4}$ and $e_{\rm out} \sim 3.5 \times 10^{-2}$, and their mutual inclination is $i = (1.20 \pm 0.17) \times 10^{-2}$ deg.

The other is a red giant 2M05215658+4359220 with an unseen massive object, possibly a black hole (Thompson et al. 2018). The system was discovered from a systematic survey of stars exhibiting anomalous accelerations. The follow-up radial-velocity (RV) observation indicates that the orbit is also near-circular; $e_{\rm out} = 0.00476 \pm 0.00255$.

The two examples are very encouraging, implying that the dynamical search for unseen companions of visible objects is very rewarding, and even that a near-circular outer object with a near-circular and coplanar inner binary really exists.

Indeed there are several on-going/future projects that search for unseen companions around stars. *Gaia* was launched at the end of 2013, and is performing astrometric survey for about billion of stars in the Galaxy. Since the astrometry of *Gaia* has great astrometric precision especially for bright stars, it can detect a subtle motion of a star around an unseen object. There are many proposals to search for star – black hole binaries with *Gaia* (e.g. Breivik et al. 2017; Kawanaka et al. 2017; Mashian & Loeb 2017; Yamaguchi et al. 2018). Yamaguchi et al. (2018), for instance, estimate that *Gaia* can detect $200 - 1000$ binaries in 5 year operation.

TESS launched in 2018 is carrying out photometric surveys of near-by stars to search for transit planets. Masuda & Hotokezaka (2018) propose that *TESS* will potentially discover $\sim 10^3$ binaries consisting of a star and an unseen compact object through identifying a relativistic effect in their photometric light-curves.

Thus it is quite likely that *Gaia*, *TESS* and other surveys detect numerous binary systems with an unseen object. Given the LIGO discovery of very tight BBHs, it is natural to expect that a fraction of those systems are indeed triple systems that host unseen inner BBHs. Therefore it is important to see if one can distinguish dynamically between a single black hole and a binary black hole in such triple systems. For that purpose, we consider the orbital evolution of an outer visible body in a near-circular and coplanar triple system. While this is a fairly idealized system, there exists at least one system as we mentioned in the above. Also we can approach the dynamics of the system analytically by applying a perturbation theory in the hierarchical three-body problem. This provides a good physical insight on the dynamical behavior of such systems, and also puts preliminary constraints on the parameter space before performing an intensive numerical study to unambiguously identify the inner BBHs.

The rest of this thesis is organized as follows. Chapter 2 summarizes the current observational reports on the binary and triple systems relevant to our study. The summary of each formation scenario and observing proposals with *Gaia* and *TESS* is also described in Chapter 2. Chapter 3 summarizes the theoretical background for the research in this thesis. Chapter 4 describes the formulation of the three-body problem that we adopted, and derives the basic perturbation equations. Here, we also present the approximate analytic solutions and comparison of them against the result from numerical simulation. Chapter 5 applies our analytic formulae to put a constraint on a possible unseen binary inside 2M05215658+4359220 reported in Thompson et al. (2018), and discusses the validity of the approximation using numerical simulations. Finally, Chapter 6 is devoted to the summary of result and discussion about future

prospects. Appendices are added in order not to disturb the main part of this thesis. They summarize the Hansen coefficients, variation of constants method, and show the full comparison of perturbation and numerical solutions on a term-by-term basis.

Chapter 2

Examples of observed compact binaries and triples

2.1 Examples of observed compact binary and triple systems

LIGO's discovery of close-in binary black hole strongly implies the presence of wide-separation ones as progenitors although they are not yet discovered. As mentioned in Chapter 1, this thesis concerns a system consisting of an outer star and inner unseen binary, and develops a possible methodology to search for wide-separation unseen binaries via radial velocity modulations of outer star. Thus, the presence of such systems should be the key issue in the practical application of this methodology.

Indeed, some systems implying the existence of them have already been announced although the number is currently quite limited. In this section, we briefly summarize a few examples for compact binary and triple systems. Figure 2.1 shows schematic illustrations of the binary and triple systems we summarize in this section.

2.1.1 A binary black hole merger GW150914

First, we have a look at the discovery of close-in binary black hole with LIGO since it first motivates the research in this thesis. In 2016, Abbott et al. (2016) reported the first detection of gravitational wave event GW150914 from a binary black hole merger with the Laser Interferometer Gravitational-Wave Observatory (LIGO). LIGO consists of two observatories at Hanford, WA, and Livingston, LA, to detect gravitational waves using laser interferometers. On the 14th of September in 2015, the detectors at two observatories coincidently detected the gravitational wave signals GW150914. After matched-filter analyses using relativistic models of compact binary waveforms, they can reproduce the strains due to GW150914 projected onto each detector.

GW150914 signals have the feature that both frequency and amplitude increase with time and show a sudden disappearance later. The frequency of signals f changes from 35 Hz to 150 Hz over the time duration of 0.2 sec. Considering this feature, they

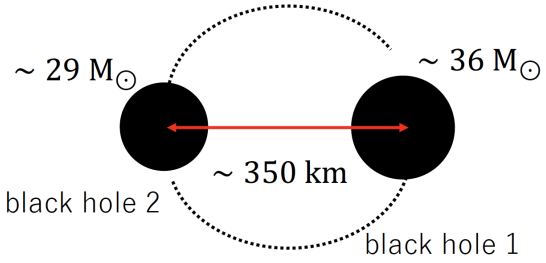

(a)

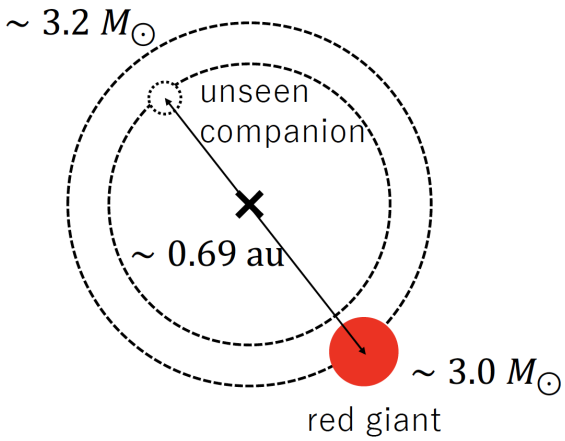

(b)

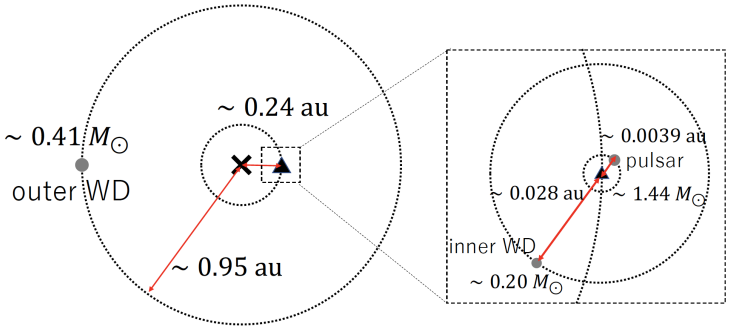

(c)

Figure 2.1: Schematic illustrations of observed binary and triple systems. The crosses denote the centre of mass of the system. The triangles denote the centres of mass of the inner binary: (a) binary black hole merger GW150914, (b) binary system 2M05215658+4359220 including an unseen companion, (c) triple system PSR J0337+1715 consisting of an white dwalf - pulsar inner binary and outer white dwarf.

conclude that GW150914 is likely due to coalescence of two black holes. The whole scenario they propose is as follows. Due to the loss of the orbital energy via gravitational wave emission, the orbit of binary black hole shrinks and exhibits inspiral motion. During this phase, its orbital separation decreases drastically and gravitational wave emission is highly enhanced and becomes detectable with LIGO. Then, two black holes collide each other and this merger event is reflected in the signals as strong strains. After that, a spinning single black hole is formed and the gravitational wave signals are decaying immediately.

With this scenario in mind, they first try to estimate the mass of each black hole by computing the charp mass. The charp mass $\mathcal{M}$, which is known to well characterize the merger event at lower frequencies, is defined as

$$\mathcal{M} \equiv \frac{(m_1 m_2)^{\frac{3}{5}}}{(m_1+m_2)^{\frac{1}{5}}} = \frac{c^3}{G}\left[\frac{5}{96}\pi^{-\frac{8}{3}} f^{-\frac{11}{3}} \dot{f}\right]^{\frac{3}{5}}, \tag{2.1}$$

where m_1 and m_2 are the masses of two black holes, c is the speed of light, G is the gravitational constant, and f is the frequency of signals. They find that ~ 30 $\mathrm{M}_\odot$ charp mass explain the data well. Using equation (2.1) and the inequality between the arithmetic and geometric means:

$$\mathcal{M} \equiv \frac{(m_1 m_2)^{\frac{3}{5}}}{(m_1+m_2)^{\frac{1}{5}}} \leq \frac{1}{4^{\frac{3}{5}}}(m_1+m_2) \approx \frac{1}{2.3}(m_1+m_2). \tag{2.2}$$

Thus, $\sim 30\ M_\odot$ charp mass reveals the total mass of system $m_1+m_2 \gtrsim 70$ $\mathrm{M}_\odot$. Besides, they find that the separation of the two black holes ~ 350 km when $f \sim 150$ Hz.

Then, they proceed a detail parameter survey using about 250000 template wave forms to find the best-fit values of parameters specifying the system. The parameter sets cover individual masses from 1 to 99 $\mathrm{M}_\odot$, total mass less than 100 $\mathrm{M}_\odot$, and dimensionless spins up to 0.99. The dimensionless spin is defined as the ratio between a spin angular momentum of a spinning black hole and maximum spin of it above which a naked singularity appears. As template waveforms, they use the effective-one-body formalism, which combine the post-Newtonian approach with results from black hole perturbation theory and numerical relativity. Table 2.1 lists the best-fit parameters they found from this procedure.

This discovery has a huge impact on formation theory of such systems. Some scenarios have already been proposed (e.g. Belczynski et al. 2012, 2016, 2002, 2007; Bird et al. 2016; Dominik et al. 2012, 2013; Kinugawa et al. 2014, 2016; O'Leary et al. 2009; Portegies Zwart & McMillan 2000; Rodriguez et al. 2016; Sasaki et al. 2016, 2018; Tagawa et al. 2016) and expect long-time dynamical evolution before an orbit shrinks and finally reaches coalescence. This fact proposes that there should be many wide-separation binary black holes as progenitors of GW150914 analogs. Although LIGO has a great precision within the range around 1 - 1000 Hz, the gravitational waves from wide-separation ones are expected to be significantly weaker and have lower frequency than ~ 1 Hz. For example, if orbital period of such a binary is ~ 10 days, the

parameter	value
Primary black hole mass m_1	36^{+5}_{-4} $M_\odot$
Secondary black hole mass m_2	29^{+4}_{-4} $M_\odot$
Final black hole mass	62^{+4}_{-4} $M_\odot$
Final black hole spin	$0.67^{+0.05}_{-0.07}$
Luminosity distance	410^{+160}_{-180} Mpc
Source redshift z	$0.09^{+0.03}_{-0.04}$

Table 2.1: Best-fit parameters for GW150914 with 90% credible intervals. Masses are given in the source frame. Adapted from Abbott et al. (2016)

expected frequency is only $\sim 10^{-6}$ Hz. Therefore, it may be difficult to observe them with the current gravitational wave detectors. Without electromagnetic radiation from the matter surrounding black holes, direct observation is also impossible. This fact motivates us to develop an alternative method to search for them.

2.1.2 A binary system 2M05215658+4359220

Second, we move to the discovery of a near-circular binary system containing an unseen object. This discovery is important bacause such systems can be realistic candidates to apply our methodology to search for unseen binaries. Many researchers (e.g. Breivik et al. 2017; Kawanaka et al. 2017; Mashian & Loeb 2017; Masuda & Hotokezaka 2018; Yamaguchi et al. 2018) propose that binary systems consisting of a star and black hole should exist and can be observed with *Gaia* and *TESS*. The discovery of a binary system 2M05215658+4359220 is also important as the first sucsessful example.

In 2018, Thompson et al. (2018) report the discovery of a binary system consisting of a red giant and unseen companion by combining radial velocity and photometric variation data. They claim that a large collection of binary systems with compact objects provides good observational data for study on binary stellar evolution models.

They start to search for binary systems with massive unseen companions using the radial velocity data from the Apache Point Observatory Galactic Evolution Experiment (APOGEE). APOGEE performs near-infrared spectroscopic observation for more than 10^5 stars in the Galaxy, providing the radial velocity data useful to search for the anomalies due to binary motion. The radial velocity anomalies from APOGEE are useful to pick up possible binaries with unseen companions among huge amount of stars, although follow-up observations are required to confirm the binaries. They first calculated the maximum acceleration $a_{\max}$ for each system using APOGEE data:

$$a_{\max} \equiv \max\left(\frac{\Delta \mathrm{RV}}{\Delta t_{\mathrm{RV}}}\right), \tag{2.3}$$

where ΔRV is the difference between two subsequent radial velocity data, and Δt_{RV} is the time interval of two observations. This quantity is useful to determine candidates since large acceleration implies the presence of massive object in system. Using

JD-2450000	Absolute RV(km/s)	Uncertainty(km/s)
6204.9537	−37.417	0.011
6229.9213	34.846	0.010
6233.8732	42.567	0.010

Table 2.2: Radial velocity measurements for 2M05215658+4359220 from APOGEE. Adapted from Thompson et al. (2018).

equation (2.3), the mass of companion in each system can be estimated by

$$a_{\max} \sim \frac{GM(a_{\max})}{s^2} \sim \frac{GM(a_{\max})}{(\Delta \mathrm{RV} \Delta t_{\mathrm{RV}})^2} \;\rightarrow\; M(a_{\max}) \sim \frac{(\Delta \mathrm{RV})^3 \Delta t_{\mathrm{RV}}}{G}, \tag{2.4}$$

where $M(a_{\max})$ is the estimated mass of companion and s is the separation between two bodies. Since they are interested in binary systems with massive compact objects, they select in total ~ 200 stars with largest estimated masses $M(a_{\max})$ as the candidates.

Determining the mass of unseen companions requires precise estimates of the orbital periods, inclinations, and eccentricities. Since the radial velocity data from APOGEE are not enough to determine the overall radial velocity curve as shown in Table 2.2, the authors need radial velocity follow-up observations. Before that, they search for periodic photometric variations in data from the All-Sky Automated Survey for Supernovae (ASAS-SN). Since periodic variations indicate transit signals, ellipsoidal variations, or starspots, they provide rough estimates of the orbital periods. Although many candidates show no variations, the authors find some systems showing periodic variations in data. Among all candidates, they pick up a red giant 2M05215658+4359220, which lies towards Auriga with Galactic co-ordinates $(l, b) = (164.774\,\mathrm{deg}, 4.184\,\mathrm{deg})$, as a feasible candidate since it shows the longest well-measured photometric variations. They find that the raw and phased V-band lightcurves for this system from the ASAS-SN over four observing seasons are consistent with the variations with the period of 83.2 days. Table 2.2 lists up the radial velocity for this system obtained from APOGEE, showing about 2.9 km/s/day apparent acceleration.

Then, they perform both multi-band photometry and radial velocity follow-up observations to constrain the orbit and photometric variations further. For photometry follow-up observation, they use the Post Observatory Mayhill (POM). For radial velocity follow-up observation, they use the spectroscopy with the Tillinghast Reflector Echelle Spectrograph (TRES) on the 1.5 m Tillinghast Reflector at the Fred Lawrence Whipple Observatory (FLWO). They find that multi-band photometry show periodic variations inconsistent with stellar pulsations or ellipsoidal variations but consistent with spots from the shape of lightcurves. Besides, they find that in total 11 radial velocity data from TRES are well-fit by a near-sinusoidal curve. Table 2.3 shows the list of all measured radial velocities from TRES and Figure 2.2 shows the plot for them. Table 2.4 lists the best-fit orbital parameters they find from TRES.

Table 2.4 shows that the system has a near-circular orbit with the eccentricity $e \approx 0.0048 \pm 0.0026$ and the orbital period $P_{\mathrm{orb}} \approx 83.2 \pm 0.06$ days. The mass function

BJD-2450000	Relative RV(km/s)	Uncertainty(km/s)
8006.9760	0.000	0.075
8023.9823	−43.313	0.075
8039.9004	−27.963	0.045
8051.9851	10.928	0.118
8070.9964	43.782	0.075
8099.8073	−30.033	0.054
8106.9178	−42.872	0.135
8112.8188	−44.863	0.088
8123.7971	−25.810	0.115
8136.6004	15.691	0.146
8143.7844	34.281	0.087

Table 2.3: Radial velocity measurements for 2M05215658+4359220 from data with TRES. In total, 11 spectra were obtained between 10 September 2017 and 25 January 2018. Adapted from Thompson et al. (2018).

parameter	value	unit	meaning
P	83.205 ± 0.064	days	orbital period
T	58115.93 ± 7.4	BJD − 2450000	pericentre passage
e	0.00476 ± 0.00255	$\cdots$	eccentricity
ω	197.13 ± 32.07	degrees	argument of pericentre
K	44.615 ± 0.123	km/s	RV semi-amplitude
γ	-0.389 ± 0.101	km/s	gamma velocity
$f(M)$	0.766 ± 0.00637	$M_\odot$	mass function

Table 2.4: Best-fit orbital parameters from radial velocity follow-up observation with TRES. Adapted from Thompson et al. (2018).

$f(M)$ in Table 2.4 is computed from the observed variables K, $P_{\rm orb}$ and e:

$$f(M) \equiv \frac{K^3 P_{\rm orb}}{2\pi G}(1-e^2)^{\frac{3}{2}}, \tag{2.5}$$

where K is the radial velocity semi-amplitude. Using equation (3.67), equation (2.5) reduces to

$$f(M) = \frac{M_{\rm CO}^3 \sin^3 i_{\rm orb}}{(M_{\rm giant} + M_{\rm CO})}, \tag{2.6}$$

where $M_{\rm CO}$ is the mass of unseen companion, $i_{\rm orb}$ is the orbital inclination, and $M_{\rm giant}$ is the mass of red giant 2M05215658+4359220. Therefore, the mass function is widely used to characterize the mass of unseen companion with the radial velocity observation. In order to analyze further, they assume that the system is tidally circularized and synchronized since $P_{\rm orb} \approx P_{\rm phot}$ and $e \approx 0$. Thus, for simplicity, they assume a fully

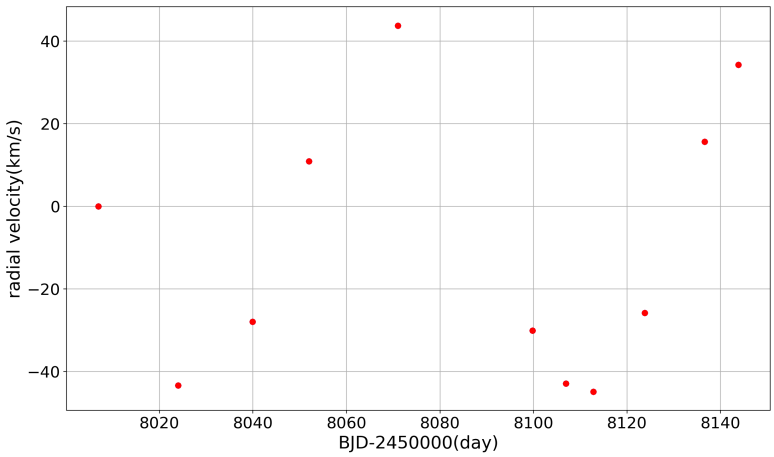

Figure 2.2: The radial velocity data for 2M05215658+4359220 from TRES follow-up observation. An error in each datum is within a filled circle.

parameter	value	meaning
$M_{\rm CO}$	$3.2^{+1.1}_{-0.4}$ $M_\odot$	mass of companion
$M_{\rm giant}$	$3.0^{+0.6}_{-0.5}$ $M_\odot$	mass of red giant
$\sin i$	$0.97^{+0.02}_{-0.14}$	orbital inclination
R	$23.8^{+3.9}_{-0.6}$ $R_\odot$	radius of red giant

Table 2.5: Best-fit parameters from TRES, *Gaia*, and the SED. Adapted from Thompson et al. (2018).

synchronized and aligned orbit:

$$P_{\rm rot} = P_{\rm orb} = P, \quad i_{\rm rot} = i_{\rm orb} = i. \tag{2.7}$$

Then, they search for the best-fit model in stellar evolution track with the surface gravity constraint $\log g = 2.35 \pm 0.14$ from TRES spectroscopy, the giant radius R, the bolometric luminosity L and the effective temperature $T_{\rm eff}$ from *Gaia* and the spectral energy distribution (SED). This procedure reveals that best-fit value of companion mass lies on the range between the maximum neutron star and the minimum black hole masses from theoretical models. Table 2.5 summarizes the best-fit parameters.

Since $\log g$ for this sytem is known to include large systematic uncertainties ($2.2 \leq \log g \leq 2.6$ depending on observation), they also try fitting procedure without the constraint on $\log g$. Table 2.6 shows the result. However, they conclude that the best-fit values in Table 2.5 are better since the best-fit $\log g$ is found to be too small ($\log g \approx 1.7^{+0.2}_{-0.3}$) without constraint.

As a result, they reach a conclusion that 2M05215658+4359220 is a binary system consisting of a red giant and a possible black hole. However, there is the possibility

parameter	value	meaning
$M_{\rm CO}$	$5.5^{+3.2}_{-2.2}$ $\mathrm{M}_\odot$	mass of companion
$M_{\rm giant}$	$2.2^{+1.2}_{-0.9}$ $\mathrm{M}_\odot$	mass of red giant
$\sin i$	$0.65^{+0.17}_{-0.12}$	orbital inclination
R	$35.8^{+8.3}_{-7.6}$ $\mathrm{R}_\odot$	radius of red giant

Table 2.6: Same as Table 2.5 but derived without constraint on $\log g$. Adapted from Thompson et al. (2018).

that the black hole is actually an unseen binary since it is not yet confirmed as a single object. Later, supposing that it is a binary rather than a single, we put a constraint on the binary as a practical application of our methodology.

2.1.3 A triple system PSR J0337+1715

As the final part of this section, we have a look at the discovery of a near-circular coplanar triple consisting of a white dwarf - millisecond pulsar binary and another outer white dwarf. If the motion of the outer white dwarf is precisely determined, this system would provide an ideal situation for our methodology. Thus, it is important since it implies the existence of the system for which the formulae derived in this thesis are directly applicable.

In 2014, Ransom et al. (2014) announced the discovery of a hierarchical triple consisting of a millisecond pulsar PSR J0337+1715, an inner white dwarf, and another outer white dwarf. As a part of large-scale pulsar survey, they discover a millisecond pulsar PSR J0337+1715 having a spin period of 2.73 ms with the Robert C. Byrd Green Bank Telescope (GBT). Since a millisecond pulsar emits the beams hundreds of times per second due to its rotation, the spin rate can be measured with high precision using pulse arriving time. In addition, analysing its delay in detail, it is possible to obtain the orbital information. At first, this system is considered to be a binary consisting of a millisecond pulsar and an inner white dwarf, however, the large timing systematics later reveal that the time delay is composed of two periodic variations with different periods. This fact shows that this system should be classified into triple rather than binary. Although two other millisecond pulsars B1257+12 and B1620-26 have already known to have multiple companions, they contain planet-mass companions. On the other hand, large timing perturbations in PSR J0337+1715 implies more massive tertiary than a planet-mass companion.

In order to constrain the system's position and orbital parameters, and the tertiary, they perform intensive multi-frequency radio timing campaign using the GBT, the Arecibo telescope, and the Westerbork Synthesis Radio Telescope (WSRT). The Arecibo has median arrival time uncertainties of 0.8 μs in 10 s. Thus, half-hour integrations achieve a precision of about 100 ns, which makes it possible to achieve one of the highest known precisions to PSR J0337+1715. They first approximate the motion as two Keplerian orbits, with the centre of inner binary moving around in the outer

parameter	value	meaning
P	2.73258863244(9) ms	Pulsar period
$\dot{P}$	$1.7666(9)(12) \times 10^{-20}$	Pulsar period derivative
τ	2.5×10^9 yrs	Characteristic age
$a_{\rm I}$	1.9242(4) ls	Pulsar semi-major axis(inner)
$e_{\rm I}$	$6.9178(2) \times 10^{-4}$	Eccentricity(inner)
$\omega_{\rm I}$	97.6182(19) deg	Longitude of pericentre(inner)
$a_{\rm O}$	118.04(3) ls	Pulsar semi-major axis(outer)
$e_{\rm O}$	$3.53561955(17) \times 10^{-2}$	Eccentricity(outer)
$\omega_{\rm O}$	95.619493(19) deg	Longitude of pericentre(outer)
i	39.243(11) deg	Inclination of invariant plane
$i_{\rm I}$	39.254(10) deg	Inclination of inner orbit
δ_i	$1.20(17) \times 10^{-2}$ deg	Angle between orbital planes
δ_ω	$-1.9987(19)$ deg	Angle between eccentricity vectors
$m_{\rm p}$	1.4378(13) $M_\odot$	Pulsar mass
$m_{\rm cI}$	0.19751(15) $M_\odot$	Inner companion mass
$m_{\rm cO}$	0.4101(3) $M_\odot$	Outer companion mass

Table 2.7: Best-fit system parameters for PSR J0337+1715. Note that values in parentheses are 1σ errors in the final decimal places. Adapted from Ransom et al. (2014).

orbit. Then, they determine pulse times of arrival (TOAs) using standard techniques and correct them to the Solar System barycentre at infinite frequency using a precise radio position obtained with the Very Long Baseline Array (VLBA). The variations of TOAs are known to have two physical origins. One is the "Rømer delay", which is a geometric effect due to the finite speed of light. The other is the "Einstein delay", which is a cumlative effect of time dilation due to the special relativistic transverse Doppler effect and the general relativistic gravitational redshift. The Rømer delay reflects the infomation on both inner and outer orbits.

Then, they plot the arrival timing data from the GBT, the WSRT, and the Arecibo telescope, and compare them with the Rømer delays model. They first calculate the residuals between data and two-Keplerian-orbit approximation. It shows the large systematic descrepancies up to several microseconds over multiple timescales, showing the presence of three-body interactions. Actually, these discrepancies contain much information about masses and geonetry of system. Thus, it is necessary to find parameter sets minimizing the difference between measured TOAs and those by three-body integration. For this purpose, they use the Monte Carlo techniques to obtain the best-fit parameters. Table 2.7 summarizes the best-fit and derived parameters they find.

Besides, they suceed in identifying an object with blue colors in the Sloan Digital Sky Survey (SDSS). The optical spectroscopy reveals that it is consistent with a inner

white dwarf in the system confirmed by pulsar timing. It also shows that the outer companion cannot be a low-mass main-sequence star for lack of near- and mid- infrared excess, implying it should be a white dwarf with an effective temperature less than 20000 K. Therefore, they finally conclude that the system is a triple consisting of a millisecond pulsar - white dwarf inner binary and another outer white dwarf.

This system is extremely surprising since its orbits are extraordinarily coplanar and near-circular. The authors propose a possible scenario to form such a system as follows. In a multiple star system, the most massive star experiences a supernove turning into a neutron star. Two companions survive the explosion, probably in eccentric orbits. After $\sim 10^9$ yrs, the outermost star evolves and transfers mass onto inner binary. The angular momentum vectors of inner and outer orbits nearly align due to the torque during this process. After the outer star evolves into a white dwarf and another $\sim 10^9$ yrs passes, the remaining main sequence star finally becomes a white dwarf. During this phase, the inner orbit becomes highly circularized and transfers small amount of mass to a neutron star, speeding up its rotation rate to form a millisecond pulsar. Then, three-body secular effects have aligned the apsides of two orbits. Although this scenario is not yet fully confirmed whether or not to work well, it could produce near-circular and coplanar hierarchical triples if it can really take place.

2.2 Formation scenarios and observing proposals

Although the formation mechanism of compact binaries is not yet clearly understood, some scenarios have been proposed. These scenarios are roughly classified into three categories, isolated binary evolution, dynamical formation in star dense rigions, and primordial origin. Among these scenarios, the isolated binary evolution and dynamical formation scenarios are considered to be most promising ones. Since each scenario has characteristics for produced binaries, it is important to understand them. In this section, we briefly summarize two major scenarios (i.e. isolated binary evolution and dynamical formation) and their uniqueness especially on the preferred orbital parameters.

Besides, recently there are many observing proposals to search for star - black hole binaries with *Gaia* and *TESS*. Since *Gaia* and *TESS* have their own preferences for the property of detectable binaries, the knowledge on them is very useful to presume the binaries providing the targets to which we will apply our methodology. Thus, we also briefly summarize Yamaguchi et al. (2018) and Masuda & Hotokezaka (2018), which are proposals with *Gaia* and *TESS*, respectivaly.

2.2.1 Compact binary formation through isolated binary evolution

The isolated binary evolution scenario (e.g. Belczyński & Bulik 1999; Belczynski et al. 2012, 2016, 2002, 2007; Dominik et al. 2012, 2013; Kinugawa et al. 2014, 2016) is

proposed as a most promising formation mechanism of close binary black holes. Apart from differences in detail concerns, overall picture of this scenario is summarized as follows.

This scenaio supposes presence of pre-existing binaries consisting of massive low-metal stars in the early universe. Since the typical lifetime of massive star is no more than ∼Myrs, the stars in a binary system quickly evolve off main sequence phases. First, one star in a binary evolves into a super redgiant and increase its radius drastically. Once the star fills in its Roche robe, significant mass flows into a companion, increasing the orbital separation and mass of companion. After the star finishes its super red giant phase, it evolves into a black hole via either direct collapse or non-violate supernova. During this phase, a star - black hole binary is formed. After a while, the companion also evolves into a giant phase. If the mass transfer is too strong to be stable, the unstable mass flow leads to the common-envelope phase, where the preformed black hole is absorbed by the envelope of the companion giant. During the common-envelope phase, since the orbital energy is consumed to eject the envelope, the orbital separation significantly decreases. Eventually, the giant also evolves into a black hole without a violate supernova. These successive processes preferentially form a close binary black hole. Since binary interactions such as the mass transfer and common-envelope phase well circularize an orbit, a typical produced binary tends to have vary small eccentricity $e \sim 0$.

Although it is confirmed that this scenario works well to produce close black hole binaries (e.g. Belczynski et al. 2016; Dominik et al. 2013; Kinugawa et al. 2014, 2016), there are many uncertainties in physical processes during this scenario. For example, it is known that violate common-envelope phase often leads to coalescense before compact binaries are formed although this process is important to form close binaries that merge within the age of universe. Since the efficiency of common-envelope phase is not yet clearly understood, this phase would change the surviving rate of close compact binaries. Even more serious problem raises up from uncertain supernova physics. Several previous researches (e.g. Belczyński & Bulik 1999; Belczynski et al. 2002; Kinugawa et al. 2014, 2016) found that significant mass loss and large natal kick due to supernova could produce wide and highly eccentric orbits although it simultaneously disrupts many binaries. If the direct collapse is really preferable for massive stars as proposed in Fryer et al. (2012), the natal kick and mass loss may be almost negligible. Thus, this scenario would produce massive compact binaries with circular close orbits.

No matter whether or not black hole binaries have initially eccentric orbits, the gravitational wave emission well circularizes the orbits after a long time evolution. Thus, the orbits are usually expected to have almost zero eccentricities before coalescence. On the other hand, our methodology can detect wide and eccentric binaries if they exist since the methodology is irrelevant to coalescense. Our methodology could provide even new hints to understand currently uncertain supernova processes although careful checks are required to distinguish eccentric binaries formed via the dynamical formation scenario.

2.2.2 Compact binary formation through dynamical interactions in star dense region

The dynamical formation scenario (e.g. O'Leary et al. 2009, 2006; Portegies Zwart & McMillan 2000; Rodriguez et al. 2016; Tagawa et al. 2016) is proposed as a counterpart of the isolated binary evolution scenario. While the isolated binary scenario requires pre-existing massive binary systems, the dynamical formation scenario enables single black holes to form binary black holes via strong gravitational interaction in star dense region. In this subsection, we have a look at the rough sketch of the dynamical formation scenario and the characteristics of the produced binaries.

Portegies Zwart & McMillan (2000) explored the possibility that black holes become close binaries via numerous gravitational scatterings with other members in star dense region, and estimate merger rate of the products. They found that this scenario could produce many black hole binaries even if their component black holes do not originally belong to binary systems. The overall picture of this scenario is summarized as follows. After all massive stars evolve off into black holes in star dense region such as globular cluster, black holes become most massive objects there. Since massive objects feel the dynamical friction strongly and lose kinetic energy, black holes tend to sink into the inner part of star dense region (e.g. Morris 1993). As a result of the condensation of black holes around core, many gravitational scattering and capture processes take place among black holes and other stars, resulting in the formation of binary black holes via three-body encounters. It is known that black holes preferencially form binary black holes with other black holes (e.g. Kulkarni et al. 1993). Therefore, the typical products may be binary black holes. While the close binary black holes become more tightly bound by superelastic encounter with other objects (e.g. Heggie 1975; Kulkarni et al. 1993), they are eventually ejected after getting the velocities large enough to escape from star dense region. Majority of these escaping binary black holes may have short enough orbital periods and high enough eccentricities that gravitational wave emissions lead them to coalescence within a few Gyrs.

In order to confirm this scenario, Portegies Zwart & McMillan (2000) performed N-body simulation with GRAPE-4, which is a special purpose computer for the multi-body problem. They used 2048 equal mass stars, with 1% of them 10 times more massive than the average (i.e. black holes). As a result, they found that $\sim 30\%$ of in total 204 black holes were ejected from a cluster in the form of binary black holes, $\sim 61\%$ were ejected in the form of single black holes, and $\sim 8\%$ were retained by the cluster. The binding energy of binary black holes E_b had a roughly log-flat distribution within the range of $1000kT - 10000kT$, where $(3/2)kT$ is mean stellar kiniteic energy in the cluster. The eccentricities of binaries roughly followed a thermal distirbution ($p(e) \sim 2e$) with high eccentricities slightly overrepresented. They also found that $\gtrsim 90\%$ of black holes were ejected before the cluster had lost 30% of its initial mass (roughly within a few Gyrs).

After that, they estimated merger rate within 12 Gyr for typical star dense regions. The result is listed in Table 2.8. Table 2.8 shows that a variety of binary black holes may be formed depending on the properties of clusters although massive cluster tend

cluster type	$\log M$ ($M_\odot$)	$\log r_{\rm vir}$ (pc)	$1000kT$ ($R_\odot$)	$N_{\rm bh}$	$f_{\rm merge}$ (%)	MR ($\rm Myr^{-1}$)
populus	4.5	-0.4	420	7.9	7.7	0.0061
globular	5.5 ± 0.5	0.5 ± 0.3	315	150	51	0.0064
nucleus	~ 7	$\lesssim 0$	$\lesssim 3.3$	2500	100	0.21
zero-age globular	6.0 ± 0.5	0 ± 0.3	33	500	92	0.038

Table 2.8: Typical parameters for each star dense region and expected merger rate. The M is the total mass and $r_{\rm vir}$ is the virial radius. The fourth column denotes the separation of binary consisting of two $10M_\odot$ black holes to obtain $1000kT$ orbital energy. The $N_{\rm bh}$ is the expected number of binary black holes. The $f_{\rm merge}$ is the fraction of these binaries which merge within 12Gyr. The final column denotes the contribution to the total black hole merger rate per cluster. Adapted from Portegies Zwart & McMillan (2000).

to produce tight binaries which merge soon after ejection.

O'Leary et al. (2006) systematically survey the distribution of eccentricities, orbital energies, and chirp masses for ejected binary black hole mergers. Instead of using expensive N-body numerical simulation, they consider this scenario using a Monte Carlo technique to sample interaction rates, and few-body numerical simulation to treat each interaction. Thus, they succeeded to contain $\sim 10^6$ bodies including ~ 500 black holes depending on models in their calculations. Since the ejected binary black holes are circularized via gravitational wave emissions, their orbits are normally circular just before merger even though they tend to have high eccentricities when ejected. O'Leary et al. (2006) found that the eccentricities of almost all orbits would be less than 0.001 when their gravitational wave frequencies enter LIGO's detectable range (~ 10 Hz). They, however, found that LISA preferencially could detect the binary black holes with their eccentricities between 0.01 and 1 since LISA would have sensitivity around $\sim 10^{-3}$ Hz. More recent analysis including binary - binary interaction in general relativistic scheme (Zevin et al. 2018) also predicted that LISA would detect gravitational waves from binary black holes with eccentricities between ~ 0.00001 and ~ 0.1 with the peak at ~ 0.001 around 10^{-2} Hz.

Therefore, apart from merger, the binary black holes formed dynamically will have high eccentricities. They found the chirp masses of merging binary black holes range from ~ 10 to ~ 100 although the distribution highly depend on models. They also computed the energy distribution of binary black holes ejected before equipartition using a model. They found that the energy distribution is nearly lognormal with a peak of $\sim 10^4 kT$ between $\sim 100kT$ and $\sim 10^5 kT$, almost independent of models. The authors implied the discrepancy from Portegies Zwart & McMillan (2000) might be due to small number particles in the simulation in Portegies Zwart & McMillan (2000). Regardless, the results by Portegies Zwart & McMillan (2000) and O'Leary et al. (2006) may imply the presence of wider separation for ejected binary black holes.

Rodriguez et al. (2016) investigated the possibility that the progenitor binary black hole of GW150914 is formed by dynamical scenario. Although they did not calculate the distribution of orbital parameters since their concern was possible GW150914 progenitors, they found that the possible progenitors tend to have large eccentricities $\gtrsim 0.5$ and relatively wide separation $\gtrsim 0.3$ au at ejection. It probably imply the preference of eccentric and wider orbits indirectly. Interestingly, Rodriguez et al. (2016) found a temporary hierarchical triple consisting of blackholes among possible GW150914 progenitors during many scattering events although it was replaced by binary black holes before ejection. It may imply that this scenario could produce a hierarchical triple consisting of a star and inner binary black holes even though this class of objects are not much.

In summary, the dynamical scenario would provide relatively wider and highly eccentric binary black holes although it is not yet fully confirmed. Although gravitational wave emission almost completely circularize the orbits before merger, our methodology can detect eccentric binaries from this scenario long before coalescence.

2.2.3 Observing proposals for binary systems including black holes with *Gaia*

There are many proposals to search for star - black hole binaries using precise astrometry observation with *Gaia*(e.g. Breivik et al. 2017; Kawanaka et al. 2017; Mashian & Loeb 2017; Yamaguchi et al. 2018). Yamaguchi et al. (2018) suggest that *Gaia* can detect $200 - 1000$ binaries dependiong on the parameters in the isolated binary evolution model within 5 year operation. Since the binaries detected with *Gaia* will provide the targets to which we can apply our methodology, it is beneficial to know which kind of binaries *Gaia* will detect. In this subsection, we briefly summarize the proposal Yamaguchi et al. (2018) for this purpose.

First, Yamaguchi et al. (2018) estimate the number of star - black hole binaries in the Galaxy using the standard isolated binary formation scenario. They use the initial mass function of stars and binary distribution in terms of mass ratio of component stars, and estimate the number of binary systems. They assume that the initial separation distribution of binaries is logarithmically flat, and binary orbits are circular initially. If the primary collapses into a black hole and the secondary still exists as a star, they count it as a star - black hole binary. In order to consider spatial distribution of such systems in the Galaxy, they use the exponentially decreasing number density in the Galactic plane. Since the systems in the Galactic bulge should not be detected due to strong interstellar absorption, they do not consider the systems located in the bulge. For simplicity, they assume that 50% of stellar systems are binaries. Taking into account the mass transfer and common-envelope phase during evolution, they can estimate the masses and separations of binary systems after evolution. They consider several different values of paramaters describing the initial mass function, the binary distribution for a given mass ratio, the relation between zero-age mass and final black hole mass, and the common-envelope phase efficiency. They also take into account the

interstellar extinction to obtain detectable companions with *Gaia*.

Next, the authors consider the required condition to identify star - black hole binary systems with the standard errors in *Gaia* observation. For astrometry observation, we obtain

$$\frac{(M_{\rm BH}+M_2)^2}{M_{\rm BH}^3}=\frac{G}{4\pi^2}\frac{P_{\rm orb}^2}{(a_* D)^3}, \tag{2.8}$$

where $M_{\rm BH}$ and M_2 are the masses of black hole and companion, respectively, $P_{\rm orb}$ is the orbital period, a_* is the angular semi-major axis, D is the distance. Thus, it is necessary to obtain $P_{\rm orb}$, a_*, D precisely to determine $M_{\rm BH}$. Through the discussion on the standard errors of the observed quantities, the authors found the required condition for the semi-major axis of binary A:

$$A > 10\frac{M_{\rm BH}+M_2}{M_{\rm BH}}\sigma_\pi(m_V)D \equiv A_{\rm ast}, \tag{2.9}$$

where $\sigma_\pi(m_V)$ is the *Gaia* standard error of parallax at a given apparent V-band magnitude m_V (Gaia Collaboration et al. 2016):

$$\sigma_\pi(m_V) \approx \sqrt{-1.631+680.8z(m_V)+32.73z^2(m_V)}, \tag{2.10}$$

where

$$z(m_V)=10^{0.4(\max[12.09,m_V]-15)}. \tag{2.11}$$

Besides, they consider the required condition for semi-major axis from the viewpoint of orbital period. Considering the result from astrometry observation with *Hipparcos*, it is estimated that the standard errors in observed orbital periods are $\lesssim 10\%$ if the periods are shorter than 2/3 of the total observation time. Since they consider 5 year oparation with *Gaia* in total, the upper limit of orbital period is ~ 3 years. In addition, since the observation cadence of *Gaia* is 50 days, the lower limit is 50 days. Therefore, the required condition for semi-major axis is

$$\max[A_{\rm ast}, A(P_{\rm orb}=50\ {\rm days})] < A < A(P_{\rm orb}=3\ {\rm years}). \tag{2.12}$$

As a result, the authors found that in total $200-1000$ binaries would be detected with *Gaia* depending on the values of parameters. They also found that the detectable binaries would locate within $1-10$ kpc and the peak would be at 7 kpc. While the estimated number of binaries increases monotonically within ~ 5 kpc due to larger volume, it drastically decreases after the peak ~ 7 kpc. The distribution of black hole mass is sensitive to the parameters, especially the mass ratio of zero-age star and black hole. The distribution is the decreaing powerlaw within $4-30\ M_\odot$ in the fiducial case. However, the maximum mass can reach $\sim 100\ M_\odot$ if they assume high efficiency from zero-age star mass to black hole mass. They also found that the contribution of companion less massive that $20\ M_\odot$ is much smaller than those with larger masses. Since the mass ratio smaller than 0.3 undergo a strong common-envelope phase, the orbits might be too small to detect with *Gaia*.

In summary, considering the required condition (2.12), *Gaia* will provide the systems which have relatively larger orbits with au-scale separations. It will be main difference between the systems *TESS* can detect. Although they do not consider the mass loss due to the stellar wind, natal kick, and initial eccentricity, they conclude that the countable black hole masses may not change drastically even including these effects from the result in Breivik et al. (2017).

2.2.4 Observing proposals for binary systems including black holes with *TESS*

Masuda & Hotokezaka (2018) recently point out that *TESS* will also detect star - black hole binaries via the photometric variations in light curves. While the typical targets of *Gaia* will be ~ 10 $M_\odot$ black holes in binary systems with their separations au-scale, Masuda & Hotokezaka (2018) find that the targets of *TESS* will be relatively tighter detached binaries with separations $\lesssim 0.3$au. Thus, *TESS* will provide complementary samples of binary systems. In this subsection, we have a look at the observing proposal Masuda & Hotokezaka (2018).

First, they consider three kinds of effects in lightcurves that unseen massive companions induce. One is the "self-lensing", which causes pulse-like periodic brightening due to microlensing during eclipse. Another is the "ellipsoidal variations", which cause the phase-curve modulations induced by the change of geometrical shapse of stars due to tidal forces by massive companions. The other is the "Doppler beaming", which is the special relativistic effect and causes the change of shape of light curves. Since they need consider the required conditions separately from self-lensing effect, they classify the latter two effects into the phase-curve variation. Although they concentrate on circular orbits throughaout their paper, this method will also be promising to detect the eccentric binaries.

Next, they computed the magnitude of each signal for given parameters to estimate the number of stars bright enough to detect the effects above with *TESS*. They separately count the number of detectable stars for the self-lensing and phase-curve variation effects. They define that the self-lensing is detectable if at least two pulses are observed. They define that the phase-curve variation is detectable if the binary period is less than half the observing duration. Since they are interested in detached stable binaries, they exclude the cases that the separation is within the Roche robe or strong gravitational wave emissions cause rapid orbital decays during observing duration. *TESS* performs photometric survey for transiting exoplanets around near-by stars. *TESS* will observe each sector for 27.4 days with 30 minute cadence usually. They use these values to estimate the number of targets.

They assume that the self-lensing signals are detectable if the following relation is satisfied:

$$\sqrt{n}\left(\frac{s_{\rm sl}}{\sigma_\tau}\right) > 8.3, \quad \sigma_\tau \equiv \sigma_{30\ \rm min}\left(\frac{\tau}{30\ \rm min}\right)^{-0.5}, \tag{2.13}$$

where $s_{\rm sl}$ is the pulse hight, n is the number of pulses, τ is the expected duration of a

single pulse, and $\sigma_{30\ \mathrm{min}}$ is the noise level over 30 minute timescale corresponding to one cadence. They used $\sigma_{30\ \mathrm{min}}$ by modifying $\sigma_{1\ \mathrm{hour}}$ available in Stassun et al. (2018). Equation (2.13) corresponds to the false-positive rate of $\sim 10^{-9}$ (Sullivan et al. 2015). For the phase-curve variation, they use the following required condition:

$$\sqrt{\frac{T}{30\ \mathrm{min}}}\left(\frac{s}{\sigma_{30\ \mathrm{min}}}\right) > 10.4, \tag{2.14}$$

where T is the observing duration, s is the amplitude of sine waves corresponding to phase-curve variation effects. Equation (2.14) also corresponds to the false-positive rate of $\sim 10^{-9}$. Assuming that the inclination is random and using the *TESS* input catalog, which is a list of stars among which the target of *TESS* will be chosen, they found that $\sim \mathcal{O}(10^7)$ and $\sim \mathcal{O}(10^5)$ stars with periods up to ~ 10 days would be bright enough to detect phase-curve variation and self-lensing, respectively. Since the self-lensing effect is detectable only when the orbit is quite nearly edge-on, the number of targets is significantly smaller that that of phase-curve variation.

Next, they consider the occurrencre rate of star - black hole binaries based on two models. One is the "Field Binary model", which is a simple estimation constructed by the combinatation of powerlaw occurence rate of black holes and that of massive binaries. The other is the "Common-envelope Evolution model", which consider the common-envelope phase during evolution. Since they concentrate on large mass ratio, they need not consider the mass transfer as Yamaguchi et al. (2018). Combining the occurence rate and the result of searchable stars, they can construct the estimated number of detectable star - black hole binaries with *TESS* in terms of the mass of black hole and the orbital period.

As a result, regardless of the binary occurrence models, they found that *TESS* would detect $\sim \mathcal{O}(10)$ and $\sim \mathcal{O}(10^3)$ binaries by self-lensing and phase-curve variation, respectively. Unlike the binaries which will be detected by *Gaia*, the tight binaries with $0.3 - 30.0$ day orbital periods will be detected by *TESS*. They found that the peak of orbital period was ~ 5 days and the peak of mass was $\sim 20\ M_\odot$. Assuming 0.8 day orbital period and 7 $M_\odot$ black hole, which is the representative value of X-ray black hole binaries, they estimated 0.25 kpc and 1.3 kpc as the maximum searchable distances for sun-like companions by self-lensing and phase-curve variation, respectively.

In summary, while *Gaia* is expected to detect wide-separation and massive binary systems beyond 1 kpc, *TESS* will detect the tight star - black hole binaries in near-by space. Since the performance of radial velocity method is the best for bright near-by stars, the binaries that *TESS* will find may provide good samples for our methodology.

Chapter 3

Perturbation theory to the three-body problem

3.1 Two body problem

Before moving to the detailed formulation of three-body perturbation theory in celestial mechanics, we start from the simplest case for the motion under the gravitational interaction, *i.e.* the two-body problem. Many references are available for the two-body problem (Brouwer & Clemence 1961; Moulton 1914; Murray & Dermott 2000; Roy 2005, e.g.). This section specifically follows Murray & Dermott (2000). Consider two point particles with mass m_1 and m_2. They interact each other only by the Newtonian gravitational force.

Figure 3.1 shows the configuration of the system that we consider here. In terms of an arbitrary Cartesian co-ordinate system (X, Y, Z), the equations of motion for the two particles are written as follows:

$$\ddot{\boldsymbol{r}}_1 = -Gm_2 \frac{(\boldsymbol{r}_1 - \boldsymbol{r}_2)}{|\boldsymbol{r}_1 - \boldsymbol{r}_2|^3} \tag{3.1}$$

and

$$\ddot{\boldsymbol{r}}_2 = Gm_1 \frac{(\boldsymbol{r}_1 - \boldsymbol{r}_2)}{|\boldsymbol{r}_1 - \boldsymbol{r}_2|^3}, \tag{3.2}$$

where G is the universal gravitational constant, $\boldsymbol{r}_1$ and $\boldsymbol{r}_2$ are the position vectors of m_1 and m_2, respectively. We introduce the position vector of the centre of mass $\boldsymbol{R}$, and the relative position vector $\boldsymbol{r}$:

$$\boldsymbol{R} \equiv \frac{m_1\boldsymbol{r}_1 + m_2\boldsymbol{r}_2}{m_1 + m_2} \tag{3.3}$$

and

$$\boldsymbol{r} \equiv \boldsymbol{r}_2 - \boldsymbol{r}_1. \tag{3.4}$$

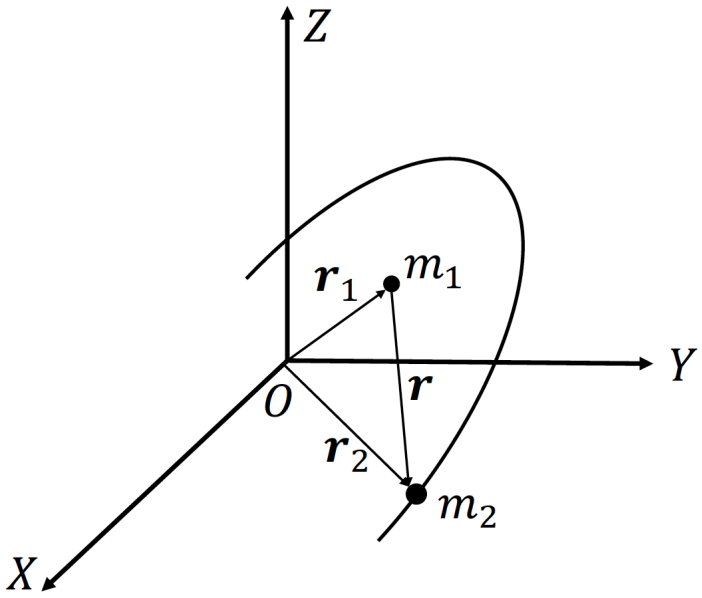

Figure 3.1: Two-body system in an arbitrary Cartesian co-ordinates

Using equations (3.3) and (3.4), we rewrite equations (3.1) and (3.2) to separate the motion of the centre of mass and the relative motion:

$$\ddot{\boldsymbol{R}} = \boldsymbol{0} \tag{3.5}$$

and

$$\ddot{\boldsymbol{r}} = -\frac{Gm_{\text{tot}}\boldsymbol{r}}{r^3}, \tag{3.6}$$

where m_{tot} is the total mass of the system. Equation (3.5) shows the centre of mass moves with constant velocity.

Taking the vector product of $\boldsymbol{r}$ with equation (3.6), we obtain

$$\boldsymbol{r} \times \ddot{\boldsymbol{r}} = \boldsymbol{0}, \tag{3.7}$$

thus,

$$\boldsymbol{r} \times \dot{\boldsymbol{r}} = \boldsymbol{h}, \tag{3.8}$$

where $\boldsymbol{h}$ is a constant vector and called the "specific relative angular momentum". Equation (3.8) shows that $\boldsymbol{r}$ and $\dot{\boldsymbol{r}}$ always lie on the invariant plane perpendicular to $\boldsymbol{h}$. This plane is called the "orbital plane". Since we are interested in the relative motion between two bodies, we concentrate on the motion fixed on the orbital plane using the result from equation (3.8).

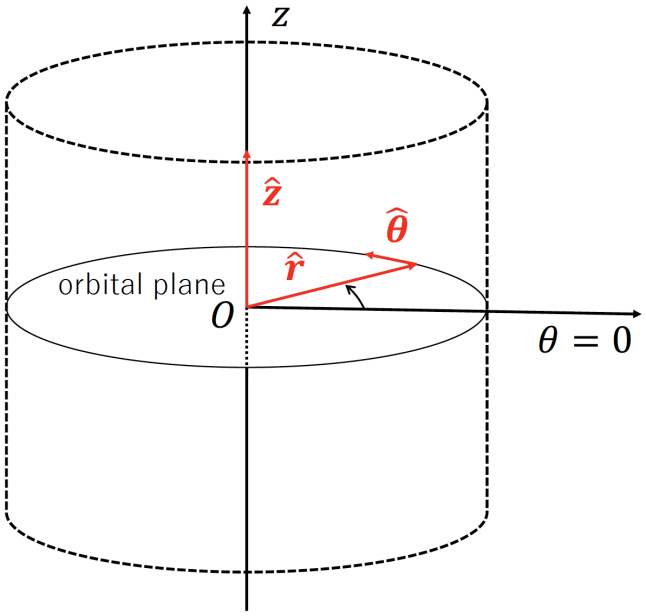

Figure 3.2: Cylindrical co-ordinate system.

Consider a cylindrical co-ordinate system (r, θ, z) with the origin at m_1 as shown in Figure 3.2. In the cylindrical co-ordinates, we can define basis vectors $\{\hat{\boldsymbol{r}}, \hat{\boldsymbol{\theta}}, \hat{\boldsymbol{z}}\}$ as

$$\hat{\boldsymbol{r}} \equiv \begin{pmatrix} \cos\theta \\ \sin\theta \\ 0 \end{pmatrix}, \quad \hat{\boldsymbol{\theta}} \equiv \begin{pmatrix} -\sin\theta \\ \cos\theta \\ 0 \end{pmatrix}, \quad \hat{\boldsymbol{z}} \equiv \begin{pmatrix} 0 \\ 0 \\ 1 \end{pmatrix}. \tag{3.9}$$

Using these basis vectors, the position vector $\boldsymbol{r}$, the velocity vector $\dot{\boldsymbol{r}}$, and the acceleration vector $\ddot{\boldsymbol{r}}$ are written as follows:

$$\boldsymbol{r} = r\hat{\boldsymbol{r}}, \tag{3.10}$$

$$\dot{\boldsymbol{r}} = \frac{d}{dt}(r\hat{\boldsymbol{r}}) = \dot{r}\hat{\boldsymbol{r}} + r\dot{\hat{\boldsymbol{r}}} = \dot{r}\hat{\boldsymbol{r}} + r\dot{\theta}\hat{\boldsymbol{\theta}}, \tag{3.11}$$

and

$$\begin{aligned} \ddot{\boldsymbol{r}} &= \frac{d}{dt}(\dot{\boldsymbol{r}}) = \ddot{r}\hat{\boldsymbol{r}} + \dot{r}\dot{\hat{\boldsymbol{r}}} + \dot{r}\dot{\theta}\hat{\boldsymbol{\theta}} + r\ddot{\theta}\hat{\boldsymbol{\theta}} + r\dot{\theta}\dot{\hat{\boldsymbol{\theta}}} \\ &= (\ddot{r} - r\dot{\theta})\hat{\boldsymbol{r}} + \left[\frac{1}{r}\frac{d}{dt}(r^2\dot{\theta})\right]\hat{\boldsymbol{\theta}}. \end{aligned} \tag{3.12}$$

Using equations (3.10) - (3.12), equations (3.6) and (3.8) become

$$(\ddot{r} - r\dot{\theta}^2)\hat{\boldsymbol{r}} = -\frac{Gm_{\text{tot}}}{r^2}\hat{\boldsymbol{r}} \tag{3.13}$$

and

$$h\hat{\boldsymbol{z}} \equiv r^2\dot{\theta}\hat{\boldsymbol{z}} = \boldsymbol{h}. \tag{3.14}$$

The areal element dA is

$$dA = \frac{1}{2}|r\hat{\boldsymbol{r}} \times rd\theta\hat{\boldsymbol{\theta}}| = \frac{1}{2}r^2 d\theta. \tag{3.15}$$

Thus, using equation (3.14), the areal velocity dA/dt is written as

$$\frac{dA}{dt} = \frac{1}{2}r^2\dot{\theta} = \frac{1}{2}h. \tag{3.16}$$

Since h is constant, this equation shows that the areal velocity is also constant. This corresponds to Kepler's second law.

In order to determine the orbit, we solve equation (3.13). Using $u \equiv 1/r$ and equation (3.14), $\dot{r}$ and $\ddot{r}$ are given by

$$\dot{r} = -r^2\dot{\theta}\frac{du}{d\theta} = -h\frac{du}{d\theta} \tag{3.17}$$

and

$$\ddot{r} = -hu^2r^2\dot{\theta}\frac{d^2u}{d\theta^2} = -h^2u^2\frac{d^2u}{d\theta^2}. \tag{3.18}$$

Therefore, when we use u instead of r, equation (3.13) reduces to

$$\frac{d^2u}{d\theta^2} + u = \frac{Gm_{\rm tot}}{h^2}. \tag{3.19}$$

Thie equations is solved as:

$$r = \frac{1}{u} = \frac{h^2/Gm_{\rm tot}}{1 + e\cos(\theta - \varpi)}, \tag{3.20}$$

where e and ϖ are constants of integration and called the "eccentricity" and the "longitude of pericentre", respectively. Equation (3.20) shows that when $h \neq 0$, the orbit is ellipse ($0 \leq e < 1$), parabola ($e = 1$) and hyperbola ($e > 1$) with m_1 at the focus (see Figure 3.3). Elliptical orbits correspond to Kepler's first law.

For an elliptical orbit, we can define semi-major axis a so that $a(1-e)$ and $a(1+e)$ become the minimum and maximum values of r, respectively. The point at which r takes the minimum value is called the "pericentre" and the point at which r takes the maximum is called the "apocentre". If we introduce the "true anomaly" f as $\theta - \varpi$, the pericentre and apocentre correspond to $f = 0$ and $f = \pi$, respectively (see Figure 3.4). The length b in Figure 3.4 is called the "semi-minor axis". Using the fact that the summation of distances from two foci is equal for every point on an ellipse, we can express b in terms of a and e:

$$a(1+e) + a(1-e) = 2\sqrt{b^2 + (ae)^2} \;\rightarrow\; b = a\sqrt{1-e^2}. \tag{3.21}$$

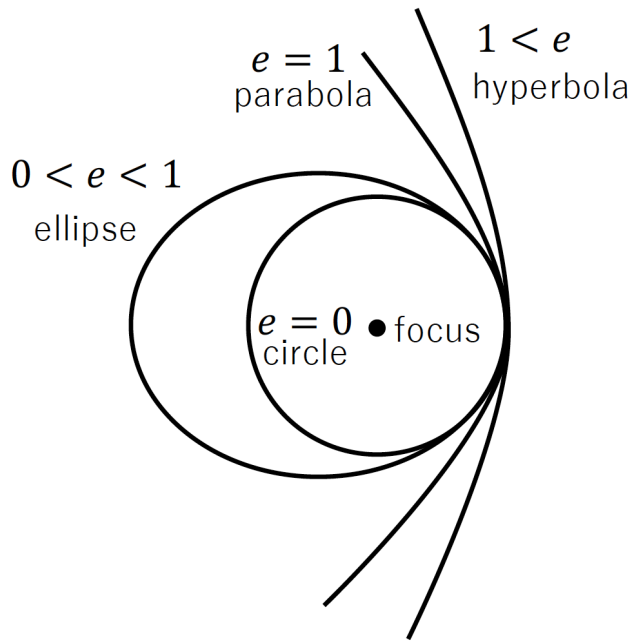

Figure 3.3: Classification of conical sections depending on eccentricity value.

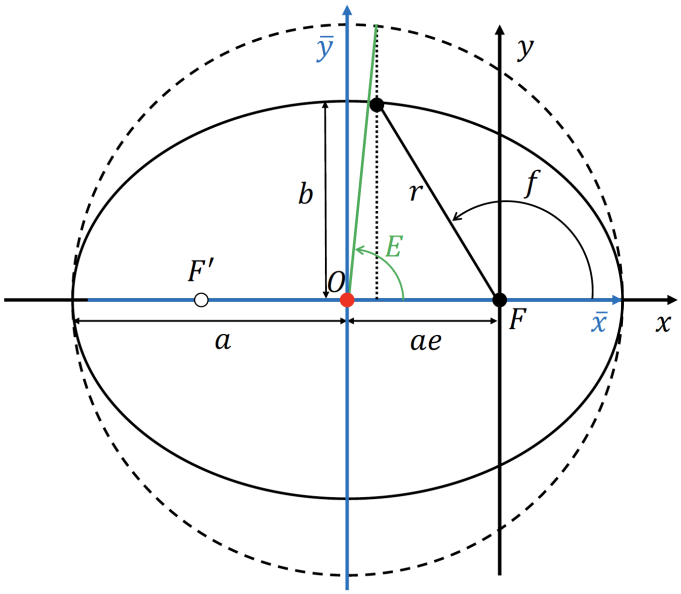

Figure 3.4: Definition of the eccentric anomaly E. The dashed circle is the circumscribed circle of ellipse with its centre at the centre of ellipse O. F and F' denote the focus and the empty focus, respectively.

Using the semi-major axis and true anomaly, equation (3.20) is written as

$$r = \frac{a(1-e^2)}{1+e\cos f}. \tag{3.22}$$

This is a conventional expression for the elliptical Keplerian orbit.

Integrating equation (3.16) over one period of an elliptical orbit P, we obtain the following relation:

$$\frac{1}{2}hP = \int_{\text{ellipse}} dA = \pi ab = \pi a^2\sqrt{1-e^2}. \tag{3.23}$$

Using equations (3.20) and (3.22),

$$\frac{h^2}{Gm_{\text{tot}}} = a(1-e^2) \;\rightarrow\; h = \sqrt{Gm_{\text{tot}}a(1-e^2)}. \tag{3.24}$$

Therefore, equation (3.23) becomes

$$P^2 = \frac{4\pi^2}{Gm_{\text{tot}}}a^3. \tag{3.25}$$

Equation (3.25) shows that the orbital period is independent of the eccentricity and only depends on semi-major axis and the total mass. This is Kepler's third law.

Since the angle f covers 2π radians during one orbital period, we can introduce a kind of averaged angular velocity, the "mean motion":

$$\nu \equiv \frac{2\pi}{P}, \tag{3.26}$$

which characterizes the Keplerian motion. In terms of a and ν, equations (3.24) and (3.25) are written as

$$h = \nu a^2\sqrt{1-e^2} \tag{3.27}$$

and

$$\nu^2 a^3 = Gm_{\text{tot}}. \tag{3.28}$$

We find that the specific angular momentum $\boldsymbol{h}$ is a constant of the motion. We next consider searching for another constant of the motion. Taking the scalar product of $\dot{\boldsymbol{r}}$ with equation (3.6),

$$\dot{\boldsymbol{r}}\cdot\ddot{\boldsymbol{r}} = -Gm_{\text{tot}}\frac{\dot{\boldsymbol{r}}\cdot\boldsymbol{r}}{r^3}. \tag{3.29}$$

Thus,

$$\frac{dC}{dt} \equiv \frac{d}{dt}\left(\frac{1}{2}\dot{\boldsymbol{r}}^2 - \frac{Gm_{\text{tot}}}{r}\right) = 0. \tag{3.30}$$

Equation (3.30) shows that C is a constant of the motion. Since C denotes the orbital energy per unit mass, it is called the "*vis viva* integral" or "specific orbital energy".

Consider writing C as a function of a, e, and $m_{\rm tot}$. Using equation (3.11), the square of velocity $\dot{\boldsymbol{r}}^2$ can be written as

$$\dot{\boldsymbol{r}}^2 = \dot{r}^2 + (r\dot{\theta})^2 = \dot{r}^2 + (r\dot{f})^2, \tag{3.31}$$

where $\dot{\theta} = \dot{f} + \dot{\varpi} = \dot{f}$. Using equations (3.16), (3.22) and (3.27),

$$r\dot{f} = \frac{h}{r} = \frac{\nu a}{\sqrt{1-e^2}}(1 + e\cos f) \tag{3.32}$$

and

$$\dot{r} = \frac{r\dot{f}e\sin f}{1 + e\cos f} = \frac{\nu a}{\sqrt{1-e^2}}e\sin f. \tag{3.33}$$

Therefore, $\dot{\boldsymbol{r}}^2$ is written as

$$\begin{aligned} \dot{\boldsymbol{r}}^2 &= \dot{r}^2 + (r\dot{f})^2 = \frac{n^2a^2}{1-e^2}(1 + 2e\cos f + e^2) \\ &= \frac{\nu^2a^2}{1-e^2}\left[\frac{2a(1-e^2)}{r} - (1-e^2)\right] = Gm_{\rm tot}\left(\frac{2}{r} - \frac{1}{a}\right). \end{aligned} \tag{3.34}$$

The specific orbital energy C is written down using the equations above:

$$C = \left(\frac{1}{2}\dot{\boldsymbol{r}}^2 - \frac{Gm_{\rm tot}}{r}\right) = -\frac{Gm_{\rm tot}}{2a}. \tag{3.35}$$

This equation shows that the orbital energy of elliptical motion is independent of the eccentricity and determined only by the semi-major axis and masses.

We have completed deriving the shape of orbit. However, the position of a body at a given time is still unknown. In order to determine the motion in a two-body problem, we derive the relation between the position and time as follows. Using equations (3.27), and (3.33) - (3.34), $\dot{r}$ reduces to

$$\dot{r} = \sqrt{\dot{\boldsymbol{r}}^2 - (r\dot{f})^2} = \frac{\nu a}{r}\sqrt{a^2e^2 - (r-a)^2}. \tag{3.36}$$

In order to integrate equation (3.36), we can introduce the "eccentric anomaly" E instead of the true anomaly f (Figure 3.4).

The equation of a centred ellipse is

$$\left(\frac{\bar{x}}{a}\right)^2 + \left(\frac{\bar{y}}{b}\right)^2 = 1, \tag{3.37}$$

where a is the semi-major axis, b is the semi-minor axis, and $(\bar{x}, \bar{y})$ is a set of co-ordinates in rectangular co-ordinates with the origin at the centre of ellipse (see Figure 3.4). Considering equations (3.21) and (3.37), Figure 3.4 shows

$$\bar{x} = a\cos E \tag{3.38}$$

and

$$\bar{y} = \sqrt{b^2\left[1 - \left(\frac{\bar{x}}{a}\right)^2\right]} = b\sin E = a\sqrt{1-e^2}\sin E. \tag{3.39}$$

Thus,

$$x = r\cos f = \bar{x} - ae = a\cos E - ae \tag{3.40}$$

and

$$y = r\sin f = \bar{y} = a\sqrt{1-e^2}\sin E. \tag{3.41}$$

Equations (3.40) and (3.41) immediately lead to the following equations:

$$r = \sqrt{x^2+y^2} = a(1 - e\cos E), \tag{3.42}$$

$$\sin f = \frac{y}{r} = \frac{\sqrt{1-e^2}\sin E}{1 - e\cos E}, \tag{3.43}$$

$$\cos f = \frac{x}{r} = \frac{\cos E - e}{1 - e\cos E}. \tag{3.44}$$

Using the eccentric anomaly, equation (3.36) becomes

$$\dot{E} = \frac{\nu}{1 - e\cos E}. \tag{3.45}$$

This equation can be integrated with respect to E and we obtain

$$M \equiv \nu(t - \tau) = E - e\sin E, \tag{3.46}$$

where M is called the "mean anomaly" and τ is an integration constant called the "time of pericentre passage". The mean anomaly denotes the angle of the averaged orbital motion. Equation (3.46), "Kepler's equation", is an important equation in celestial mechanics since its solution gives the position of body at a given time.

Since it is known that Kepler's equation cannot be solved as a simple analytical function of M, we need use either infinite expansion or numerical calculation. Consider solving Kepler's equation with the Fourier expansion. Since $E - M$ is an odd function from equation (3.46), it can be expanded as an infinite Fourier series of sine functions:

$$E - M = e\sin E = \sum_{s=1}^{\infty} b_s(e)\sin(sM), \tag{3.47}$$

where $b_s(e)$ are the coefficients depending only on e and given by

$$b_s(e) = \frac{2}{\pi}\int_0^{\pi} e\sin E\sin sM dM. \tag{3.48}$$

Using Kepler's equation and integrating by parts,

$$b_s(e) = \frac{2}{s\pi}\int_0^{\pi}\cos(sE - se\sin E)dE = \frac{2}{s}J_s(se), \tag{3.49}$$

where $J_s(se)$ are the Bessel functions. Therefore, Kepler's equation can be solved formally as

$$E = M + \sum_{s=1}^{\infty} \frac{2}{s} J_s(se) \sin(sM). \tag{3.50}$$

Computing this series, we can determine E for a given M. Note that it is known that this series diverges if $e > 0.6627434$ (e.g. Hagihara 1970) although it rapidly converges for small value of e

Using the formal expansion solution (3.50), we consider writing important functions of f in terms of e and M. We follows Kinoshita (2007) for this procedure. Differentiating Kepler's equation with respect to M and using equation (3.42), we obtain

$$\frac{\partial E}{\partial M} = \frac{1}{1 - e\cos E} = \frac{a}{r}. \tag{3.51}$$

Using equation (3.22), it leads to

$$\frac{a}{r} = 1 + 2\sum_{s=1}^{\infty} J_s(se)\cos(sM) \tag{3.52}$$

and

$$\cos f = -e + \frac{2(1-e^2)}{e} \sum_{s=1}^{\infty} J_s(se)\cos(sM). \tag{3.53}$$

Differentiating Kepler's equation with respect to e,

$$\frac{\partial E}{\partial e} = \frac{\sin E}{1 - e\cos E}. \tag{3.54}$$

From equation (3.43), we obtain

$$\sin f = \sqrt{1-e^2}\frac{\partial E}{\partial e} = 2\sqrt{1-e^2}\sum_{s=1}^{\infty} \frac{1}{s}\frac{\partial J_s(se)}{\partial e}\sin(sM). \tag{3.55}$$

Later, we can use these formulae to derive the radial velocity formula as a function of the mean anomaly.

Although we have obtained the relative motion of a body with respect to another body, it is important to consider the motion of two bodies with respect to the centre of mass in this system. This can be done as follows. Using equations (3.3) and (3.4), the position vectors for each body with respect to the centre of mass are

$$\boldsymbol{r}_1 - \boldsymbol{R} = -\frac{m_2}{m_1 + m_2}\boldsymbol{r} \tag{3.56}$$

and

$$\boldsymbol{r}_2 - \boldsymbol{R} = \frac{m_1}{m_1 + m_2}\boldsymbol{r}. \tag{3.57}$$

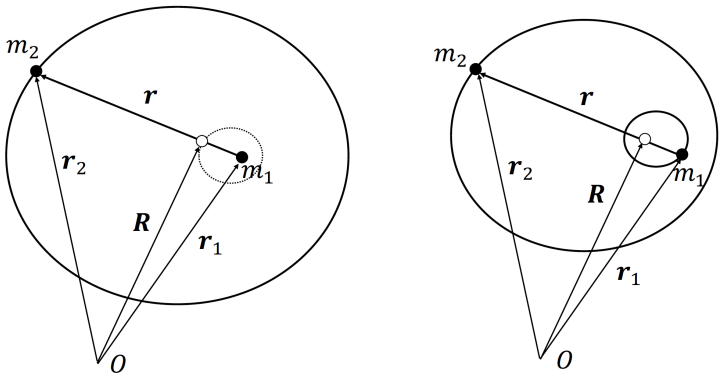

Figure 3.5: An orbit of the reletive position vector(left panel) and two orbits with respect to the centre of mass. The white circle denotes the centre of mass.

Equations (3.56) and (3.57) show that each orbit is the reduced orbit for relative motion (see Figure 3.5).

Next we consider a Keplerian orbit in three-dimentional space. Although a Keplerian orbit is always fixed on the plane, the orbit is not always on the same plane as the plane including our line of sight. Additionally, if we consider a system containing more than two bodies, the orbit is usually no longer fixed on one plane. Thus, it is important to consider an orbit in an arbitrary Cartesian frame.

Figure 3.6 shows the configuration we consider here. We take an arbitrary reference plane with the orthogonal unit vectors $\hat{\boldsymbol{X}}$ and $\hat{\boldsymbol{Y}}$, then we can take an unit vector $\hat{\boldsymbol{Z}}$ as $\hat{\boldsymbol{X}} \times \hat{\boldsymbol{Y}}$. $(\hat{\boldsymbol{X}}, \hat{\boldsymbol{Y}}, \hat{\boldsymbol{Z}})$ constitutes a set of base vectors. As shown in Figure 3.6, we need define some angles to express the orbit in a three dimentional space. The angle I between $\boldsymbol{h}$ and $\hat{\boldsymbol{Z}}$ is called the "inclination". When the inclination has non zero value, the orbit has two intersection points for the reference plane. The point of them where the body crosses the reference plane from below to above is especially called the "ascending node". The angle Ω between $\hat{\boldsymbol{X}}$ and the vector towards the ascending node is called the "longitude of ascending node" Finally, the angle ω between the vectors towards the ascending node and the pericentre is defined. It is called the "argument of pericentre". If $I \to 0$, the orbital plane coincides with the reference plane. In this case, from equation (3.20), $\varpi = \Omega + \omega$. We define ϖ as $\Omega + \omega$ even for an inclined case. The dog-leg angle ϖ is called the "longitude of pericentre". The set of parameters $(a, e, I, \Omega, \omega, \tau)$ defines a Keplerian orbit in space. Therefore, these parameters are called the "orbital elements". Instead of ω, ϖ is often used as one of orbital elements.

Using a set of orbital elements and rotating the co-ordinate system, we can write down the position of body (X, Y, Z) in the $(\hat{\boldsymbol{X}}, \hat{\boldsymbol{Y}}, \hat{\boldsymbol{Z}})$ frame. As in Figure 3.6, we consider setting the frame $(\hat{\boldsymbol{x}}, \hat{\boldsymbol{y}}, \hat{\boldsymbol{z}})$ with $\hat{\boldsymbol{x}}$ towards the pericentre and $\hat{\boldsymbol{z}}$ towards $\boldsymbol{h}$.

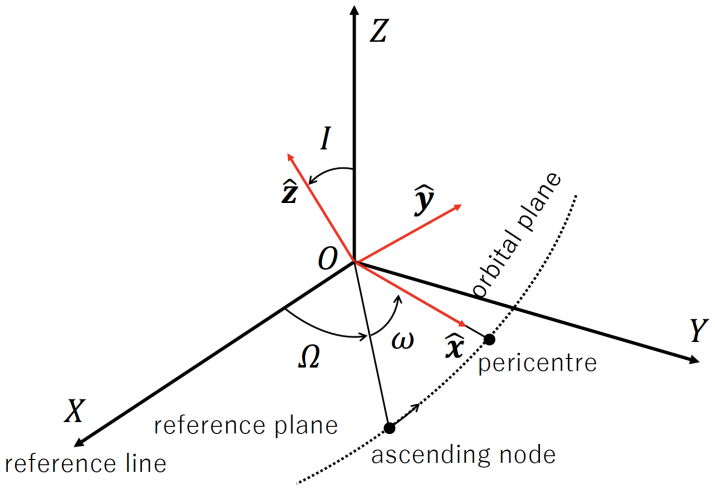

Figure 3.6: Keplerian orbit with respect to an arbitrary reference plane.

In this frame, the position of orbiting body can be written as

$$\begin{pmatrix} x \\ y \\ z \end{pmatrix} = \begin{pmatrix} r\cos f \\ r\sin f \\ 0 \end{pmatrix}. \tag{3.58}$$

Figure 3.6 shows that we can transform (x, y, z) to (X, Y, Z) combining three rotations $R_z(\omega)$, $R_x(I)$ and $R_z(\Omega)$ in order, where $R_i(j)$ is a rotation around i $(i = x, y, z)$ axis by j $(j = \omega, I, \Omega)$. Thus, we obtain the relation between (x, y, z) and (X, Y, Z) as follows:

$$\begin{pmatrix} X \\ Y \\ Z \end{pmatrix} = R_z(\Omega)R_x(I)R_z(\omega)\begin{pmatrix} x \\ y \\ z \end{pmatrix}, \tag{3.59}$$

where

$$R_z(\Omega) = \begin{pmatrix} \cos\Omega & -\sin\Omega & 0 \\ \sin\Omega & \cos\Omega & 0 \\ 0 & 0 & 1 \end{pmatrix}, \tag{3.60}$$

$$R_x(I) = \begin{pmatrix} 1 & 0 & 0 \\ 0 & \cos I & -\sin I \\ 0 & \sin I & \cos I \end{pmatrix}, \tag{3.61}$$

and

$$R_z(\omega) = \begin{pmatrix} \cos\omega & -\sin\omega & 0 \\ \sin\omega & \cos\omega & 0 \\ 0 & 0 & 1 \end{pmatrix}. \tag{3.62}$$

Equations (3.58) and (3.59) immediately yield

$$\begin{pmatrix} X \\ Y \\ Z \end{pmatrix} = r \begin{pmatrix} \cos\Omega\cos(\omega+f) - \sin\Omega\sin(\omega+f)\cos I \\ \sin\Omega\cos(\omega+f) + \cos\Omega\sin(\omega+f)\cos I \\ \sin(\omega+f)\sin I \end{pmatrix}. \tag{3.63}$$

The orbital velocity $\boldsymbol{V}$ in the (x, y, z) frame can be written using equations (3.33) and (3.32):

$$\boldsymbol{V} = \begin{pmatrix} V_x \\ V_y \\ V_z \end{pmatrix} \equiv \frac{d}{dt}\begin{pmatrix} r\cos f \\ r\sin f \\ 0 \end{pmatrix} = \frac{\nu a}{\sqrt{1-e^2}}\begin{pmatrix} -\sin f \\ \cos f + e \\ 0 \end{pmatrix}. \tag{3.64}$$

Since (X, Y, Z) frame is arbitrary, we can define the line towards the ascending node as X axis. In this frame, $\Omega = 0$ and $\omega = \varpi$. Using equation (3.59) to the velocity vector $\boldsymbol{V}$, the explicit form of $\boldsymbol{V}$ in terms of (X, Y, Z) frame is

$$\begin{aligned} \boldsymbol{V} &= R_z(0)R_x(I)R_z(\varpi)\begin{pmatrix} -\frac{\nu a}{\sqrt{1-e^2}}\sin f \\ \frac{\nu a}{\sqrt{1-e^2}}(\cos f + e) \\ 0 \end{pmatrix} \\ &= \frac{\nu a}{\sqrt{1-e^2}}\begin{pmatrix} -\sin(f+\varpi) - e\sin\varpi \\ [\cos(f+\varpi) + e\cos\varpi]\cos I \\ [\cos(f+\varpi) + e\cos\varpi]\sin I \end{pmatrix}. \end{aligned} \tag{3.65}$$

The velocity component of the orbiting body towards our line of sight is called the "radial velocity". Since the radial velocity can be directly observed using spectroscopic analysis, it is worth while to write down it explicitly. If we choose our line of sight as Z axis, the radial velocity $V_{\rm RV}$ can be written as

$$\begin{aligned} V_{\rm RV} = \boldsymbol{V}\cdot\begin{pmatrix} 0 \\ 0 \\ 1 \end{pmatrix} &= \frac{\nu a}{\sqrt{1-e^2}}\left[\cos(f+\varpi) + e\cos\varpi\right]\sin I \\ &= K\left[\cos(f+\varpi) + e\cos\varpi\right]. \end{aligned} \tag{3.66}$$

Note that the inclination I is the angle between the line of sight and $\boldsymbol{h}$ in this case (see Figure 3.7). In equation (3.66), the radial velocity semi-amplitude K is defined using equations (3.26) and (3.28) as

$$K \equiv \frac{\nu a}{\sqrt{1-e^2}}\sin I = \frac{1}{\sqrt{1-e^2}}\left(\frac{2\pi G m_{\rm tot}}{P}\right)^{\frac{1}{3}}\sin I. \tag{3.67}$$

Using equation (3.53), the radial velocity is written as a function of mean anomaly:

$$\begin{aligned} V_{\rm RV} = \frac{\nu a}{\sqrt{1-e^2}}\sin I\Bigg[&\frac{2(1-e^2)}{e}\cos\varpi\sum_{s=1}^{\infty}J_s(se)\cos(sM) \\ &-2\sqrt{1-e^2}\sin\varpi\sum_{s=1}^{\infty}\frac{\partial J_s(se)}{\partial e}\sin(sM)\Bigg]. \end{aligned} \tag{3.68}$$

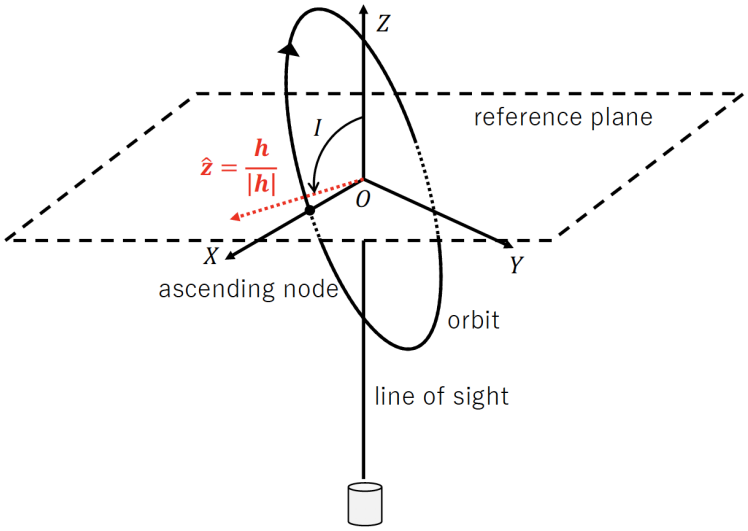

Figure 3.7: Schematic illustration for the concept of radial velocity.

The Bessel functions are expanded for $x \ll 1$ as

$$J_1(x) = \frac{1}{2}x - \frac{1}{16}x^3 + \mathcal{O}(x^5), \tag{3.69}$$

$$J_2(x) = \frac{1}{8}x^2 + \mathcal{O}(x^4), \tag{3.70}$$

and

$$J_i(x) = \mathcal{O}(x^i) \ (i \geq 3). \tag{3.71}$$

Thus, the radial velocity up to $\mathcal{O}(e)$ can be written as

$$V_{\rm RV} \approx [\nu a \cos(M + \varpi) + \nu a e \cos\varpi \cos(2M) - \nu a e \sin\varpi \sin(2M)] \sin I \tag{3.72}$$

or

$$V_{\rm RV} \approx [\nu a \cos\lambda + \nu a e \cos\varpi \cos(2\lambda) + \nu a e \sin\varpi \sin(2\lambda)] \sin I, \tag{3.73}$$

where $\lambda \equiv M + \varpi$. λ is called the "mean longitude". Since the mean anomaly is defined as $\nu(t - \tau)$ in equation (3.46), the mean longitude is rewritten as

$$\lambda = M + \varpi = \nu t + (\varpi - \nu\tau) \equiv \nu t + \tilde{\epsilon}, \tag{3.74}$$

where $\tilde{\epsilon}$ is called the "mean longitude at epoch", and often used as one of orbital elements instead of τ.

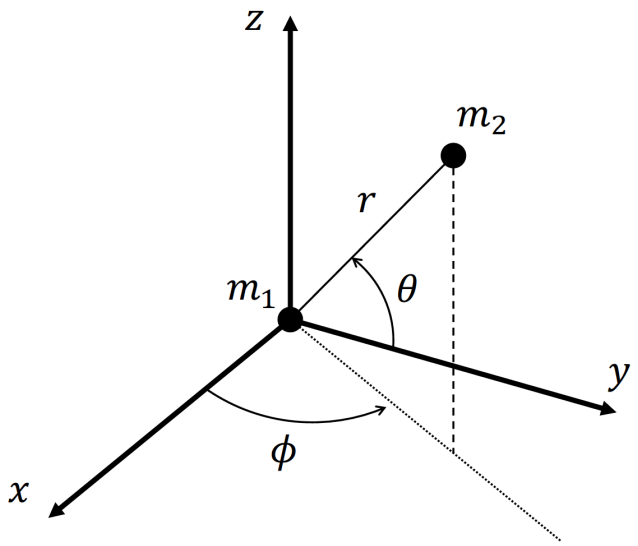

Figure 3.8: A relative motion in two-body system in terms of spherical co-ordinates.

3.2 Perturbation theory

In the previous section, we consider the motion in a two-body system and define the orbital elements. In a two-body problem, the orbital elements are constant with time and completely specify an overall motion (i.e., Keplerian motion). However, the motions of bodies should not follow one specific Keplerian motion if perturbing forces act on the system.

Even if perturbing forces exist, we can always define the unique orbital elements at a given time using the instantaneous position and velocity vectors of bodies. These orbital elements are called the "osculating elements" since they specify the instantaneous Keplerian motion, which is the motion that the bodies would follow if the perturbing force acting on the system were to dissapear suddenly. The osculating elements are not constant with time.

In this section, we switch to the perturbation theory and derive the "Lagrange planetary equations", the differential equations for orbital elements. These equations are used to describe the motions of bodies in a hierarchical three-body system later. The perturbation theory is described in many standard textbooks of celestial mechanics (e.g. Brouwer & Clemence 1961; Danby 1988; Moulton 1914; Murray & Dermott 2000; Valtonen & Karttunen 2006). In this section, we specifically follow Valtonen & Karttunen (2006) and Danby (1988). Another method called the "variation of constants" to derive the equations is described in Appendix C.

Consider a Hamiltonian $\mathcal{H}$ for a relative motion in a two-body system with a perturbation potential $-\mathcal{R}$. The $\mathcal{R}$ is called the "disturbing function". The minus sign is a convention in celestial mechanics. The disturbing function represents any external

forces, but usually comes from multi-body interaction terms. The Hamiltonian is written down in terms of spherical co-ordinate system illustrated in Figure 3.8 as

$$\mathcal{H} = \frac{1}{2\mu}\left(p_r^2 + \frac{p_\theta^2}{r^2} + \frac{p_\phi^2}{r^2\cos^2\theta}\right) - \frac{G\mu m_{\text{tot}}}{r} - \mathcal{R}, \tag{3.75}$$

where μ is the reduced mass and m_{tot} is the total mass. First, we consider the case that $\mathcal{R} = 0$. The Hamilton-Jacobi equation is

$$\frac{\partial S}{\partial t} + \mathcal{H}\left(\boldsymbol{q}, \frac{\partial S}{\partial \boldsymbol{q}}\right) = 0, \tag{3.76}$$

where $\boldsymbol{q} \equiv (r, \theta, \phi)$ and S is the action. Therefore, for the Hamiltonian $\mathcal{H}$ in equation (3.75) with $\mathcal{R} = 0$, the explicit form of the Hamilton-Jacobi equation is written as

$$\frac{\partial S}{\partial t} + \frac{1}{2\mu}\left[\left(\frac{\partial S}{\partial r}\right)^2 + \frac{1}{r^2}\left(\frac{\partial S}{\partial \theta}\right)^2 + \frac{1}{r^2\cos^2\theta}\left(\frac{\partial S}{\partial \phi}\right)^2\right] - \frac{G\mu m_{\text{tot}}}{r} = 0. \tag{3.77}$$

It is known that the action S is totally separable in a two-body problem. Thus, we can set

$$S = S_r(r) + S_\theta(\theta) + S_\phi(\phi) + S_t(t). \tag{3.78}$$

Substituting equation (3.78), equation (3.77) can be separated into the following series of equations:

$$\frac{dS_t}{dt} = -\alpha_1, \tag{3.79}$$

$$\frac{dS_\phi}{d\phi} = \alpha_3, \tag{3.80}$$

$$\left(\frac{dS_\theta}{d\theta}\right)^2 + \frac{\alpha_3^2}{\cos^2\theta} = \alpha_2^2, \tag{3.81}$$

and

$$\left(\frac{dS_r}{dr}\right)^2 + \frac{\alpha_2^2}{r^2} = 2\mu\left(\alpha_1 + \frac{G\mu m_{\text{tot}}}{r}\right), \tag{3.82}$$

where α_1, α_2 and α_3 are constants. Integrating equations (3.79) - (3.82), we obtain

$$S = -\alpha_1 t + \alpha_3\phi + \int^\theta \sqrt{\alpha_2^2 - \frac{\alpha_3^2}{\cos^2\theta}}d\theta + \int^r \sqrt{2\mu\left(\alpha_1 + \frac{G\mu m_{\text{tot}}}{r}\right) - \frac{\alpha_2^2}{r^2}}dr. \tag{3.83}$$

In order to understand physical meaning of the constants α_1, α_2 and α_3, we consider the specific angular momentum $\boldsymbol{h}$ using (r, θ, ϕ):

$$\begin{aligned}\boldsymbol{h} \equiv \boldsymbol{r} \times \dot{\boldsymbol{r}} &= \begin{pmatrix} r\cos\theta\cos\phi \\ r\cos\theta\sin\phi \\ r\sin\theta \end{pmatrix} \times \frac{d}{dt}\begin{pmatrix} r\cos\theta\cos\phi \\ r\cos\theta\sin\phi \\ r\sin\theta \end{pmatrix} \\ &= r^2\begin{pmatrix} \dot{\theta}\sin\phi - \dot{\phi}\sin\theta\cos\theta\cos\phi \\ -\dot{\theta}\cos\phi - \dot{\phi}\sin\theta\cos\theta\sin\phi \\ \dot{\phi}\cos^2\theta \end{pmatrix}.\end{aligned} \tag{3.84}$$

Thus,

$$h^2 = (r^2)^2(\dot{\theta}^2 + \cos^2\theta\dot{\phi}^2). \tag{3.85}$$

Using equations (3.77) - (3.85), the constants α_1, α_2 and α_3 are given as

$$\alpha_1 = -\frac{\partial S}{\partial t} = \mathcal{H}, \tag{3.86}$$

$$\alpha_3 = p_\phi = \mu(r\cos\theta)^2\dot{\phi} = \mu h_z, \tag{3.87}$$

$$\alpha_2^2 = \left(\frac{\partial S_\theta}{\partial\theta}\right)^2 + \frac{\alpha_3^2}{\cos^2\theta} = (\mu r^2)^2(\dot{\theta}^2 + \cos^2\theta\dot{\phi}^2) = (\mu h)^2. \tag{3.88}$$

These equations show that α_1, α_2 and α_3 correspond to the orbital energy, the magnitude of angular momentum and the z component of angular momentum, respectively. Thus, they are related to the orbital elements as

$$\alpha_1 = -\frac{G\mu m_{\rm tot}}{2a}, \tag{3.89}$$

$$\alpha_2 = \mu\sqrt{Gm_{\rm tot}a(1-e^2)} \tag{3.90}$$

and

$$\alpha_3 = \mu\sqrt{Gm_{\rm tot}a(1-e^2)}\cos I. \tag{3.91}$$

Since α_1, α_2 and α_3 are constant, it is useful to consider the canonical transformation which constitutes $(\alpha_1, \alpha_2, \alpha_3)$ as the generalized momenta (P_1, P_2, P_3). Then, the corresponding generalized co-ordinates Q_1, Q_2 and Q_3 are computed from S as

$$Q_1 = \frac{\partial S}{\partial\alpha_1} = -t + \int\frac{\mu dr}{\sqrt{2\mu(\alpha_1 + G\mu m_{\rm tot}/r) - \alpha_2^2/r^2}}, \tag{3.92}$$

$$\begin{aligned} Q_2 &= \frac{\partial S}{\partial\alpha_2} \\ &= \alpha_2\int\frac{d\theta}{\sqrt{\alpha_2^2 - \alpha_3^2/\cos^2\theta}} - \frac{\alpha_2}{\mu}\int\frac{\mu}{r^2\sqrt{2\mu(\alpha_1 + G\mu m_{\rm tot}/r) - \alpha_2^2/r^2}}, \end{aligned} \tag{3.93}$$

and

$$Q_3 = \frac{\partial S}{\partial\alpha_3} = \phi - \alpha_3\int\frac{d\theta}{\cos^2\theta\sqrt{\alpha_2^2 - \alpha_3^2/\cos^2\theta}}. \tag{3.94}$$

Using equations (3.86) and (3.90),

$$Q_1 = -t + \frac{1}{\sqrt{Gm_{\rm tot}}}\int\frac{rdr}{\sqrt{-r^2/a + 2r - a(1-e^2)}}. \tag{3.95}$$

Introducing a new variable E as $r = a(1 - e\cos E)$ and using Kepler's equation,

$$Q_1 = -t + \sqrt{\frac{a^3}{Gm_{\rm tot}}}(E - e\sin E) = -\tau, \tag{3.96}$$

where τ is the pericentre passage.

Similarly, using equation (3.86) - (3.91), we obtain

$$Q_2 = \int \frac{d\theta}{\sqrt{1-\cos^2 I/\cos^2\theta}} - \frac{\alpha_2}{\sqrt{(Gm_{\rm tot})^3}} \int \frac{dr}{r^2\sqrt{-1/a+2/r-a(1-e^2)/r^2}}. \quad (3.97)$$

Using equation (3.63), we obtain the following variable transformation:

$$\sin\theta = \sin(\omega+f)\sin I. \quad (3.98)$$

Therefore, the first integral in equation (3.97) is

$$\int \frac{d\theta}{\sqrt{1-\cos^2 I/\cos^2\theta}} = \omega + f. \quad (3.99)$$

If we use the variable transformation in equation (3.22), the second integral in equation (3.97) can be written as follows:

$$\frac{\alpha_2}{\sqrt{(Gm_{\rm tot})^3}} \int \frac{dr}{r^2\sqrt{-1/a+2/r-a(1-e^2)/r^2}} = f. \quad (3.100)$$

Combining equations (3.99) and (3.100), we obtain

$$Q_2 = \omega. \quad (3.101)$$

Finally, using (3.88) and (3.91),

$$Q_3 = \phi - \int \frac{\cos I d\theta}{\cos^2\theta\sqrt{1-\cos^2 I/\cos^2\theta}}. \quad (3.102)$$

Using equations (3.63) and (3.98),

$$\sin(\phi-\Omega) = \tan\theta\cot I. \quad (3.103)$$

The integral in equation (3.102) can be calculated using the variable transformation above:

$$\int \frac{\cos I d\theta}{\cos^2\theta\sqrt{1-\cos^2 I/\cos^2\theta}} = \phi - \Omega. \quad (3.104)$$

Thus, equation (3.102) reduces to

$$Q_3 = \Omega. \quad (3.105)$$

As a result, the set of canonical variables $(Q_1, Q_2, Q_3, P_1, P_2, P_3)$ is written down as follows:

$$\begin{pmatrix} Q_1 \\ Q_2 \\ Q_3 \\ P_1 \\ P_2 \\ P_3 \end{pmatrix} = \begin{pmatrix} -\tau \\ \omega \\ \Omega \\ -\dfrac{G\mu m_{\rm tot}}{2a} \\ \mu\sqrt{Gm_{\rm tot}a(1-e^2)} \\ \mu\sqrt{Gm_{\rm tot}a(1-e^2)}\cos I \end{pmatrix}. \quad (3.106)$$

In terms of these canonical variables, the Hamiltonian is constantly zero.

In celestial mechanics, usually the canonial variables $(\boldsymbol{Q'}, \boldsymbol{P'})$ called the "Delaunay variables" are often used. Consider a generating function $F(\boldsymbol{Q}, \boldsymbol{P'})$:

$$F(\boldsymbol{Q}, \boldsymbol{P'}) \equiv \left(P'_1 - \frac{Gm_{\rm tot}\mu}{2\nu a} \right) \nu(t + Q_1) + Q_2 P'_2 + Q_3 P'_3. \tag{3.107}$$

Thus, the Delaunay variables are

$$\begin{pmatrix} Q'_1 \\ Q'_2 \\ Q'_3 \\ P'_1 \\ P'_2 \\ P'_3 \end{pmatrix} = \begin{pmatrix} M \\ \omega \\ \Omega \\ \mu\sqrt{Gm_{\rm tot}a} \\ \mu\sqrt{Gm_{\rm tot}a(1-e^2)} \\ \mu\sqrt{Gm_{\rm tot}a(1-e^2)}\cos I \end{pmatrix}. \tag{3.108}$$

The Hamiltonian in terms of the Delaunay variables is

$$\mathcal{H}' = \frac{\partial F}{\partial t} = -\frac{(Gm_{\rm tot})^2\mu^3}{2P'^2_1}. \tag{3.109}$$

This Hamiltonian shows that only Q'_1 evolves with time and other variables are constant if the disturbing function $\mathcal{R} = 0$.

If $\mathcal{R} \neq 0$, the Delaunay variables change with time. In this case, the Hamiltonian in terms of the Delaunay variables is

$$\mathcal{H}' = -\frac{(Gm_{\rm tot})^2\mu^3}{2P'^2_1} - \mathcal{R}. \tag{3.110}$$

Substituting $\mathcal{H}'$ into the canonical equations for the Delaunay variables and using equation (3.108), we obtain

$$\dot{Q}'_1 = \dot{M} = \frac{(Gm_{\rm tot})^2\mu^3}{P'^3_1} - \frac{\partial \mathcal{R}}{\partial P'_1}, \tag{3.111}$$

$$\dot{P}'_1 = \frac{\mu\sqrt{Gm_{\rm tot}}}{2\sqrt{a}}\dot{a} = \frac{\partial \mathcal{R}}{\partial Q'_1}, \tag{3.112}$$

$$\dot{Q}'_2 = \dot{\omega} = -\frac{\partial \mathcal{R}}{\partial P'_2}, \tag{3.113}$$

$$\dot{P}'_2 = \frac{\mu\sqrt{Gm_{\rm tot}(1-e^2)}}{2\sqrt{a}}\dot{a} - \frac{\mu\sqrt{Gm_{\rm tot}a}}{\sqrt{1-e^2}}e\dot{e} = \frac{\partial \mathcal{R}}{\partial Q'_2}, \tag{3.114}$$

$$\dot{Q}'_3 = \dot{\Omega} = -\frac{\partial \mathcal{R}}{\partial P'_3}, \tag{3.115}$$

and

$$\begin{aligned}\dot{P}_3' &= \frac{\mu\sqrt{Gm_{\rm tot}(1-e^2)}}{2\sqrt{a}}\cos I\dot{a} - \frac{\mu\sqrt{Gm_{\rm tot}a}}{\sqrt{1-e^2}}e\cos I\dot{e} - \mu\sqrt{Gm_{\rm tot}a(1-e^2)}\sin I\dot{I} \\ &= \frac{\partial\mathcal{R}}{\partial Q_3'}.\end{aligned} \tag{3.116}$$

Using equation (3.108),

$$a = \frac{P_1'^2}{\mu^2 Gm_{\rm tot}}, \tag{3.117}$$

$$e = \sqrt{1-\frac{P_2'^2}{P_1'^2}}, \tag{3.118}$$

$$\cos I = \frac{P_3'}{P_2'}, \tag{3.119}$$

$$\lambda = Q_1' + Q_2' + Q_3', \tag{3.120}$$

$$\varpi = Q_2' + Q_3' \tag{3.121}$$

and

$$\Omega = Q_3'. \tag{3.122}$$

Thus,

$$\frac{\partial\mathcal{R}}{\partial P_1'} = \frac{2\sqrt{a}}{\mu\sqrt{Gm_{\rm tot}}}\frac{\partial\mathcal{R}}{\partial a} + \frac{1-e^2}{\mu e\sqrt{Gm_{\rm tot}a}}\frac{\partial\mathcal{R}}{\partial e}, \tag{3.123}$$

$$\frac{\partial\mathcal{R}}{\partial P_2'} = -\frac{\sqrt{1-e^2}}{\mu e\sqrt{Gm_{\rm tot}a}}\frac{\partial\mathcal{R}}{\partial e} + \frac{\cos I}{\mu\sqrt{Gm_{\rm tot}a(1-e^2)}\sin I}\frac{\partial\mathcal{R}}{\partial I} \tag{3.124}$$

$$\frac{\partial\mathcal{R}}{\partial P_3'} = -\frac{1}{\mu\sqrt{Gm_{\rm tot}a(1-e^2)}\sin I}\frac{\partial\mathcal{R}}{\partial I}, \tag{3.125}$$

$$\frac{\partial\mathcal{R}}{\partial Q_1'} = \frac{\partial\mathcal{R}}{\partial\lambda}, \tag{3.126}$$

$$\frac{\partial\mathcal{R}}{\partial Q_2'} = \frac{\partial\mathcal{R}}{\partial\lambda} + \frac{\partial\mathcal{R}}{\partial\varpi} \tag{3.127}$$

and

$$\frac{\partial\mathcal{R}}{\partial Q_3'} = \frac{\partial\mathcal{R}}{\partial\lambda} + \frac{\partial\mathcal{R}}{\partial\varpi} + \frac{\partial\mathcal{R}}{\partial\Omega}. \tag{3.128}$$

Substituting equations (3.123) - (3.128) into equations (3.112) - (3.115), we obtain

$$\dot{a} = \frac{2}{\mu\nu a}\frac{\partial\mathcal{R}}{\partial\lambda}, \tag{3.129}$$

$$\dot{\varpi} = \dot{\omega} + \dot{\Omega} = \frac{\sqrt{1-e^2}}{\mu\nu a^2 e}\frac{\partial\mathcal{R}}{\partial e} + \frac{\tan\frac{I}{2}}{\mu\nu a^2\sqrt{1-e^2}}\frac{\partial\mathcal{R}}{\partial I}, \tag{3.130}$$

$$\dot{e} = -\frac{\sqrt{1-e^2}(1-\sqrt{1-e^2})}{\mu\nu a^2 e}\frac{\partial \mathcal{R}}{\partial \lambda} - \frac{\sqrt{1-e^2}}{\mu\nu a^2 e}\frac{\partial \mathcal{R}}{\partial \varpi}, \tag{3.131}$$

$$\dot{\Omega} = \frac{1}{\mu\nu a^2\sqrt{1-e^2}\sin I}\frac{\partial \mathcal{R}}{\partial I}, \tag{3.132}$$

$$\begin{aligned}\dot{\tilde{\epsilon}} &= \dot{M} + \dot{\varpi} - \frac{d}{dt}(\nu t) \\ &= -\frac{2}{\mu\nu a}\frac{\partial \mathcal{R}}{\partial a} + \frac{\sqrt{1-e^2}(1-\sqrt{1-e^2})}{\mu\nu a^2 e}\frac{\partial \mathcal{R}}{\partial e} + \frac{\tan\frac{I}{2}}{\mu\nu a^2\sqrt{1-e^2}}\frac{\partial \mathcal{R}}{\partial I} - \dot{\nu} t\end{aligned} \tag{3.133}$$

and

$$\dot{I} = -\frac{\tan\frac{I}{2}}{\mu\nu a^2\sqrt{1-e^2}}\left(\frac{\partial \mathcal{R}}{\partial \lambda} + \frac{\partial \mathcal{R}}{\partial \varpi}\right) - \frac{1}{\mu\nu a^2\sqrt{1-e^2}\sin I}\frac{\partial \mathcal{R}}{\partial \Omega}. \tag{3.134}$$

Note that a dependence in ν is not considered when we calculate $\frac{\partial \mathcal{R}}{\partial a}$ since a and λ are independent in terms of the Delaunay variables and ν only appears in λ. The term $\dot{\nu}t$ in equation (3.133) is called secular term since it increases with time. This behaviour is problematic when we solve this equation either approximately or numerically. In order to avoid this problem, we introduce the "new longitude at epoch" ϵ as

$$\epsilon \equiv \lambda - \int_0^t \nu dt'. \tag{3.135}$$

Using ϵ instead of $\tilde{\epsilon}$, equation (3.133) is modified to

$$\begin{aligned}\dot{\epsilon} &= \dot{\lambda} - \nu = \dot{M} + \dot{\varpi} - \nu \\ &= -\frac{2}{\mu\nu a}\frac{\partial \mathcal{R}}{\partial a} + \frac{\sqrt{1-e^2}(1-\sqrt{1-e^2})}{\mu\nu a^2 e}\frac{\partial \mathcal{R}}{\partial e} + \frac{\tan\frac{I}{2}}{\mu\nu a^2\sqrt{1-e^2}}\frac{\partial \mathcal{R}}{\partial I}.\end{aligned} \tag{3.136}$$

A series of equations (3.129) - (3.134) and (3.136) are the "Lagrange planetary equations", the differential equations for six orbital elements.

Equations (3.130) and (3.131) include e in denominators. It causes singularity when $e \to 0$. In order to avoid the singularities, it is convenient to define the vertical and horizontal components of eccentricity:

$$h \equiv e\sin\varpi \tag{3.137}$$

and

$$k \equiv e\cos\varpi. \tag{3.138}$$

Using these variables, equation (3.130) and (3.131) are modified to

$$\dot{h} = \frac{1}{\mu\nu a^2}\sqrt{1-e^2}\frac{\partial \mathcal{R}}{\partial k} + \frac{k}{\mu\nu a^2}\frac{\tan\frac{I}{2}}{\sqrt{1-e^2}}\frac{\partial \mathcal{R}}{\partial I} - \frac{h}{\mu\nu a^2}\frac{\sqrt{1-e^2}}{1+\sqrt{1-e^2}}\frac{\partial \mathcal{R}}{\partial \lambda}. \tag{3.139}$$

and

$$\dot{k} = -\frac{1}{\mu\nu a^2}\sqrt{1-e^2}\frac{\partial \mathcal{R}}{\partial h} - \frac{h}{\mu\nu a^2}\frac{\tan\frac{I}{2}}{\sqrt{1-e^2}}\frac{\partial \mathcal{R}}{\partial I} - \frac{k}{\mu\nu a^2}\frac{\sqrt{1-e^2}}{1+\sqrt{1-e^2}}\frac{\partial \mathcal{R}}{\partial \lambda}. \tag{3.140}$$

These equations do not include singularities when $e \to 0$.

For equations (3.132) and (3.134), we encounter the same problem as above when $I \to 0$. This can be avoided by introducing the following variables:

$$\mathcal{P} \equiv \sin I \sin \Omega \tag{3.141}$$

and

$$\mathcal{Q} \equiv \sin I \cos \Omega. \tag{3.142}$$

Using these variables, equations (3.132) and (3.134) are modified to

$$\dot{\mathcal{P}} = \frac{\cos I}{\mu\nu a^2\sqrt{1-e^2}}\frac{\partial \mathcal{R}}{\partial \mathcal{Q}} - \frac{1}{\mu\nu a^2}\frac{\mathcal{P}\cos I}{\sqrt{1-e^2}(1+\cos I)}\left(\frac{\partial \mathcal{R}}{\partial \varpi} + \frac{\partial \mathcal{R}}{\partial \lambda}\right) \tag{3.143}$$

and

$$\dot{\mathcal{Q}} = -\frac{\cos I}{\mu\nu a^2\sqrt{1-e^2}}\frac{\partial \mathcal{R}}{\partial \mathcal{P}} - \frac{1}{\mu\nu a^2}\frac{\mathcal{Q}\cos I}{\sqrt{1-e^2}(1+\cos I)}\left(\frac{\partial \mathcal{R}}{\partial \varpi} + \frac{\partial \mathcal{R}}{\partial \lambda}\right). \tag{3.144}$$

Again, these equations do not have singularities when $I \to 0$.

3.3 Hierarchical three-body problem

In this section, we consider a system consisting of three point particles with masses m_1, m_2 and m_3. They interact each other only by the Newtonian gravitational force. Defining $\boldsymbol{r}_1$, $\boldsymbol{r}_2$ and $\boldsymbol{r}_3$ as the position vectors of m_1, m_2 and m_3 in an arbitrary Cartesian co-ordinates, the Lagrangian $\mathcal{L}$ of the system is

$$\mathcal{L} = \frac{1}{2}m_1\dot{\boldsymbol{r}}_1^2 + \frac{1}{2}m_2\dot{\boldsymbol{r}}_2^2 + \frac{1}{2}m_3\dot{\boldsymbol{r}}_3^2 + \frac{Gm_1m_2}{|\boldsymbol{r}_2-\boldsymbol{r}_2|} + \frac{Gm_1m_3}{|\boldsymbol{r}_3-\boldsymbol{r}_1|} + \frac{Gm_2m_3}{|\boldsymbol{r}_3-\boldsymbol{r}_2|}. \tag{3.145}$$

In what follows, we consider a hierarchcial three-body system as illustrated in Figure 3.9. A hierarchical three-body system is defined as the system consisting of two well-separated orbits such that gravitational interactions can be treated as a summation of the term constructing two Keplerian orbits and a small perturbation on each orbit. For a hierarchical three-body problem, it is convenient to use the Jacobian co-ordinates instead of $\boldsymbol{r}_1$, $\boldsymbol{r}_2$ and $\boldsymbol{r}_3$.

The position vectors $\boldsymbol{r}_{\rm CM}$, $\boldsymbol{r}$ and $\boldsymbol{R}$ in the Jacobian co-ordinates are defined as

$$\boldsymbol{r}_{\rm CM} \equiv \frac{m_1\boldsymbol{r}_1 + m_2\boldsymbol{r}_2 + m_3\boldsymbol{r}_3}{m_{123}}, \tag{3.146}$$

$$\boldsymbol{r} \equiv \boldsymbol{r}_2 - \boldsymbol{r}_1 \tag{3.147}$$

and

$$\boldsymbol{R} \equiv \boldsymbol{r}_3 - \frac{m_1\boldsymbol{r}_1 + m_2\boldsymbol{r}_2}{m_{12}}, \tag{3.148}$$

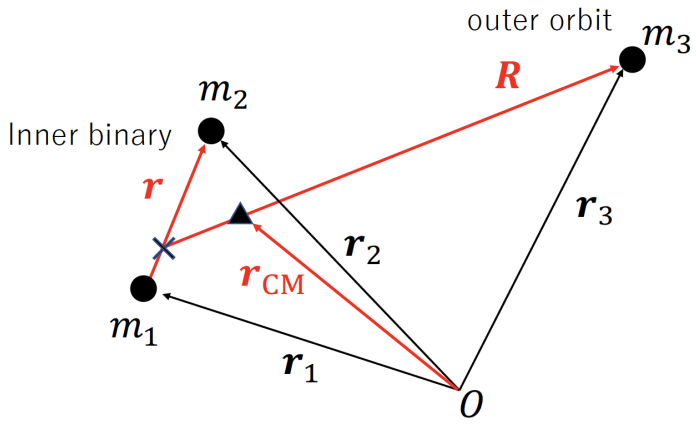

Figure 3.9: A hierarchical three-body system in terms of the Jacobian co-ordinate system. The cross denotes the centre of mass for inner binary. The triangle denotes the centre of mass of system.

where $m_{12} \equiv m_1 + m_2$ and $m_{123} \equiv m_1 + m_2 + m_3$. The $\boldsymbol{r}_{\rm CM}$ physically means the position vector for the centre of mass of this system. The $\boldsymbol{r}$ means the relative position vector of m_2 with respect to m_1. The $\boldsymbol{R}$ means the position vector of m_3 with respect to the centre of mass of inner binary. Using equations (3.146) - (3.148), we find

$$\boldsymbol{r}_1 = \boldsymbol{r}_{\rm CM} - \frac{m_2}{m_{12}}\boldsymbol{r} - \frac{m_3}{m_{123}}\boldsymbol{R}, \tag{3.149}$$

$$\boldsymbol{r}_2 = \boldsymbol{r}_{\rm CM} + \frac{m_1}{m_{12}}\boldsymbol{r} - \frac{m_3}{m_{123}}\boldsymbol{R} \tag{3.150}$$

and

$$\boldsymbol{r}_3 = \boldsymbol{r}_{\rm CM} + \frac{m_{12}}{m_{123}}\boldsymbol{R}. \tag{3.151}$$

Therefore, the Lagrangian (3.145) is written in the Jacobian co-ordinates as

$$\mathcal{L} = \frac{1}{2}m_{123}\dot{\boldsymbol{r}}_{\rm CM}^2 + \frac{1}{2}\mu_{\rm in}\dot{\boldsymbol{r}}^2 + \frac{1}{2}\mu_{\rm out}\dot{\boldsymbol{R}}^2 + \frac{Gm_1m_2}{|\boldsymbol{r}|} + \frac{Gm_1m_3}{|\boldsymbol{R} - \beta_2\boldsymbol{r}|} + \frac{Gm_2m_3}{|\boldsymbol{R} - \beta_1\boldsymbol{r}|}, \tag{3.152}$$

where $\mu_{\rm in} \equiv m_1m_2/m_{12}$, $\mu_{\rm out} \equiv m_3m_{12}/m_{123}$, $\beta_1 \equiv m_1/m_{12}$, and $\beta_2 \equiv -m_2/m_{12}$. The momenta corresponding to $\boldsymbol{r}_{\rm CM}$, $\boldsymbol{r}$ and $\boldsymbol{R}$ are calculated using $\mathcal{L}$:

$$\boldsymbol{p}_{\rm CM} \equiv \frac{\partial\mathcal{L}}{\partial\dot{\boldsymbol{r}}_{\rm CM}} = m_{123}\dot{\boldsymbol{r}}_{\rm CM}, \tag{3.153}$$

$$\boldsymbol{p} \equiv \frac{\partial\mathcal{L}}{\partial\dot{\boldsymbol{r}}} = \mu_{\rm in}\dot{\boldsymbol{r}}, \tag{3.154}$$

and

$$\boldsymbol{P} \equiv \frac{\partial \mathcal{L}}{\partial \dot{\boldsymbol{R}}} = \mu_{\rm out} \dot{\boldsymbol{R}}. \tag{3.155}$$

Therefore, the Hamiltonian $\mathcal{H}$ of this system is

$$\begin{aligned} \mathcal{H} &\equiv \dot{\boldsymbol{r}}_{\rm CM} \cdot \boldsymbol{p}_{\rm CM} + \dot{\boldsymbol{r}} \cdot \boldsymbol{p} + \dot{\boldsymbol{R}} \cdot \boldsymbol{P} - \mathcal{L} \\ &= \frac{\boldsymbol{p}_{\rm CM}^2}{2m_{123}} + \left(\frac{\boldsymbol{p}^2}{2\mu_{\rm in}} - \frac{Gm_{12}\mu_{\rm in}}{|\boldsymbol{r}|} \right) + \left(\frac{\boldsymbol{P}^2}{2\mu_{\rm out}} - \frac{Gm_{123}\mu_{\rm out}}{|\boldsymbol{R}|} \right) \\ &- \left(-\frac{Gm_{12}m_3}{|\boldsymbol{R}|} + \frac{Gm_1m_3}{|\boldsymbol{R} - \beta_2\boldsymbol{r}|} + \frac{Gm_2m_3}{|\boldsymbol{R} - \beta_1\boldsymbol{r}|} \right). \end{aligned} \tag{3.156}$$

Note that $m_{12}\mu_{\rm in} = m_1m_2$ and $m_{123}\mu_{\rm out} = m_{12}m_3$. The equation above shows that the Hamiltonian $\mathcal{H}$ consists of four terms with different physical meanings. The first term in equation (3.156) corresponds to the constant motion of the centre of mass. Since it is irrelevant to the motion of bodies due to the gravitational interaction, we need not consider this term in the following analysis. The second term describes the Keplerian orbit of the inner binary. This term shows that the Keplerian motion of the inner binary is equivalent to that for a two-body system consisting of m_1 and m_2. Thus, we can define the mean motion of inner binary $\nu_{\rm in}$ as

$$\nu_{\rm in} \equiv \sqrt{\frac{Gm_{12}}{a_{\rm in}^3}}, \tag{3.157}$$

where $a_{\rm in}$ is the semi-major axis of the inner binary in the Jacobian co-ordinates. The third term describes the Keplerian orbit of the outer body m_3 around the centre of mass of the inner binary. Thus, we can define the mean motion of the outer orbit $\nu_{\rm out}$ as

$$\nu_{\rm out} \equiv \sqrt{\frac{Gm_{123}}{a_{\rm out}^3}}, \tag{3.158}$$

where $a_{\rm out}$ is the semi-major axis of the outer orbit in the Jacobian co-ordinates. The final term in equation (3.156) corresponds to the disturbing function $\mathcal{R}$ which describes the perturbation in a three-body problem:

$$\mathcal{R} = -\frac{Gm_{12}m_3}{|\boldsymbol{R}|} + \frac{Gm_1m_3}{|\boldsymbol{R} - \beta_2\boldsymbol{r}|} + \frac{Gm_2m_3}{|\boldsymbol{R} - \beta_1\boldsymbol{r}|}. \tag{3.159}$$

As a result, we find that

$$\mathcal{H} = (\text{Keplerian motion of inner orbit}) - \mathcal{R} + (\text{irrelevant to inner orbit}) \tag{3.160}$$

and

$$\mathcal{H} = (\text{Keplerian motion of outer orbit}) - \mathcal{R} + (\text{irrelevant to outer orbit}). \tag{3.161}$$

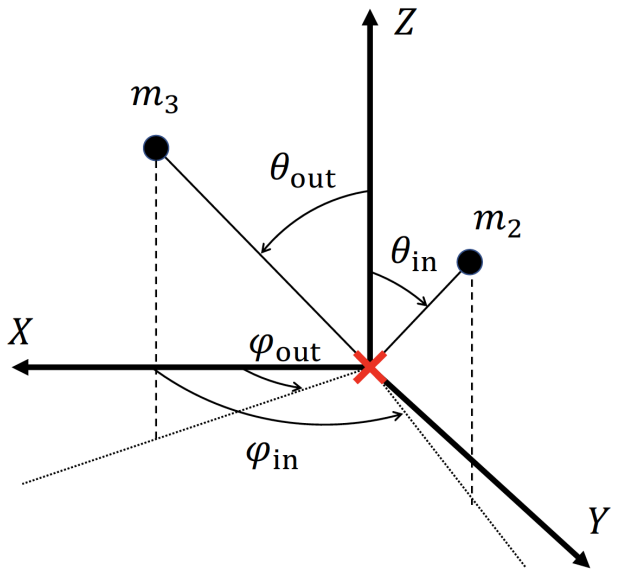

Figure 3.10: The definition of angles $\theta_{\rm in}, \varphi_{\rm in}, \theta_{\rm out}, \varphi_{\rm out}$ in spherical co-ordinates. The cross denotes the centre of mass for inner binary consisting of m_1 and m_2.

Considering the discussion in the previous section, these equations show that if we substitute $\mathcal{R}$ into the Lagrange planetary equations, we obtain the differential equations for both inner and outer orbital elements in a three-body system in the Jacobian co-ordinates.

Since the Lagrange planetary equations are differential equations for the orbital elements, it is necassary to write down the disturbing function $\mathcal{R}$ in terms of orbital elements rather than position vectors. This has been studied by many researchers (e.g. Boquet 1889; Brouwer & Clemence 1961; Brown & Shook 1933; Kaula 1962; Le Verrier 1855; Mardling 2013; Murray 1985; Newcomb 1895; Peirce 1849). We specifically follow the derivation of disturbing function for a coplanar three-body system by Mardling (2013).

Using multi-pole expansion in terms of the Legendre polynomials (e.g. Binney & Tremaine 2008), we obtain

$$\frac{1}{|\boldsymbol{R}-\beta_s\boldsymbol{r}|}=\frac{1}{R}\sum_{l=0}^{\infty}\left(\frac{\beta_1 r}{R}\right)^l P_l(\cos\psi)\ (s=1,2), \tag{3.162}$$

where $R\equiv|\boldsymbol{R}|$, $r\equiv|\boldsymbol{r}|$, P_l is the Legendre polynomial of order l, and $\cos\psi\equiv(\boldsymbol{r}\cdot\boldsymbol{R})/(rR)$. Using the addition theorem for spherical harmonics (e.g. Binney & Tremaine 2008; Jackson 1975):

$$P_l(\cos\psi)=\sum_{m=-l}^{l}\frac{4\pi}{2l+1}Y_{lm}(\theta_{\rm in},\varphi_{\rm in})Y^*_{lm}(\theta_{\rm out},\varphi_{\rm out}), \tag{3.163}$$

where Y_{lm} is the spherical harmonic of degree l and m, and Y^*_{lm} is its complex conjugate. In equation (3.163), $(\theta_{\rm in}, \varphi_{\rm in})$ and $(\theta_{\rm out}, \varphi_{\rm out})$ are sets of angles for m_2 and m_3 in spherical co-ordinates with respect to the centre of mass for inner binary consisting of m_1 and m_2, respectively (see Figure 3.10). Thus, the disturbing function $\mathcal{R}$ is expanded to

$$\mathcal{R} = G\mu_{\rm in} m_3 \sum_{l=2}^{\infty} \sum_{m=-l}^{l} \left(\frac{4\pi}{2l+1} \right) \mathcal{M}_l \left(\frac{r^l}{R^{l+1}} \right) Y_{lm}(\theta_{\rm in}, \varphi_{\rm in}) Y^*_{lm}(\theta_{\rm out}, \varphi_{\rm out}), \tag{3.164}$$

where the mass factor $\mathcal{M}_l$ is defined as

$$\mathcal{M}_l \equiv \beta_1^{l-1} - \beta_2^{l-1} = \frac{m_1^{l-1} + (-1)^l m_2^{l-1}}{m_{12}^{l-1}}. \tag{3.165}$$

For a coplanar case, we can take $\theta_{\rm in} = \theta_{\rm out} = \pi/2$, $\varphi_{\rm in} = f_{\rm in} + \varpi_{\rm in}$, and $\varphi_{\rm out} = f_{\rm out} + \varpi_{\rm out}$, where $f_{\rm in}$ and $f_{\rm out}$ are the true anomalies of inner and outer orbits, respectively, and $\varpi_{\rm in}$ and $\varpi_{\rm out}$ are the longitudes of pericentre for inner and outer orbits, respectively. Using the standard definiton of spherical harmonics:

$$Y_{lm}(\theta, \varphi) = \sqrt{\frac{2l+1}{4\pi} \frac{(l-m)!}{(l+m)!}} P_l^m(\cos\theta) \mathrm{e}^{\mathrm{i}m\varphi}, \tag{3.166}$$

where P_l^m is an associated Legendre polynomials, i is the imaginary unit, and e is the Nepier constant. We use a Roman font here to avoid confusing i and e with the inclination and eccentricity, respectively. Thus, for a coplanar case,

$$\begin{aligned} &Y_{lm}\left(\frac{\pi}{2}, f_{\rm in} + \varpi_{\rm in}\right) Y^*_{lm}\left(\frac{\pi}{2}, f_{\rm out} + \varpi_{\rm out}\right) \\ &= \frac{2l+1}{4\pi} \frac{(l-m)!}{(l+m)!} [P_l^m(0)]^2 \mathrm{e}^{\mathrm{i}m(f_{\rm in} - f_{\rm out})} \mathrm{e}^{\mathrm{i}m(\varpi_{\rm in} - \varpi_{\rm out})}. \end{aligned} \tag{3.167}$$

Since $P_l^m(x)$ is explicitly given as

$$P_l^m(x) \equiv \frac{(-1)^m}{2^l l!} (1-x^2)^{m/2} \sum_{j=\lfloor (l+m+1)/2 \rfloor}^{l} (-1)^{l-j} \left(\begin{array}{c} l \\ j \end{array} \right) \frac{(2j)!}{(2j-l-m)!} x^{2j-l-m}, \tag{3.168}$$

$$P_l^m(0) = \begin{cases} (-1)^{(l+m)/2} \dfrac{(l+m)!}{2^l l!} \left(\begin{array}{c} l \\ (l+m)/2 \end{array} \right) & (l+m \text{ even}) \\ 0 & (\text{otherwise}) \end{cases}. \tag{3.169}$$

Using the equation above, the disturbing function reduces to

$$\mathcal{R} = G\mu_{\rm in} m_3 \sum_{l=2}^{\infty} \sum_{m=-l,2}^{l} \frac{1}{2} c_{lm}^2 \mathcal{M}_l \mathrm{e}^{\mathrm{i}m(\varpi_{\rm in} - \varpi_{\rm out})} (r^l \mathrm{e}^{\mathrm{i}m f_{\rm in}}) \left(\frac{\mathrm{e}^{-\mathrm{i}m f_{\rm out}}}{R^{l+1}} \right), \tag{3.170}$$

where

$$c_{lm}^2 \equiv \frac{8\pi}{2l+1}[Y_{lm}(\pi/2,0)]^2 = \frac{(l-m)!(l+m)!}{2^{2l-1}[((l+m)/2)!((l-m)/2)!]^2} \tag{3.171}$$

and

$$\sum_{m=m_{\min},2}^{m_{\max}} \xi_m \equiv \xi_{m_{\min}} + \xi_{m_{\min}+2} + \cdots + \xi_{m_{\max}}. \tag{3.172}$$

In equation (3.172), ξ_m denotes any variables with subscript m. If a system is stable, $(r^l \mathrm{e}^{\mathrm{i}mf_{\rm in}})$ and $(\mathrm{e}^{-\mathrm{i}mf_{\rm out}}/R^{l+1})$ in equation (3.170) are nealy periodic in the inner and outer orbital periods, respectively. Therefore, we can expand them further using the Fourier expansion in terms of the mean anomalies associated with the inner and outer orbits:

$$r^l \mathrm{e}^{\mathrm{i}mf_{\rm in}} = a_{\rm in}^l \left(\frac{1-e_{\rm in}^2}{1+e_{\rm in}\cos f_{\rm in}}\right)^l \mathrm{e}^{\mathrm{i}mf_{\rm in}} = a_{\rm in}^l \sum_{n=-\infty}^{\infty} X_n^{l,m}(e_{\rm in})\mathrm{e}^{\mathrm{i}nM_{\rm in}} \tag{3.173}$$

and

$$\begin{aligned} \frac{\mathrm{e}^{-\mathrm{i}mf_{\rm out}}}{R^{l+1}} &= a_{\rm out}^{-(l+1)} \left(\frac{1-e_{\rm out}^2}{1+e_{\rm out}\cos f_{\rm out}}\right)^{-(l+1)} \mathrm{e}^{-\mathrm{i}mf_{\rm out}} \\ &= a_{\rm out}^{-(l+1)} \sum_{n'=-\infty}^{\infty} X_{n'}^{-(l+1),m}(e_{\rm out})\mathrm{e}^{-\mathrm{i}n'M_{\rm out}}, \end{aligned} \tag{3.174}$$

where $M_{\rm in}$ and $M_{\rm out}$ are the mean anomalies of the inner and outer orbits, $e_{\rm in}$ and $e_{\rm out}$ are the eccentricities of these orbits. The coefficients $X_n^{l,m}(e_{\rm in})$ and $X_n^{-(l+1),m}(e_{\rm out})$ in equations (3.173) and (3.174) are called the "Hansen coefficients" (Hughes 1981) and are expressed as

$$X_n^{l,m}(e_{\rm in}) \equiv \frac{1}{2\pi}\int_0^{2\pi} \left(\frac{r}{a_{\rm in}}\right)^l \mathrm{e}^{\mathrm{i}mf_{\rm in}}\mathrm{e}^{-\mathrm{i}nM_{\rm in}} dM_{\rm in} \tag{3.175}$$

and

$$X_{n'}^{-(l+1),m}(e_{\rm out}) \equiv \frac{1}{2\pi}\int_0^{2\pi} \left(\frac{R}{a_{\rm out}}\right)^{-(l+1)} \mathrm{e}^{-\mathrm{i}mf_{\rm out}}\mathrm{e}^{\mathrm{i}n'M_{\rm out}} dM_{\rm out}. \tag{3.176}$$

Since the real parts of the integrands in equations (3.175) and (3.176) are even functions and the imaginary parts of them are odd functions for $M_{\rm in}$ and $M_{\rm out}$, both $X_n^{l,m}(e_{\rm in})$ and $X_{n'}^{-(l+1),m}(e_{\rm out})$ are real. Thus,

$$[X_n^{l,m}(e_{\rm in})]^* = X_{-n}^{l,-m}(e_{\rm in}) = X_n^{l,m}(e_{\rm in}) \tag{3.177}$$

and

$$[X_{n'}^{-(l+1),m}(e_{\rm out})]^* = X_{-n'}^{-(l+1),-m}(e_{\rm out}) = X_{n'}^{-(l+1),m}(e_{\rm out}), \tag{3.178}$$

where the superscript $*$ denotes the complex conjugate. Substituting equations (3.173) and (3.174) into equation (3.170), and using equations (3.177) and (3.178), we obtain

$$\mathcal{R} = \frac{G\mu_{\rm in} m_3}{a_{\rm out}} \sum_{l=2}^{\infty} \sum_{m=m_{\rm min},2}^{l} \sum_{n=-\infty}^{\infty} \sum_{n'=-\infty}^{\infty} \zeta_m c_{lm}^2 \mathcal{M}_l \alpha^l X_n^{l,m}(e_{\rm in}) X_{n'}^{-(l+1),m}(e_{\rm out}) \cos\phi_{mnn'}, \tag{3.179}$$

where

$$\alpha \equiv \frac{a_{\rm in}}{a_{\rm out}}, \tag{3.180}$$

$$\zeta_m \equiv \begin{cases} 1/2, & m = 0 \\ 1, & \text{otherwise} \end{cases}, \tag{3.181}$$

$$m_{\rm min} \equiv \begin{cases} 0, & l \text{ even} \\ 1, & l \text{ odd} \end{cases}. \tag{3.182}$$

The argument $\phi_{mnn'}$ of cosine function in equation (3.179) is called the "harmonic angle" and defined as

$$\begin{aligned} \phi_{mnn'} &\equiv nM_{\rm in} - n'M_{\rm out} + m(\varpi_{\rm in} - \varpi_{\rm out}) \\ &= n\lambda_{\rm in} - n'\lambda_{\rm out} + (m-n)\varpi_{\rm in} - (m-n')\varpi_{\rm out}, \end{aligned} \tag{3.183}$$

where $\lambda_{\rm in}$ and $\lambda_{\rm out}$ are the mean longitudes of the inner and outer orbits, respectively.

In order to further calculating $\mathcal{R}$, we consider changing the order of summation for l and m in equation (3.179). This procedure can be achieved using the following relation:

$$\begin{aligned} &\sum_{l=2}^{\infty} \sum_{m=m_{\rm min},2}^{l} \xi_{lm} \\ &= [\xi_{20} + \xi_{22}] + [\xi_{31} + \xi_{33}] + [\xi_{40} + \xi_{42} + \xi_{44}] + [\xi_{51} + \xi_{53} + \xi_{55}] + \cdots \\ &= [\xi_{20} + \xi_{40} + \cdots] + [\xi_{31} + \xi_{51} + \cdots] + [\xi_{22} + \xi_{42} + \cdots] + [\xi_{33} + \xi_{53} + \cdots] + \cdots \\ &= \sum_{m=0}^{\infty} \sum_{l=l_{\rm min},2}^{\infty} \xi_{lm}, \end{aligned} \tag{3.184}$$

where

$$l_{\rm min} \equiv \begin{cases} 2, & m = 0 \\ 3, & m = 1 \\ m, & m \geq 2 \end{cases}. \tag{3.185}$$

Note that in equation (3.184) ξ_{lm} denotes any variables with two subscripts l and m.

As a result, the final expression of the disturbing function $\mathcal{R}$ is

$$\mathcal{R} = \sum_{m=0}^{\infty} \sum_{n=-\infty}^{\infty} \sum_{n'=-\infty}^{\infty} \mathcal{R}_{mnn'} \cos\phi_{mnn'}, \tag{3.186}$$

where

$$\mathcal{R}_{mnn'} \equiv \frac{G\mu_{\rm in}m_3}{a_{\rm out}} \sum_{l=l_{\rm min},2}^{\infty} \zeta_m c_{lm}^2 \mathcal{M}_l \alpha^l X_n^{l,m}(e_{\rm in}) X_{n'}^{-(l+1),m}(e_{\rm out}). \tag{3.187}$$

Equation (3.187) shows that the dependence of $\mathcal{R}$ on $e_{\rm in}$, $e_{\rm out}$ and α is completely separated. Therefore, this expression of $\mathcal{R}$ is optimal to control the order of these parameters when calculating an approximate disturbing function. Later, we use this expression to obtain the quadrupole ($l = 2$) part of the disturbing function approximately.

Chapter 4

Result

4.1 Derivation of perturbation equations

As mentioned in Chapter 1, we consdier developing the methodology to search for a binary black hole through the motion of outer body in a triple. Figure 4.1 shows a schematic illustration of a hierarchical three-body system that we consider in this thesis. An outer body of mass m_3 is orbiting around an unseen inner binary of masses m_1 and m_2, and both orbits are near-circular on a invariant plane.

Following the formulation in Chapter 3, we derive the basic perturbation equations in terms of the Jacobian co-ordinates. Major variables adopted in this chapter are summarized in Table 4.1 for clarity.

4.1.1 Basic formulation of the Lagrange planetary equations

The Hamiltonian $\mathcal{H}$ of the system illustrated in Figure 4.1 is given by

$$\begin{aligned}\mathcal{H} = &\frac{\boldsymbol{p}_{\rm CM}^2}{2m_{123}} + \left(\frac{\boldsymbol{p}^2}{2\mu_{\rm in}} - \frac{Gm_{12}\mu_{\rm in}}{|\boldsymbol{r}|}\right) + \left(\frac{\boldsymbol{P}^2}{2\mu_{\rm out}} - \frac{Gm_{123}\mu_{\rm out}}{|\boldsymbol{R}|}\right) \\ &- \left(-\frac{Gm_{12}m_3}{|\boldsymbol{R}|} + \frac{Gm_1m_3}{|\boldsymbol{R}-\beta_2\boldsymbol{r}|} + \frac{Gm_2m_3}{|\boldsymbol{R}-\beta_1\boldsymbol{r}|}\right),\end{aligned} \tag{4.1}$$

where $\boldsymbol{r}$ and $\boldsymbol{R}$ are position vectors of the inner and outer orbits, respectively, in terms of Jacobian co-ordinates, and $\boldsymbol{p}$ and $\boldsymbol{P}$ are corresponding momenta, $r = |\boldsymbol{r}|$, $R = |\boldsymbol{R}|$, $m_{12} = m_1 + m_2$, $\mu_{\rm in} = m_1m_2/m_{12}$, $\mu_{\rm out} = m_{12}m_3/m_{123}$, and $m_{123} = m_1 + m_2 + m_3$.

Thus, the disturbing function $\mathcal{R}$ in equation (4.1) is explicitly written as

$$\mathcal{R} = -\frac{Gm_{12}m_3}{R} + \frac{Gm_2m_3}{|\boldsymbol{R}-\beta_1\boldsymbol{r}|} + \frac{Gm_1m_3}{|\boldsymbol{R}-\beta_2\boldsymbol{r}|}, \tag{4.2}$$

where $\beta_1 = m_1/m_{12}$ and $\beta_2 = -m_2/m_{12}$.

Following the derivation in Mardling (2013) (see Section 3.3 for detail), this disturbing function for a coplanar case can be written explicitly as an infinite series of

symbol	meaning
$\boldsymbol{r}_i (i=1,2,3)$	position vector of $m_i (i=1,2,3)$ in arbitrary reference frame
$\boldsymbol{r} \equiv \boldsymbol{r}_2 - \boldsymbol{r}_1$	position vector of inner orbit in Jacobian co-ordinate system
$\boldsymbol{R} \equiv \boldsymbol{r}_3 - \dfrac{m_1\boldsymbol{r}_1 + m_2\boldsymbol{r}_2}{m_{12}}$	position vector of outer orbit in Jacobian co-ordinate system
$m_{12} \equiv m_1 + m_2$	total mass of inner binary
$m_{123} \equiv m_1 + m_2 + m_3$	total mass of system
$\mu_{\rm in} \equiv m_1 m_2 / m_{12}$	reduced mass of inner binary
$\mu_{\rm out} \equiv m_3 m_{12} / m_{123}$	reduced mass of three-body system
a	semi-major axis
$\alpha \equiv a_{\rm in}/a_{\rm out}$	semi-major axis ratio; after Section 4.2, $\alpha \equiv a_{\rm in}^{\rm (i)}/a_{\rm out}^{\rm (i)}$
$\beta_1 \equiv m_1/m_{12}$	
$\beta_2 \equiv -m_2/m_{12}$	
$\lambda \equiv \displaystyle\int_0^t \nu dt' + \epsilon \equiv \nu t + \tilde{\epsilon}$	mean longitude
ϖ	longitude of pericentre
$\mathcal{M}_l \equiv \dfrac{m_1^{l-1} + (-1)^l m_2^{l-1}}{m_{12}^{l-1}}$	
$\epsilon \equiv \lambda - \displaystyle\int_0^t \nu dt'$	new mean longitude at epoch
$\tilde{\epsilon} \equiv \lambda - \nu t$	mean longitude at epoch
e	eccentricity
$h \equiv e \sin\varpi$	
$k \equiv e \cos\varpi$	
$\nu_{\rm in} \equiv \sqrt{G m_{12}/a_{\rm in}^3}$	mean motion of inner binary
$\nu_{\rm out} \equiv \sqrt{G m_{123}/a_{\rm out}^3}$	mean motion of outer body

Table 4.1: Definitions of major variables in the present analysis.

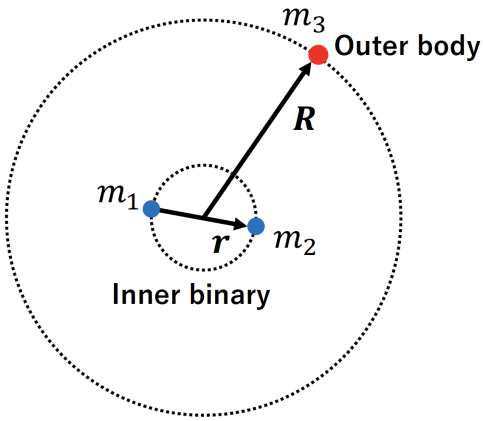

Figure 4.1: Schematic illustration of a coplanar and near-circular triple system. The relative position vectors $\boldsymbol{r}$ and $\boldsymbol{R}$ are defined in the Jacobian coordinate.

cosine functions:

$$\mathcal{R} = \sum_{m=0}^{\infty} \sum_{n=-\infty}^{\infty} \sum_{n'=-\infty}^{\infty} \mathcal{R}_{mnn'} \cos \phi_{mnn'}. \tag{4.3}$$

The coefficients of the disturbing function in the right-hand-side of equation (4.3) are further expanded as

$$\mathcal{R}_{mnn'} = \frac{G\mu_{\rm in} m_3}{a_{\rm out}} \sum_{l=l_{\rm min},2}^{\infty} \zeta_m c_{lm}^2 \mathcal{M}_l \alpha^l X_n^{l,m}(e_{\rm in}) X_{n'}^{-(l+1),m}(e_{\rm out}), \tag{4.4}$$

where the sum over l is in steps of two from $l_{\rm min}$:

$$l_{\rm min} \equiv \begin{cases} 2, m = 0 \\ 3, m = 1 \\ m, m \geq 2 \end{cases}. \tag{4.5}$$

Note that we use two indices $\{\rm in, out\}$ to indicate the inner and outer orbits, respectively.

The arguments of the cosine function in equation (4.3) are defined as

$$\phi_{mnn'} \equiv n\lambda_{\rm in} - n'\lambda_{\rm out} + (m-n)\varpi_{\rm in} - (m-n')\varpi_{\rm out}, \tag{4.6}$$

where λ is the mean longitude and ϖ is the longitude of pericentre. Also the coefficients $X_n^{l,m}(e_{\rm in})$ and $X_{n'}^{-(l+1),m}(e_{\rm out})$ in equation (4.4) are the Hansen coefficients (see

Appendix A for detail). The other coefficients in equation (4.4) are defined as

$$\alpha \equiv a_{\rm in}/a_{\rm out}, \tag{4.7}$$

$$\zeta_m \equiv \begin{cases} 1/2, m=0 \\ 1, m \neq 0 \end{cases}, \tag{4.8}$$

$$c_{lm} \equiv \sqrt{\frac{8\pi}{2l+1}} Y_{lm}(\pi/2, 0), \tag{4.9}$$

$$\mathcal{M}_l \equiv \frac{m_1^{l-1} + (-1)^l m_2^{l-1}}{m_{12}^{l-1}}. \tag{4.10}$$

The Lagrange planetary equations for orbital elements in terms of the disturbing function $\mathcal{R}$ reduce to

$$\frac{da}{dt} = \frac{2}{\mu\nu a}\frac{\partial \mathcal{R}}{\partial \lambda} \tag{4.11}$$

and

$$\frac{d\epsilon}{dt} = -\frac{2}{\mu\nu a}\left(\frac{\partial \mathcal{R}}{\partial a}\right)_{\nu,\rm fixed} + \frac{\sqrt{1-e^2}\left(1-\sqrt{1-e^2}\right)}{\mu\nu a^2 e}\frac{\partial \mathcal{R}}{\partial e}, \tag{4.12}$$

where we define ϵ and $\tilde{\epsilon}$ (see Section 3.3 for detail) through

$$\epsilon \equiv \lambda - \int_0^t \nu dt' \tag{4.13}$$

and

$$\tilde{\epsilon} \equiv \lambda - \nu t. \tag{4.14}$$

Since we now consider near-circular orbits, we use h and k instead of e and ϖ to avoid apparent divergent terms in differential equations for e and ϖ. The Lagrange planetary equations for h and k are wrriten as (e.g. Danby 1988; Moulton 1914; Murray & Dermott 2000)

$$\dot{h} = \frac{1}{\mu a^2 \nu}\sqrt{1-e^2}\frac{\partial \mathcal{R}}{\partial k} - \frac{h}{\mu a^2 \nu}\frac{\sqrt{1-e^2}}{1+\sqrt{1-e^2}}\frac{\partial \mathcal{R}}{\partial \tilde{\epsilon}} \tag{4.15}$$

and

$$\dot{k} = -\frac{1}{\mu a^2 \nu}\sqrt{1-e^2}\frac{\partial \mathcal{R}}{\partial h} - \frac{k}{\mu a^2 \nu}\frac{\sqrt{1-e^2}}{1+\sqrt{1-e^2}}\frac{\partial \mathcal{R}}{\partial \tilde{\epsilon}}, \tag{4.16}$$

where $h \equiv e\sin\varpi$ and $k \equiv e\cos\varpi$.

We have two sets of the Lagrange planetary equations both for inner and outer orbits. We emphasize here that we do not use the orbit-averaged disturbing function, unlike a conventional analysis for secular evolution, since we are interested in the short-term modulation in order to identify the signature of the inner binary.

4.1.2 Perturbation approach to the Lagrange planetary equations for coplanar near-circular orbits

Next we consider the hierarchical ($\alpha \ll 1$) and near-circular ($e_{\rm in} \ll 1$, $e_{\rm out} \ll 1$) conditions, and approximate the disturbing function, neglecting the higher-order terms than $\mathcal{O}(e^2)$ and $\mathcal{O}(\alpha^3)$. Under this approximation, the disturbing function reduces to the quadrupole moment part of the potential:

$$\begin{aligned}\mathcal{R} \approx \frac{G\mu_{\rm i} m_3 \mathcal{M}_2}{a_{\rm out}}\alpha^2 \Bigg\{ & \frac{1}{4} + \frac{3}{4}\cos(2\lambda_{\rm in} - 2\lambda_{\rm out}) + \frac{3}{4}(k_{\rm out}\cos\lambda_{\rm out} + h_{\rm out}\sin\lambda_{\rm out}) \\ & - \frac{1}{2}(k_{\rm in}\cos\lambda_{\rm in} + h_{\rm in}\sin\lambda_{\rm in}) - \frac{3}{8}[k_{\rm out}\cos(2\lambda_{\rm in} - \lambda_{\rm out}) + h_{\rm out}\sin(2\lambda_{\rm in} - \lambda_{\rm out})] \\ & - \frac{9}{4}[k_{\rm in}\cos(\lambda_{\rm in} - 2\lambda_{\rm out}) - h_{\rm in}\sin(\lambda_{\rm in} - 2\lambda_{\rm out})] \\ & + \frac{21}{8}[k_{\rm out}\cos(2\lambda_{\rm in} - 3\lambda_{\rm out}) - h_{\rm out}\sin(2\lambda_{\rm in} - 3\lambda_{\rm out})] \\ & + \frac{3}{4}[k_{\rm in}\cos(3\lambda_{\rm in} - 2\lambda_{\rm out}) + h_{\rm in}\sin(3\lambda_{\rm in} - 2\lambda_{\rm out})]\Bigg\},\end{aligned} \tag{4.17}$$

where

$$h_{\rm in} \equiv e_{\rm in}\sin\varpi_{\rm in},\ \ k_{\rm in} \equiv e_{\rm in}\cos\varpi_{\rm in} \tag{4.18}$$

and

$$h_{\rm out} \equiv e_{\rm out}\sin\varpi_{\rm out},\ \ k_{\rm out} \equiv e_{\rm out}\cos\varpi_{\rm out}. \tag{4.19}$$

Finally we insert equation (4.17) into the Lagrange planetary equations for outer orbital elements, and obtain the corresponding perturbation equations explicitly:

$$\dot{a}_{\rm out} \approx \frac{3G\mu_{\rm in} m_3 \mathcal{M}_2}{\mu_{\rm out}\nu_{\rm out} a_{\rm out}^2}\alpha^2 \sin(2\lambda_{\rm in} - 2\lambda_{\rm out}), \tag{4.20}$$

$$\dot{\epsilon}_{\rm out} \approx \frac{3G\mu_{\rm in} m_3 \mathcal{M}_2}{2\mu_{\rm out}\nu_{\rm out} a_{\rm out}^3}\alpha^2 [1 + 3\cos(2\lambda_{\rm in} - 2\lambda_{\rm out})], \tag{4.21}$$

$$\dot{h}_{\rm out} \approx \frac{G\mu_{\rm in} m_3 \mathcal{M}_2}{\mu_{\rm out}\nu_{\rm out} a_{\rm out}^3}\alpha^2 \left[\frac{3}{4}\cos\lambda_{\rm out} - \frac{3}{8}\cos(2\lambda_{\rm in} - \lambda_{\rm out}) + \frac{21}{8}\cos(2\lambda_{\rm in} - 3\lambda_{\rm out})\right], \tag{4.22}$$

$$\dot{k}_{\rm out} \approx -\frac{G\mu_{\rm in} m_3 \mathcal{M}_2}{\mu_{\rm out}\nu_{\rm out} a_{\rm out}^3}\alpha^2 \left[\frac{3}{4}\sin\lambda_{\rm out} - \frac{3}{8}\sin(2\lambda_{\rm in} - \lambda_{\rm out}) - \frac{21}{8}\sin(2\lambda_{\rm in} - 3\lambda_{\rm out})\right]. \tag{4.23}$$

4.2 Analytic solutions to the perturbation equations

4.2.1 Leading-order solutions

While it is not possible to find rigorous analytical solutions for equations (4.20)-(4.23), we can solve them iteratively. In practice, we perform the iteration just once, and write down the approximate analytical solutions:

$$\frac{a_{\rm out}}{a_{\rm out}^{\rm (i)}} \approx 1 - \frac{3G\mu_{\rm in}m_3\mathcal{M}_2}{2\mu_{\rm out}\nu_{\rm out}^{\rm (i)}[a_{\rm out}^{\rm (i)}]^3(\nu_{\rm in}^{\rm (i)}-\nu_{\rm out}^{\rm (i)})}\alpha^2 C_0[2(\nu_{\rm in}^{\rm (i)}-\nu_{\rm out}^{\rm (i)})t + 2(\epsilon_{\rm in}^{\rm (i)}-\epsilon_{\rm out}^{\rm (i)})], \tag{4.24}$$

$$\begin{aligned}\epsilon_{\rm out} \approx \epsilon_{\rm out}^{\rm (i)} &+ \frac{3\mu_{\rm in}m_3\mathcal{M}_2}{2\mu_{\rm out}(m_1+m_2+m_3)}\alpha^2\nu_{\rm out}^{\rm (i)}t \\ &+ \frac{9G\mu_{\rm in}m_3\mathcal{M}_2}{4\mu_{\rm out}\nu_{\rm out}^{\rm (i)}[a_{\rm out}^{\rm (i)}]^3(\nu_{\rm in}^{\rm (i)}-\nu_{\rm out}^{\rm (i)})}\alpha^2 S_0[2(\nu_{\rm in}^{\rm (i)}-\nu_{\rm out}^{\rm (i)})t + 2(\epsilon_{\rm in}^{\rm (i)}-\epsilon_{\rm out}^{\rm (i)})],\end{aligned} \tag{4.25}$$

$$\begin{aligned}h_{\rm out} \approx h_{\rm out}^{\rm (i)} + \frac{G\mu_{\rm in}m_3\mathcal{M}_2}{\mu_{\rm out}[a_{\rm out}^{\rm (i)}]^3\nu_{\rm out}^{\rm (i)}}\alpha^2 \Bigg[&\frac{3}{4\nu_{\rm out}^{\rm (i)}}S_0[\nu_{\rm out}^{\rm (i)}t+\epsilon_{\rm out}^{\rm (i)}] \\ &-\frac{3}{8(2\nu_{\rm in}^{\rm (i)}-\nu_{\rm out}^{\rm (i)})}S_0[(2\nu_{\rm in}^{\rm (i)}-\nu_{\rm out}^{\rm (i)})t+(2\epsilon_{\rm in}^{\rm (i)}-\epsilon_{\rm out}^{\rm (i)})] \\ &+\frac{21}{8(2\nu_{\rm in}^{\rm (i)}-3\nu_{\rm out}^{\rm (i)})}S_0[(2\nu_{\rm in}^{\rm (i)}-3\nu_{\rm out}^{\rm (i)})t+(2\epsilon_{\rm in}^{\rm (i)}-3\epsilon_{\rm out}^{\rm (i)})]\Bigg],\end{aligned} \tag{4.26}$$

$$\begin{aligned}k_{\rm out}(t) \approx k_{\rm out}^{\rm (i)} + \frac{G\mu_{\rm in}m_3\mathcal{M}_2}{\mu_{\rm out}[a_{\rm out}^{\rm (i)}]^3\nu_{\rm out}^{\rm (i)}}\alpha^2 \Bigg[&\frac{3}{4\nu_{\rm out}^{\rm (i)}}C_0[\nu_{\rm out}^{\rm (i)}t+\epsilon_{\rm out}^{\rm (i)}] \\ &-\frac{3}{8(2\nu_{\rm in}^{\rm (i)}-\nu_{\rm out}^{\rm (i)})}C_0[(2\nu_{\rm in}^{\rm (i)}-\nu_{\rm out}^{\rm (i)})t+(2\epsilon_{\rm in}^{\rm (i)}-\epsilon_{\rm out}^{\rm (i)})] \\ &-\frac{21}{8(2\nu_{\rm in}^{\rm (i)}-3\nu_{\rm out}^{\rm (i)})}C_0[(2\nu_{\rm in}^{\rm (i)}-3\nu_{\rm out}^{\rm (i)})t+(2\epsilon_{\rm in}^{\rm (i)}-3\epsilon_{\rm out}^{\rm (i)})]\Bigg],\end{aligned} \tag{4.27}$$

where

$$C_0[f(t)] \equiv \cos[f(t)] - \cos[f(t=0)], \tag{4.28}$$

$$S_0[f(t)] \equiv \sin[f(t)] - \sin[f(t=0)]. \tag{4.29}$$

Note that $\lambda_{\rm out}$ can be calculated approximately combining the solutions above:

$$\lambda_{\rm out} \equiv \int_0^t \nu_{\rm out}(t')dt' + \epsilon_{\rm out} = \int_0^t \sqrt{\frac{G(m_1+m_2+m_3)}{a_{\rm out}^3}}dt' + \epsilon_{\rm out}. \tag{4.30}$$

In the above expressions and in what follows, the superscript (i) is used to denote the values for those variables evaluated at the arbitrarily chosen initial epoch ($t=0$). Note also that α denotes $a_{\rm in}^{\rm (i)}/a_{\rm out}^{\rm (i)}$ below, instead of $a_{\rm in}(t)/a_{\rm out}(t)$ just to simplify the notation.

4.2.2 Perturbative analytic expressions for radial velocity

The next task is to derive observable quantities from the solution obtained in §4.2.1, including variations of the position and radial velocity of the outer body. We focus on the radial velocity (RV) of the outer star, assuming that the precise RV follow-up is performed to search for the unseen inner binary after the outer binary is detected. Since RV method has a great precision up to ~ 1 m/s for stars brighter than ~ 10 apparent magnitude in V band (Motalebi et al. 2015), it is feasible to detect tiny signals due to inner binary.

Because the non-zero inclination $i_{\rm orb}$ of the orbital planes relative to the observer can change the velocity amplitude by a factor of $\sin i_{\rm orb}$, we assume $\sin i_{\rm orb} = 1.0$ without loss of generality, and obtain the RV of the outer star in barycentric coordinate system:

$$V_{\rm RV}(t) = F\frac{\nu_{\rm out}(t)a_{\rm out}(t)}{\sqrt{1-e_{\rm out}(t)^2}}[e_{\rm out}(t)\cos\omega_{\rm out}(t) + \cos[f_{\rm out}(t)+\omega_{\rm out}(t)]], \tag{4.31}$$

where

$$F \equiv \frac{\mu_{\rm out}}{m_3} = \frac{m_1+m_2}{m_1+m_2+m_3}. \tag{4.32}$$

Note that the RV is just $V_{\rm RV}\sin i_{\rm orb}$ for the case that $\sin i_{\rm orb} \neq 1.0$. Neglecting terms higher than $\mathcal{O}(e^2)$, we obtain

$$\begin{aligned} V_{\rm RV}(t) \approx F\big\{&\nu_{\rm out}(t)a_{\rm out}(t)\cos[\lambda_{\rm out}(t)] \\ &+ \nu_{\rm out}(t)a_{\rm out}(t)k_{\rm out}(t)\cos[2\lambda_{\rm out}(t)] \\ &+ \nu_{\rm out}(t)a_{\rm out}(t)h_{\rm out}(t)\sin[2\lambda_{\rm out}(t)]\big\}. \end{aligned} \tag{4.33}$$

Combining with the results in §4.2.1, neglecting $\mathcal{O}(\alpha^5)$ and $\mathcal{O}(e\alpha^2)$, equation (4.33) is approximated by the sum of 9 terms:

$$V_{\rm RV} \approx \sum_{i=1}^{9} V_i. \tag{4.34}$$

We define the following quantities depending on the frequency:

$$V_{\rm Kep} \equiv V_1 + V_3 + V_7 \approx V_1, \tag{4.35}$$

$$V_{\rm ecc} \equiv V_2 + V_4 \approx V_2, \tag{4.36}$$

and

$$V_{\rm binary} \equiv V_5 + V_6 + V_8 + V_9. \tag{4.37}$$

The explicit expressions for the frequencies and amplitudes of the 9 terms, and the definition of $V_{\rm Kep}$, $V_{\rm ecc}$ and $V_{\rm binary}$ are listed in Table 4.2, where we use the following

variables:

$$V_{\mathrm{RV},0} \equiv F\nu_{\mathrm{out}}^{(\mathrm{i})}a_{\mathrm{out}}^{(\mathrm{i})}, \tag{4.38}$$

$$p(t) \approx \frac{9}{4}\left(\sqrt{\frac{m_1}{m_2}}+\sqrt{\frac{m_2}{m_1}}\right)^{-2} F^{-\frac{1}{2}}\alpha^{\frac{7}{2}}S_0[2(\nu_{\mathrm{in}}^{(\mathrm{i})}-\nu_{\mathrm{out}}^{(\mathrm{i})})t+2(\epsilon_{\mathrm{in}}^{(\mathrm{i})}-\epsilon_{\mathrm{out}}^{(\mathrm{i})})], \tag{4.39}$$

$$\frac{\Delta\nu_{\mathrm{out}}}{\nu_{\mathrm{out}}^{(\mathrm{i})}} \approx \frac{3}{2}\left(\sqrt{\frac{m_1}{m_2}}+\sqrt{\frac{m_2}{m_1}}\right)^{-2} \alpha^2\left[1-\frac{3}{2}F^{-\frac{1}{2}}\alpha^{\frac{3}{2}}\cos[2(\epsilon_{\mathrm{in}}^{(\mathrm{i})}-\epsilon_{\mathrm{out}}^{(\mathrm{i})})]\right], \tag{4.40}$$

and

$$K \equiv V_{\mathrm{RV},0}\left(\sqrt{\frac{m_1}{m_2}}+\sqrt{\frac{m_2}{m_1}}\right)^{-2} F^{-\frac{1}{2}}\alpha^{\frac{7}{2}}. \tag{4.41}$$

Note that in what follows we use K as equation (4.41) rather than the radial velocity semi-amplitude.

The three terms V_1, V_3 and V_7 constituting V_{Kep} basically correspond to the Kepler motion of the outer body but with their frequencies modified only slightly from $\omega = \nu_{\mathrm{out}}^{(\mathrm{i})}$ due to the presence of the inner binary. Since the frequency difference $\Delta\nu_{\mathrm{out}}$ is very small, the three terms would be degenerate.

The two terms V_2 and V_4 in V_{ecc} around $\omega = 2\nu_{\mathrm{out}}^{(\mathrm{i})}$ come from the second and third terms in equation (4.33), representing the first order expansion of the true anomaly f in terms of e and λ. Since they show up always for non-circular orbits, they are not directly related to the presence of the inner binary.

The remaining four terms V_5, V_6, V_8 and V_9 in V_{binary} around $\omega = 2\nu_{\mathrm{in}}^{(\mathrm{i})}$ represent the velocity modulation due to the quadrupole moment of the inner binary, and thus they are the source for the nature of the inner binary. Therefore, we use the word "signals" referring to V_{binary}. Indeed the detection of those signals reveals $\nu_{\mathrm{in}}^{(\mathrm{i})}$ and K. Since the parameters characterizing the outer orbit, $V_{\mathrm{RV},0}$, a_{out} and m_3 should be known from V_{Kep}, we can estimate m_1, m_2 and a_{in} separately from V_{binary}, or constrain those parameters even from the upper limits on V_{binary}.

While V_{binary} is obtained precisely from the perturbation expansion, they can be derived more qualitatively as follows. Consider a simplified model illustrated in Figure 4.2. If we neglect the motion of the outer body m_3 during one orbital period of the inner binary with $P_{\mathrm{in}} \ll P_{\mathrm{out}}$, the force acting on m_3 is given by

$$\mathcal{F} = \frac{Gm_2m_3}{\left(a_{\mathrm{out}}-\frac{m_1}{m_1+m_2}a_{\mathrm{in}}\right)^2}+\frac{Gm_1m_3}{\left(a_{\mathrm{out}}+\frac{m_2}{m_1+m_2}a_{\mathrm{in}}\right)^2}. \tag{4.42}$$

Neglecting $\mathcal{O}(\alpha^3)$, equation (4.42) reduces to

$$\mathcal{F} \approx \frac{G(m_1+m_2)m_3}{a_{\mathrm{out}}^2}+\frac{3Gm_1m_2m_3}{(m_1+m_2)a_{\mathrm{out}}^2}\alpha^2. \tag{4.43}$$

The first term in the right-hand-side causes the Keplerian motion of m_3, and the second term corresponds to the modulation due to the inner binary. Since the second

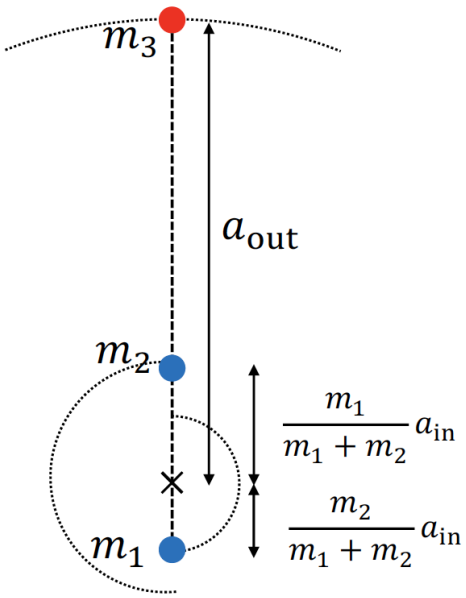

Figure 4.2: A simplified model to derive $V_{\rm binary}$ qualitatively. The cross denotes the center of mass for the inner binary.

term is symmetric with respect to m_1 and m_2, it induces the modulation of a period of $P_{\rm in}/2$. Therefore, the amplitude of the velocity modulation δV and the frequency ω are roughly estimated as

$$\delta V \approx \frac{1}{m_3}\left[\mathcal{F} - \frac{G(m_1+m_2)m_3}{a_{\rm out}^2}\right]\frac{P_{\rm in}}{2} \approx 3\pi V_{\rm RV,0} F^{-\frac{1}{2}}\left(\sqrt{\frac{m_1}{m_2}}+\sqrt{\frac{m_2}{m_1}}\right)^{-2}\alpha^{\frac{7}{2}}, \quad (4.44)$$

$$\omega \approx \frac{2\pi}{P_{\rm in}/2} = 2\nu_{\rm in}. \quad (4.45)$$

These expressions qualitatively reproduce $V_{\rm binary}$.

symbol	frequency ω	expression
V_1	$\nu_{\rm out}^{\rm (i)} + \Delta\nu_{\rm out}$	$V_{\rm RV,0}\cos(\omega t + p(t) + \epsilon_{\rm out}^{\rm (i)})$
V_2	$2(\nu_{\rm out}^{\rm (i)} + \Delta\nu_{\rm out})$	$h_{\rm out}^{\rm (i)} V_{\rm RV,0}\sin(\omega t + 2p(t) + 2\epsilon_{\rm out}^{\rm (i)}) + k_{\rm out}^{\rm (i)} V_{\rm RV,0}\cos(\omega t + 2p(t) + 2\epsilon_{\rm out}^{\rm (i)}) - \frac{3}{4}V_{\rm RV,0}\left(\sqrt{\frac{m_1}{m_2}} + \sqrt{\frac{m_2}{m_1}}\right)^{-2}\alpha^2\cos(\omega t + 2p(t) + \epsilon_{\rm out}^{\rm (i)})$
V_3	$\nu_{\rm out}^{\rm (i)} + 2\Delta\nu_{\rm out}$	$\frac{3}{4}V_{\rm RV,0}\left(\sqrt{\frac{m_1}{m_2}} + \sqrt{\frac{m_2}{m_1}}\right)^{-2}\alpha^2\cos(\omega t + 2p(t) + \epsilon_{\rm out}^{\rm (i)})$
V_4	$2(\nu_{\rm out}^{\rm (i)} + \Delta\nu_{\rm out})$	$\frac{3}{16}K\left[7\cos(\omega t + 2p(t) + 2\epsilon_{\rm in}^{\rm (i)} - \epsilon_{\rm out}^{\rm (i)}) + \cos(\omega t + 2p(t) - 2\epsilon_{\rm in}^{\rm (i)} + 3\epsilon_{\rm out}^{\rm (i)})\right]$
V_5	$2\nu_{\rm in}^{\rm (i)} - \nu_{\rm out}^{\rm (i)} + 2\Delta\nu_{\rm out}$	$-\frac{21}{16}K\cos(\omega t + 2p(t) + 2\epsilon_{\rm in}^{\rm (i)} - \epsilon_{\rm out}^{\rm (i)})$
V_6	$2\nu_{\rm in}^{\rm (i)} - \nu_{\rm out}^{\rm (i)} + \Delta\nu_{\rm out}$	$\frac{3}{8}K\cos(\omega t + p(t) + 2\epsilon_{\rm in}^{\rm (i)} - \epsilon_{\rm out}^{\rm (i)})$
V_7	$\nu_{\rm out}^{\rm (i)} + \Delta\nu_{\rm out}$	$-\frac{3}{8}K\left[\cos(\omega t + p(t) + 2\epsilon_{\rm in}^{\rm (i)} - \epsilon_{\rm out}^{\rm (i)}) + \cos(\omega t + p(t) - 2\epsilon_{\rm in}^{\rm (i)} + 3\epsilon_{\rm out}^{\rm (i)})\right]$
V_8	$2\nu_{\rm in}^{\rm (i)} - 3\nu_{\rm out}^{\rm (i)} - \Delta\nu_{\rm out}$	$\frac{3}{8}K\cos(\omega t - p(t) + 2\epsilon_{\rm in}^{\rm (i)} - 3\epsilon_{\rm out}^{\rm (i)})$
V_9	$2\nu_{\rm in}^{\rm (i)} - 3\nu_{\rm out}^{\rm (i)} - 2\Delta\nu_{\rm out}$	$-\frac{3}{16}K\cos(\omega t - 2p(t) + 2\epsilon_{\rm in}^{\rm (i)} - 3\epsilon_{\rm out}^{\rm (i)})$
$V_{\rm Kep}$	$\approx \nu_{\rm out}^{\rm (i)}$	$V_1 + V_3 + V_7 \approx V_1$
$V_{\rm ecc}$	$\approx 2\nu_{\rm out}^{\rm (i)}$	$V_2 + V_4 \approx V_2$
$V_{\rm binary}$	$\approx 2\nu_{\rm in}^{\rm (i)}$	$V_5 + V_6 + V_8 + V_9$
K	$\cdots$	$V_{\rm RV,0}\left(\sqrt{\frac{m_1}{m_2}} + \sqrt{\frac{m_2}{m_1}}\right)^{-2}\left(\frac{m_1+m_2}{m_1+m_2+m_3}\right)^{-\frac{1}{2}}\alpha^{\frac{7}{2}}$

Table 4.2: Nine terms for the radial velocity of the outer body from perturbative analytic solutions. We define $V_{\rm Kep}$, $V_{\rm ecc}$, and $V_{\rm binary}$ according to the frequency $\omega \approx \nu_{\rm out}^{\rm (i)}$, $2\nu_{\rm out}^{\rm (i)}$, and $2\nu_{\rm in}^{\rm (i)}$, respectively.

symbol	value
$a_{\rm out}$	2.0 au
$a_{\rm in}$	0.1 au
m_1	10.0 $M_\odot$
m_2	10.0 $M_\odot$
m_3	0.5 $M_\odot$
$e_{\rm in}$	10^{-8}
$e_{\rm out}$	10^{-5}
$f_{\rm in}$	$\pi/6$
$f_{\rm out}$	$2\pi/3$
$\varpi_{\rm in}$	0.0
$\varpi_{\rm out}$	0.0

Table 4.3: Initial condition for numerical simulation described in Section 4.3

4.3 Comparison of the perturbation solution with numerical simulation

Before applying our pertubative formulae to the binary system 2M05215658+4359220, we check their validity and limitation by comparing equations (4.24)-(4.27) and the radial velocity against the result of numerical simulation based on a public N-body package *rebound*. This section focuses on a system with $\alpha \ll 1$ and $m_3 \ll m_1 + m_2$ whose parameters are summarized in Table 4.3, and the validity in the case of the binary 2M05215658+4359220 will be considered in Section 5.

Consider first the orbital elements. Figure 4.3 (a) - (c) show the comparison for $a_{\rm out}/a_{\rm out}^{\rm (i)} - 1$, $\cos\lambda_{\rm out}$, $h_{\rm out} - h_{\rm out}^{\rm (i)}$ and $k_{\rm out} - k_{\rm out}^{\rm (i)}$, respectively. As mentioned in the previous section, since the short-term oscillations reflected in $V_{\rm binary}$ are the direct evidence of the inner binary, we also check the corresponding short-period terms $h_{\rm out,short}$ and $k_{\rm out,short}$ in $h_{\rm out}$ and $k_{\rm out}$:

$$h_{\rm out,short} \equiv \frac{G\mu_{\rm in} m_3 \mathcal{M}_2}{\mu_{\rm out}[a_{\rm out}^{\rm (i)}]^3 \nu_{\rm out}^{\rm (i)}} \alpha^2 \left[-\frac{3}{8(2\nu_{\rm in}^{\rm (i)} - \nu_{\rm out}^{\rm (i)})} S_0[(2\nu_{\rm in}^{\rm (i)} - \nu_{\rm out}^{\rm (i)})t + (2\epsilon_{\rm in}^{\rm (i)} - \epsilon_{\rm out}^{\rm (i)})] \right.$$
$$\left. + \frac{21}{8(2\nu_{\rm in}^{\rm (i)} - 3\nu_{\rm out}^{\rm (i)})} S_0[(2\nu_{\rm in}^{\rm (i)} - 3\nu_{\rm out}^{\rm (i)})t + (2\epsilon_{\rm in}^{\rm (i)} - 3\epsilon_{\rm out}^{\rm (i)})] \right] \tag{4.46}$$

and

$$k_{\rm out,short} \equiv \frac{G\mu_{\rm in}m_3\mathcal{M}_2}{\mu_{\rm out}[a_{\rm out}^{\rm (i)}]^3\nu_{\rm out}^{\rm (i)}}\alpha^2\left[-\frac{3}{8(2\nu_{\rm in}^{\rm (i)}-\nu_{\rm out}^{\rm (i)})}C_0[(2\nu_{\rm in}^{\rm (i)}-\nu_{\rm out}^{\rm (i)})t+(2\epsilon_{\rm in}^{\rm (i)}-\epsilon_{\rm out}^{\rm (i)})]\right.$$
$$\left.-\frac{21}{8(2\nu_{\rm in}^{\rm (i)}-3\nu_{\rm out}^{\rm (i)})}C_0[(2\nu_{\rm in}^{\rm (i)}-3\nu_{\rm out}^{\rm (i)})t+(2\epsilon_{\rm in}^{\rm (i)}-3\epsilon_{\rm out}^{\rm (i)})]\right]. \tag{4.47}$$

The results are shown in Figures 4.4 and 4.5.

In what follows, we use the subscripts app and sim to denote the quantities from approximation formulae and numerical simulation, respectively. The upper panel of Figure 4.3 (a) shows that the fractional modulation amplitude of $a_{\rm out}$ relative to $a_{\rm out}^{\rm (i)}-1$ is $O(10^{-5})$. The difference between our analytic solution and the numerical result plotted in the lower panel is about 5 percent of the modulation. The periodic signal at the frequency $\nu_{\rm in}$ of the inner binary is also gradually modulated with the frequency $\nu_{\rm out}$.

Figure 4.3 (b) and (c) indicate that $\cos\lambda_{\rm out}$, $h_{\rm out}$ and $k_{\rm out}$ exhibit the very similar behavior, while their fractional residual amplitudes are significantly smaller than that of $a_{\rm out}$.

Figure 4.4 and 4.5 show the comparison for short-term oscillations $h_{\rm out,short}$ and $k_{\rm out,short}$, indicating that the fractional deviation of those amplitudes is about 3% at $t \approx P_{\rm out}$ although $h_{\rm out}$ and $k_{\rm out}$ deviates gradually due to the long-term modulation.

Consider next the comparison of the RV. Figure 4.6 compares $V_{\rm 1,app}$ (see Table 4.2) with $V_{\rm RV,sim}$. As we can see in Figure 4.6, while the major component of the RV can be explained by V_1, the residual shows the presence of the other modes, *i.e.* V_2 to V_9 in Table 4.2. Among the modes in the residual, the short-term oscillations corresponding to $V_{\rm binary}$ include the information of the inner binary.

Figure 4.7 compares $V_{\rm binary,app}$ (see Table 4.2) with $V_{\rm RV,sim}-(V_{\rm 1,app}+V_{\rm 2,app}+V_{\rm 3,app}+V_{\rm 4,app}+V_{\rm 7,app})$. The spikes in Figure 4.7 correspond to the short-term spikes in the residual of Figure 4.6. The $V_{\rm binary}$ from approximation shows significant deviation after about $0.4P_{\rm out}$, however, the amplitude of each spike only deviates about 4% at $t \approx P_{\rm out}$. Figure 4.8 shows the same plot as Figure 4.7 for longer time. It shows that the approximation formula is no longer accurate after a long time from the initial epoch due to the long-term modulation. However, the amplitude of each spike only deviates about 8% at $t \approx 3.5P_{\rm out}$.

Figures 4.3 to 4.10 confirm that our approximation formulae are sufficiently accurate as long as both α and eccentricities are small enough. Even though the longer-term modulation starts to dominate the entire amplitude of the signals, the higher-frequency component of the RV that carries the information of the inner binary can be reproduced by our analytic solution within a few percent; see Figure 4.7 and 4.8.

In order to prove that the lower-frequency modulation does not affect the accuracy of the RV components around at frequency $2\nu_{\rm in}$, we plot Figure 4.9 and 4.10 that are renormalized adopting the values of all variables at $t = 3P_{\rm out}$ as their initial values. They show that the higher-frequency components in our analytic solutions remain

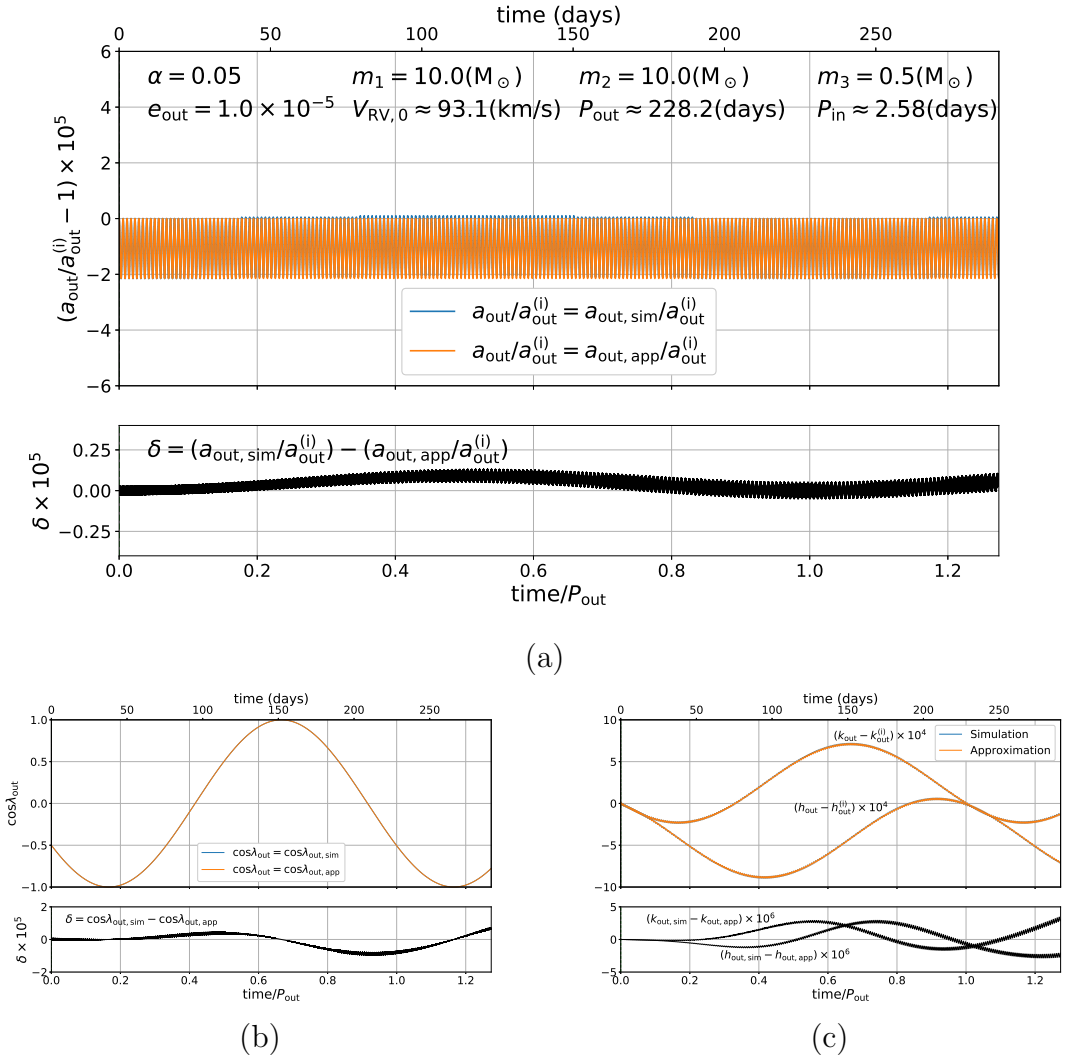

Figure 4.3: Comparison of our approximate formulae against numerical simulation for the initial condition summarized in Table 4.3: (a) $a_{\mathrm{out}}/a_{\mathrm{out}}^{(\mathrm{i})} - 1$, (b) $\cos\lambda_{\mathrm{out}}$, and (c) $h_{\mathrm{out}} - h_{\mathrm{out}}^{(\mathrm{i})}$ and $k_{\mathrm{out}} - k_{\mathrm{out}}^{(\mathrm{i})}$

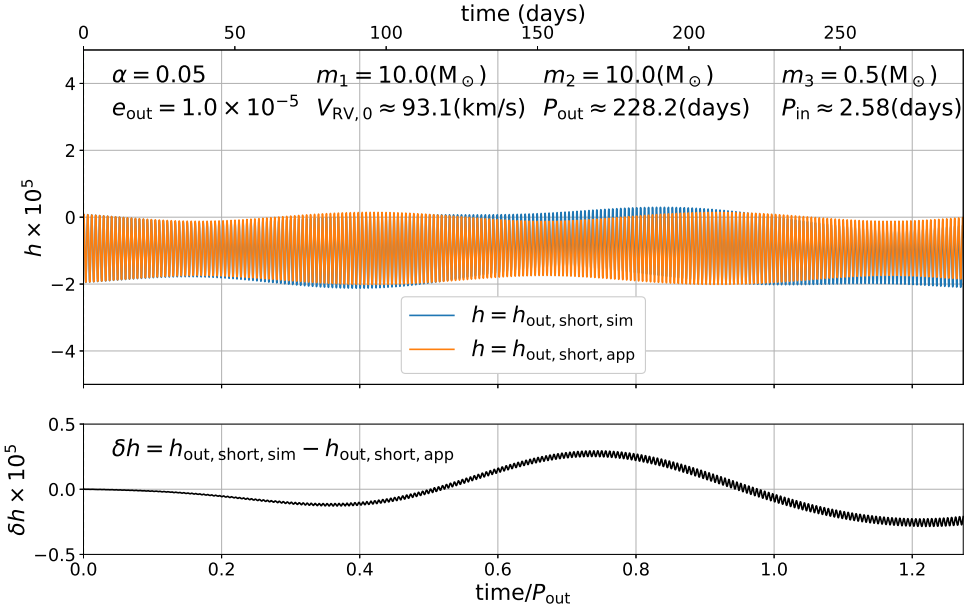

Figure 4.4: Comparison of $h_{\mathrm{out,short,sim}} \equiv h_{\mathrm{out,sim}} - (h_{\mathrm{out,app}} - h_{\mathrm{out,short,app}})$ and $h_{\mathrm{out,short,app}}$ (see equation (4.46)) for the initial condition listed in Table 4.3

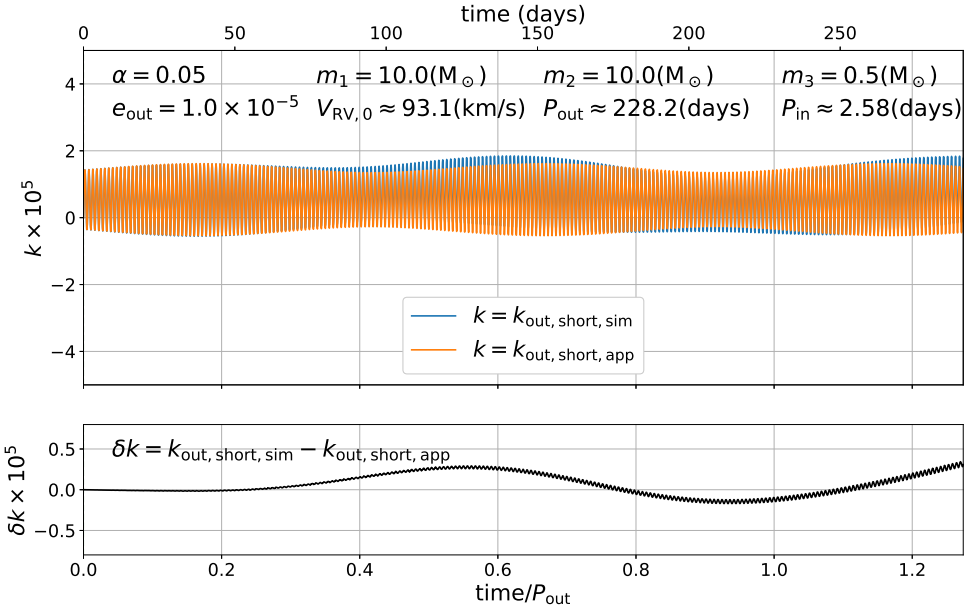

Figure 4.5: Comparison of $k_{\mathrm{out,short,sim}} \equiv k_{\mathrm{out,sim}} - (k_{\mathrm{out,app}} - k_{\mathrm{out,short,app}})$ and $k_{\mathrm{out,short,app}}$ (see equation (4.47)) for the initial condition listed in Table 4.3

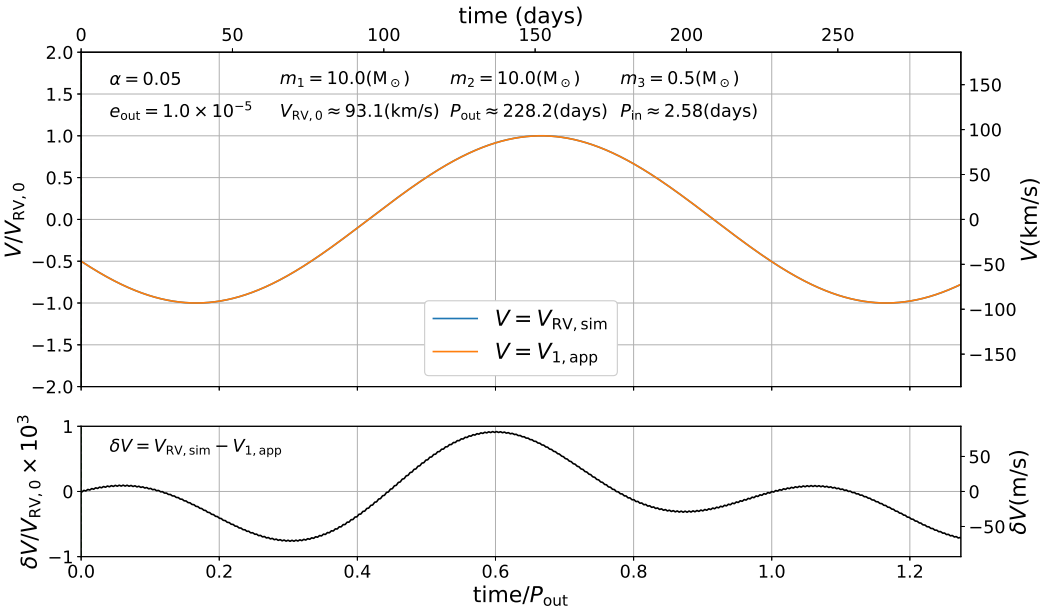

Figure 4.6: Comparison of $V_{\mathrm{RV,sim}}$ and $V_{1,\mathrm{app}}$ (Table 4.2) for the initial condition summarized in Table 4.3

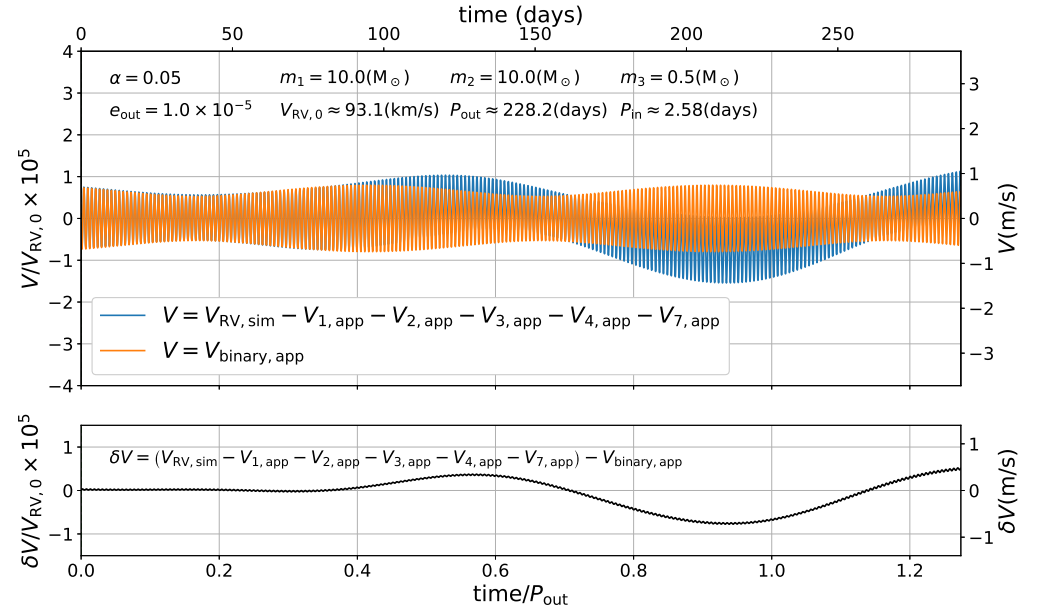

Figure 4.7: Same as Figure 4.6 but for $V_{\mathrm{RV,sim}} - (V_{1,\mathrm{app}} + V_{2,\mathrm{app}} + V_{3,\mathrm{app}} + V_{4,\mathrm{app}} + V_{7,\mathrm{app}})$ and $V_{\mathrm{binary,app}}$ (see Table 4.2)

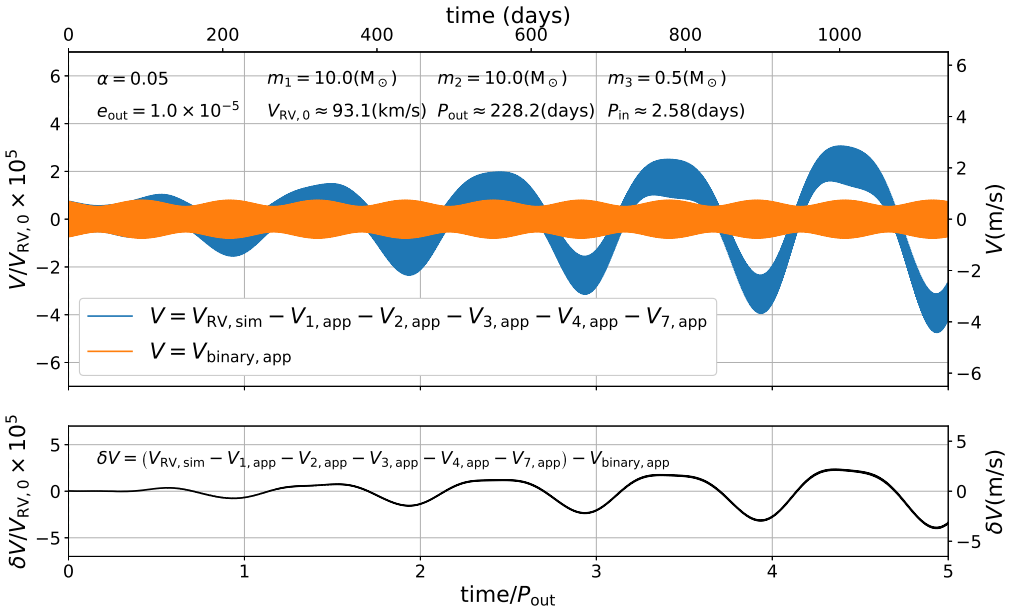

Figure 4.8: Same as Figure 4.7 but for $0 \leq t \leq 5P_{\mathrm{out}}$

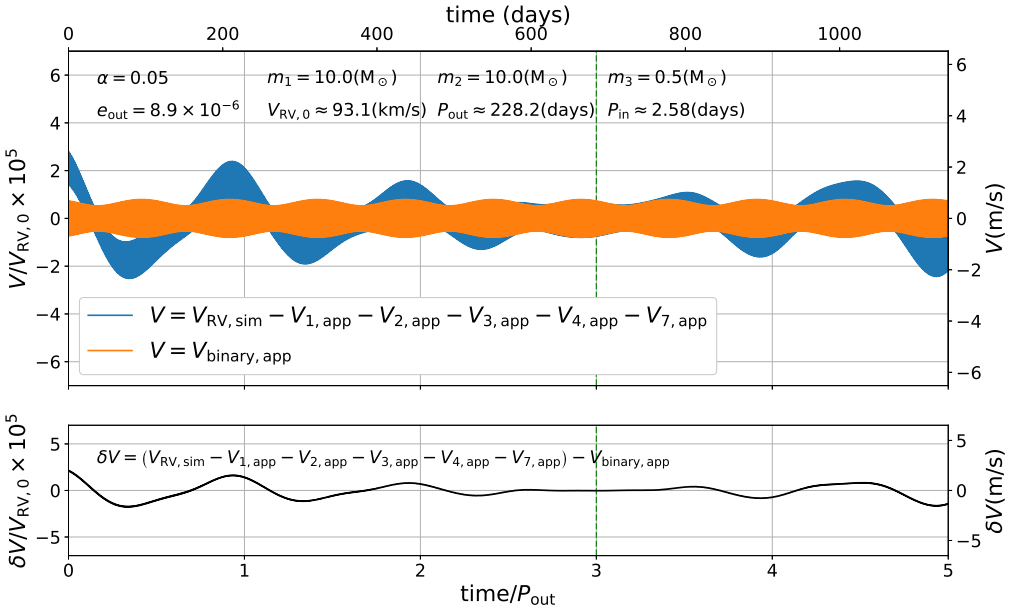

Figure 4.9: Same as Figure 4.8 but we adopt the analytic formulae using the orbital parameters at $t = 3P_{\mathrm{out}}$ for their initial values.

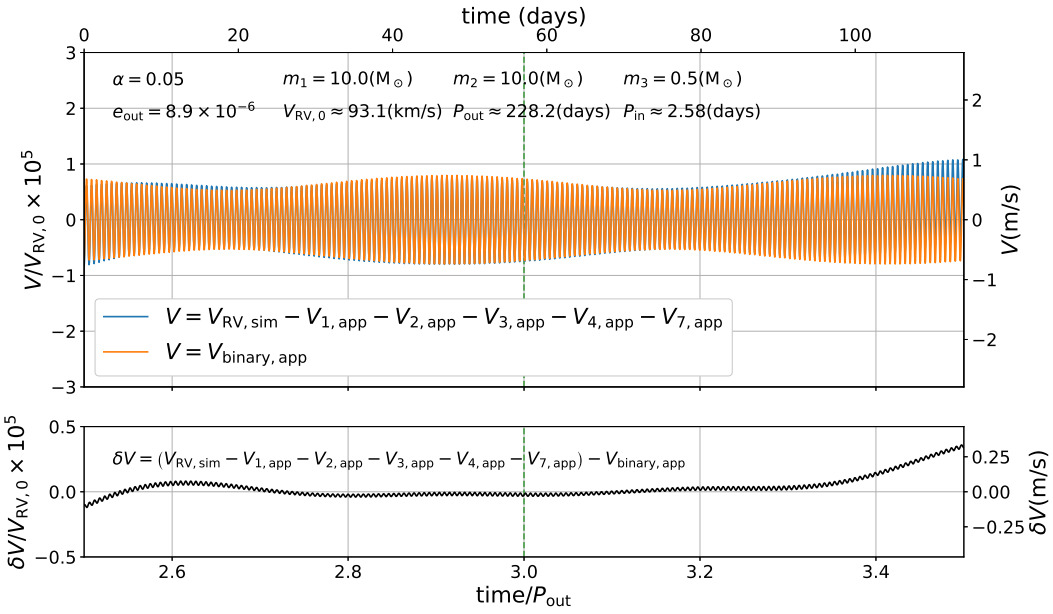

Figure 4.10: An enlarged version of Figure 4.9 for $2.5P_{\mathrm{out}} \leq t \leq 3.5P_{\mathrm{out}}$

accurate at least for a few orbital periods of the inner binary if they are reset at any arbitrary epoch.

Chapter 5

Application to a binary system 2M05215658+4359220

Thompson et al. (2018) reported the discovery of a binary system 2M05215658+4359220 that consists of a red giant and an unseen massive object. They first searched for systems exhibiting anomalously large radial accelerations from the Apache Point Observatory Galactic Evolution Experiment (APOGEE) radial velocity data, and selected 200 candidates of binaries. After checking the photometric variations from the All-Sky Automated Survey for Supernovae (ASAS-SN) data, they identified 2M05215658+4359220 as the most likely binary candidate. Then they performed the radial velocity follow-up observation with the Tillinghast Reflector Echelle Spectrograph (TRES) on the 1.5 m telescope at the Fred Lawrence Whipple Observatory (FLWO). They obtained 11 spectra with the precision of about 0.1 kms^{-1} over six months. Since the orbital period of the system is very close to that of the photometric variations, they assumed that it is tidally synchronized, therefore the inclination of rotation axis of red giant i_{rot} is equal to the orbital inclination i_{orb}: $i \equiv i_{\mathrm{rot}} = i_{\mathrm{orb}}$. Then, they estimated the best-fit parameters of the system (Table 5.1) from the RV data and the spectroscopic analysis of the red giant.

Thompson et al. (2018) estimated the mass of the unseen companion to be $m_{\mathrm{giant}} =$

parameter	value	meaning
P_{out}	83.205 ± 0.064 days	orbital period
m_{co}	$3.2^{+1.1}_{-0.4}$ $\mathrm{M}_{\odot}$	mass of an unseen companion
m_{giant}	$3.0^{+0.6}_{-0.5}$ $\mathrm{M}_{\odot}$	mass of a red giant
e_{out}	0.0048 ± 0.0026	eccentricity
ϖ_{out}	197.13 ± 32.07 deg	longitude of pericentre
$\sin i$	$0.97^{+0.02}_{-0.14}$	inclination of the orbital plane

Table 5.1: A list of parameters for the binary system 2M05215658+4359220 (Thompson et al. 2018)

$3.0^{+0.6}_{-0.5}$ $M_\odot$. Since the mass is close to the maximum mass of the neutron star, it could be a single black hole as well, or even a binary neutron star. Thus we apply our perturbative result derived in the present analysis to constrain the parameters for the possible inner binary by setting $m_{\rm giant} = m_3$ and $m_{\rm CO} = m_1 + m_2$. Furthermore we assume that the inner binary is near-circular and coplanar with the outer orbit.

Under those assumptions, we can constrain the period $P_{\rm in}$ and mass ratio m_2/m_1 of the possible inner binary in the 2M05215658+4359220 system. Although K is not the amplitude of $V_{\rm binary}$ itself rigorously, we use K to put a constraint since K well characterizes the amplitude of $V_{\rm binary}$ (see Table 4.2). This is justified using numerical simulation later. Figure 5.1 shows a contour plot of K computed from equation (4.41) adopting the parameters in Table 5.1. The color is coded according to the magnitude of K, and the plotted contour curves are labelled with K in units of m/s. Note that the RV normally has a $\sin i$ factor if the orbit inclined toward our line of sight, therefore the signal should be $V_{\rm binary} \sin i_{\rm orb}$ rigorously although it may not affect much for the case we consider here (see Table 5.1). The right vertical axis shows the semi-major axis ratio α corresponding to $P_{\rm in}$ in the left vertical axis.

We also indicate a dynamically unstable region in gray, following a wildly used criterion by Mardling & Aarseth (2001):

$$\left(\frac{a_{\rm in}}{a_{\rm out}}\right)_{\rm crit} = \frac{1-e_{\rm out}}{2.8}\left(\frac{(1+m_3/(m_1+m_2))(1+e_{\rm out})}{\sqrt{1-e_{\rm out}}}\right)^{-\frac{2}{5}} \approx 0.272. \tag{5.1}$$

Even with the current RV follow-up of the system, the data are consistent with a simple Keplerian orbit of the red giant within the observational precision of ~ 0.1 km/s (Thompson et al. 2018). In turn, even the current data exclude the region beyond $V_{\rm binary} = 100/\sin i_{\rm orb} \approx 100$ in Figure 5.1. It is very likely that the precision of the RV measurement over several weeks is significantly better with high-resolution spectrographs. Thus it would be relatively easy to improve the constraint, or future RV data might even detect a signature of the presence of the unseen inner binary.

The accuracy of the perturbation formulae, however, is not guaranteed when α becomes large. Thus we attempt to check the validity of the constraints using numerical simulations. Specifically, we consider three cases, black circles labelled A, B, and C in Figure 5.1, whose parameters are summarized in Tables 5.2 and 5.3. Cases A, B and C have the same mass ratio $m_2/m_1 (= 0.4)$, but different orbital periods of the inner binary $P_{\rm in}$. Since α monotonically increases with $P_{\rm in}$, the accuracy of the approximate formula should degrade for larger $P_{\rm in}$.

Figure 5.2 (a) - (c) compare the RV signals computed with the perturbation formulae and numerical simulations for Case A to Case C. While these figures show that the entire RV signals are affected by the longer-term modulation with a period of $P_{\rm out}$, the RV component corresponding to the inner binary period is generally *underestimated* by a factor of few relative to the numerical result. Furthermore, $V_{\rm binary}$ is very similar to K itself, implying that the different phases among V_5, V_6, V_8, and V_9 do not cancel the overall amplitude of $V_{\rm binary}$. Therefore, the constraints plotted in Figure 5.1 should be indeed regarded as conservative, and serve as a useful analytical limit on a possible inner binary.

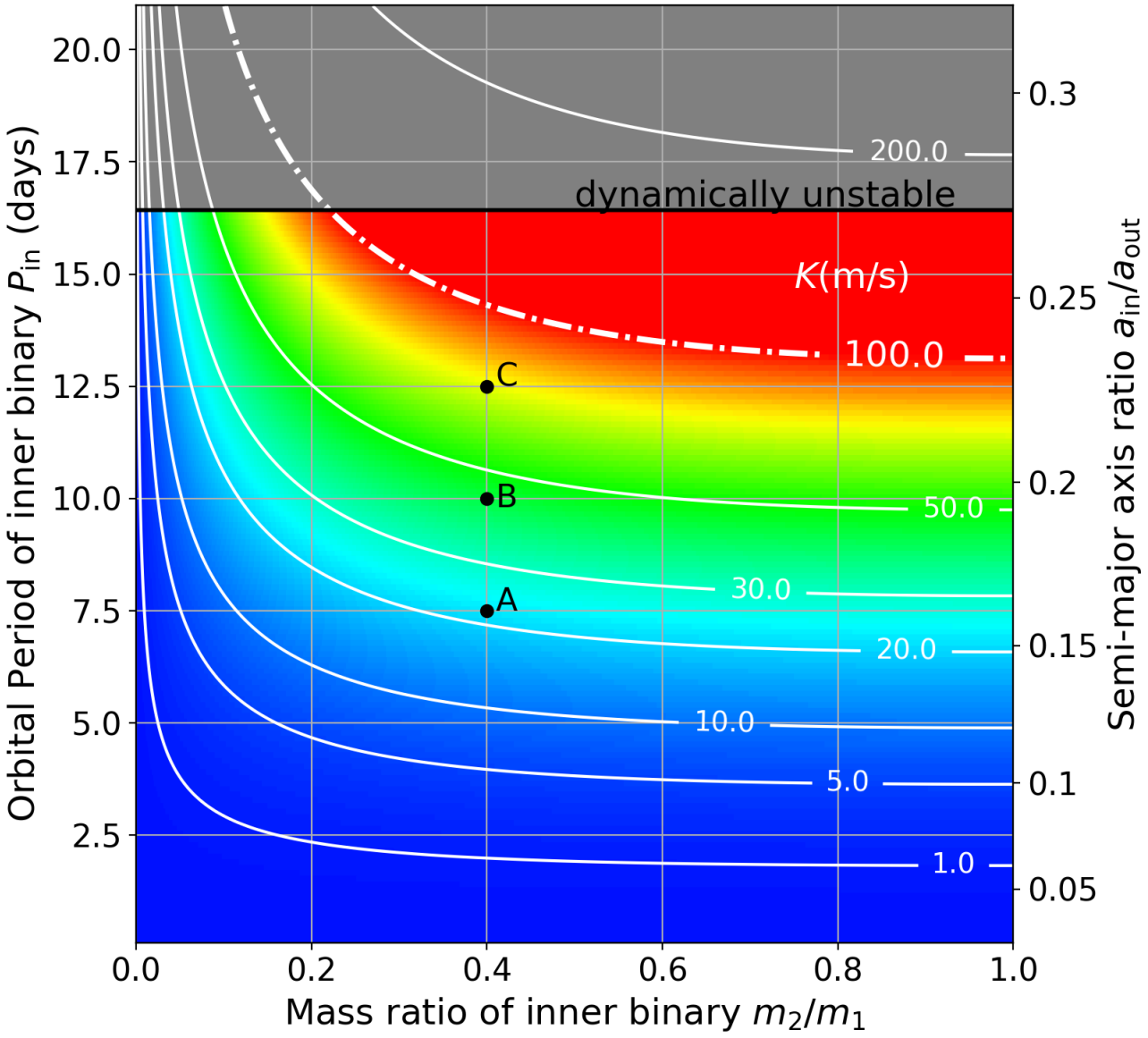

Figure 5.1: The estimated RV modulations K due to the inner binary for 2M05215658+4359220 (Eq. (4.41)). Each contour curve is labelled by the value of K in units of m/s. The gray region specifies the dynamically unstable region calculated by equation (5.1).

parameter	value
$a_{\rm out}$	0.685 au
m_3	3.0 $M_\odot$
$e_{\rm in}$	10^{-8}
$e_{\rm out}$	0.0048
$f_{\rm in}$	$\frac{\pi}{6}$
$f_{\rm out}$	$\frac{2}{3}\pi$
$\varpi_{\rm in}$	0.0
$\varpi_{\rm out}$	$\frac{197.13}{180}\pi$

Table 5.2: Initial parameters common for Cases A to C

parameter	value	Case
$a_{\rm in}$	0.11 au	A
$P_{\rm in}$	7.5 days	A
m_2/m_1	0.4	A
(m_1, m_2) $M_\odot$	$(2.29, 0.91)$	A
$a_{\rm in}$	0.13 au	B
$P_{\rm in}$	10.0 days	B
m_2/m_1	0.4	B
(m_1, m_2) $M_\odot$	$(2.29, 0.91)$	B
$a_{\rm in}$	0.16 au	C
$P_{\rm in}$	12.5 days	C
m_2/m_1	0.4	C
(m_1, m_2) $M_\odot$	$(2.29, 0.91)$	C

Table 5.3: Initial parameters corresponding to Cases A to C

Also independently of the RV amplitude, it is possible to extract its modulation frequency:

$$\nu_{\rm in}^{\rm (i)} \equiv \sqrt{\frac{G(m_1+m_2)}{a_{\rm in}^{\rm (i)3}}}. \tag{5.2}$$

Thus if the modulation is detected, one can estimate the semi-major axis of the inner binary, $a_{\rm in}$, from $\nu_{\rm in}$ combined with the total mass of the inner bodies $m_1 + m_2$.

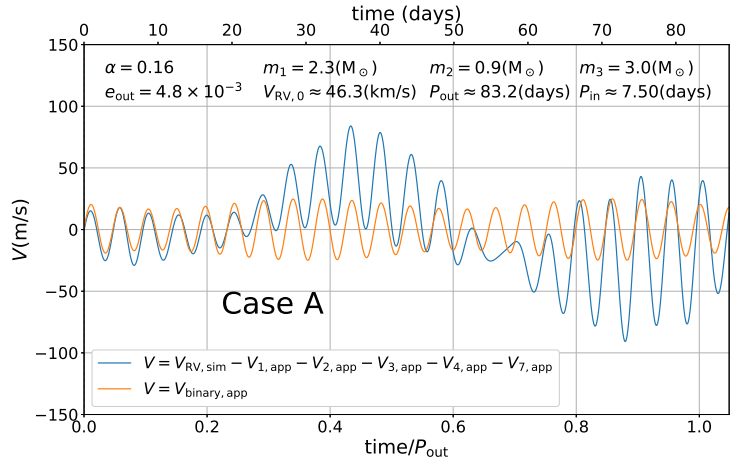

(a)

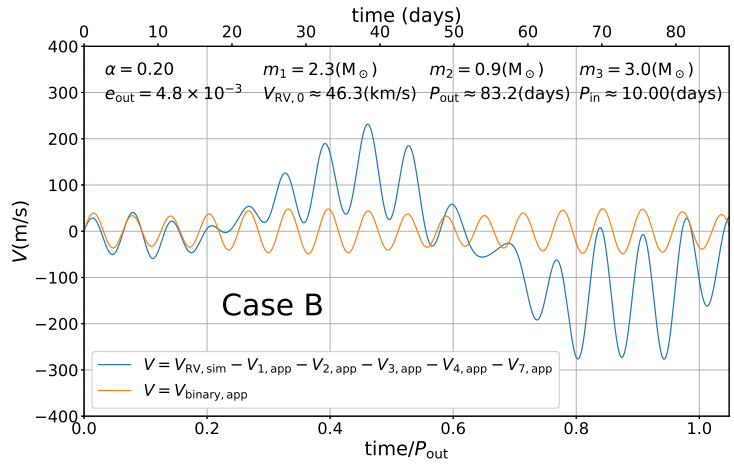

(b)

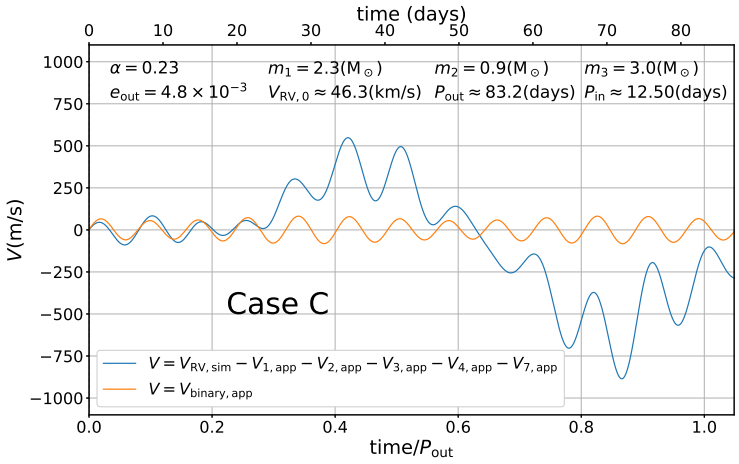

(c)

Figure 5.2: Comparison of our approximate formulae against numerical simulation for the system 2M05215658+4359220 assuming the initial parameters shown in Tables 5.2 and 5.3: (a) Case A, (b) Case B, and (c) Case C.

Chapter 6

Conclusion and future prospect

After LIGO found several close-in binary black-hole systems, many models have been proposed to explain the formation of such objects (e.g. Belczynski et al. 2012, 2016, 2002, 2007; Bird et al. 2016; Dominik et al. 2012, 2013; Kinugawa et al. 2014, 2016; O'Leary et al. 2009; Portegies Zwart & McMillan 2000; Rodriguez et al. 2016; Sasaki et al. 2016, 2018; Tagawa et al. 2016). These scenarios usually assume the presence of progenitor wide-separation binary black holes, but they are still undetected.

In this thesis, we have developed a methodology to search for an unseen inner binary from the precise orbital motion of the outer body. We focused on a three-body system with coplanar near-circular orbits, and derived analytic perturbation formulae of the orbital elements for the outer body. We have confirmed the validity of our analytic formulae using numerical simulation.

While these formulae are expected to be applicable for a variety of observational data, we have examined the radial velocity of the outer body as one of the most feasible methods, and put a constraint on the binary system 2M05215658+4359220 recently discovered by Thompson et al. (2018). If the central object inside the system consists of a binary black hole with roughly equal masses, even the current data turned out to exclude the the inner binary with more than 12.5 day orbital period. Future precise RV follow-up observations of this system will either strengthen the constraint or even detect a signature of the inner binary.

Although our current study assumes a fairly idealized configuration, there are a couple of known systems that are consistent with the assumption, and more importantly, our current analytic model will provide a useful analytic constraint on the system parameter before performing intensive systematic parameter searches using numerical simulations. This will be particularly useful because *Gaia* and *TESS* are expected to identify $\sim 10^3$ binaries in the future.

There should be future opportunities relevant for our methodology presented in this thesis. Since it is likely that most of the systems that *Gaia* or *TESS* would discover are not in coplanar near-circular orbits, it is important to generalize our formulae for eccentric and non-coplanar systems. Specifically, the dynamical formation scenario (e.g. O'Leary et al. 2009; Portegies Zwart & McMillan 2000; Rodriguez et al. 2016; Tagawa et al. 2016) may provide relatively wider and eccentric binary black

holes. Thus, this kind of generalization is quite important to test each formation scenario through observation. We can study these eccentric systems combining both perturbative approach and systematic numerical simulations.

Besides, in order to accelerate merger time (e.g. Antonini et al. 2014; Blaes et al. 2002; Miller & Hamilton 2002; Silsbee & Tremaine 2017; Thompson 2011) and explain spin-orbit misalignment (e.g. Liu & Lai 2017, 2018) implied by LIGO observation, the Lidov - Kozai oscillations (LK oscillations) (Kozai 1962; Lidov 1962) is discussed widely as a possible origin. In this scenario, eccentricity and inclination oscillations induced by the LK oscillations lead to highly eccentric orbits and chaotic evolution of black hole spin axes in a mutually inclined hierarchical triple system. In order to test the feasibility of this scenario, it will be important to find inclined and eccentric compact binaries with a tertiary since the systems possibly undergo the LK oscillations. Generalizing our methodology for finite eccentricity and inclination will also help for this purpose.

In addition, it may be useful to consider also an unbound configuration ($e > 1$) to increase the chance of applications. While the number of triple may be limited, there is a possibility that stars pass beside unseen binaries more frequently. If *Gaia* detects an anomalous motion of star, it will be possible that RV follow-up later finds the unseen objects including compact binaries. This method is used to estimate the internal structure of satellites in the solar system during fly-bys of space probes (e.g. Rappaport et al. 2001). Rappaport et al. (2001) will provide a good resource to extend our methodology although it requires slight changes.

Finally, application to other class of objects may also be promising. Since this methodology is equally applicable to any hierarchical three-body system after slight changes, it is possible to consider broad classes of configurations, including binary planet for example. Ochiai et al. (2014) find that considerable fraction of planetary systems containing giant planets form binary planets though planet - planet scattering and tidal interacrtions. Lewis et al. (2015) discuss the detectablity of them with transit method. Although the RV modulations of host star due to binary planets are usually small as already mentioned in Lewis et al. (2015), it may be possible to detect them depending on the configuration. During the last two decades after the first discovery of exoplanet, many unexpected planets have been discovered including hot jupiters, significantly misaligned system, etc. Therefore it is also worth considering the detection of binary planet through the methodology presented in this thesis.

Apart from the extention of our methodology, it is also practical to perform mock observations with noises using numerical simulation for a variety of parameter sets. It is important to understand what condition is required for parameters and noise levels to distinguish a single black hole and binary black hole from realistic observation. Applying our methodology to data from mock observation and performing realistic data analyses, we should study how accurately we can reconstruct orbital parameters of binary black holes in a variety of condition with current and near future radial velocity instruments.

Acknowledgments

I would like to express my gratitude to supervisor Yasushi Suto for his advice on research and discussion during seminars. Although this research faced many difficulties, he always gave good advice and possible way to overcome these difficulties. I am also grateful to my collaborator Shijie Wang for his help and working together. I thank to Makiko Nagasawa and Re'em Sari for discussion on dynamical evolution of multi-body systems and giving comments on our study. I also would like to thank to Kazuhiro Kanagawa, Shoya Kamiaka, Masataka Aizawa, and Yuta Nakagawa for giving me great insight on planetary physics during seminar. I am grateful to all other members belonging to the University of Tokyo Theoretical Astrophysics (UTAP) and Research Center for the Early Universe (RESCEU) for many good comments on this study and thesis. Finally, I express thank to my family for supporting my life.

Appendix A

The Hansen coefficients

A.1 Calculating the Hansen coefficients

In order to obtain an appropreate disturbing function $\mathcal{R}$, it is required to calculate the Hansen coefficients depending on the order of eccentricities we consider. In this section, we list up the values of them we use to derive the approximate formulae in the main part of this thesis. The following discussion usually follows Mardling (2013) and Hughes (1981).

The Hansen coefficients are defined as

$$X_n^{l,m}(e_{\rm in}) \equiv \frac{1}{2\pi}\int_0^{2\pi}\left(\frac{r}{a_{\rm in}}\right)^l {\rm e}^{{\rm i}mf_{\rm in}}{\rm e}^{-{\rm i}nM_{\rm in}}dM_{\rm in} \tag{A.1}$$

and

$$X_{n'}^{-(l+1),m}(e_{\rm out}) \equiv \frac{1}{2\pi}\int_0^{2\pi}\left(\frac{R}{a_{\rm out}}\right)^{-(l+1)} {\rm e}^{-{\rm i}mf_{\rm out}}{\rm e}^{{\rm i}n'M_{\rm out}}dM_{\rm out}. \tag{A.2}$$

In order to obtain the approximate disturbing function, it is required to compute the Hansen coefficients explicitly. This procedure is done as follows. Using the inner and outer eccentric anomalies $E_{\rm in}$ and $E_{\rm out}$,

$$r = a_{\rm in}(1-e_{\rm in}\cos E_{\rm in}),\ R = a_{\rm out}(1-e_{\rm out}\cos E_{\rm out}), \tag{A.3}$$

$$M_{\rm in} = E_{\rm in} - e_{\rm in}\sin E_{\rm in},\ M_{\rm out} = E_{\rm out} - e_{\rm out}\sin E_{\rm out}, \tag{A.4}$$

$$\sin f_{\rm in} = \frac{\sqrt{1-e_{\rm in}^2}\sin E_{\rm in}}{1-e_{\rm in}\cos E_{\rm in}},\ \sin f_{\rm out} = \frac{\sqrt{1-e_{\rm out}^2}\sin E_{\rm out}}{1-e_{\rm out}\cos E_{\rm out}}, \tag{A.5}$$

$$\cos f_{\rm in} = \frac{\cos E_{\rm in} - e_{\rm in}}{1-e_{\rm in}\cos E_{\rm in}},\ \cos f_{\rm out} = \frac{\cos E_{\rm out} - e_{\rm out}}{1-e_{\rm out}\cos E_{\rm out}}, \tag{A.6}$$

$$dM_{\rm in} = dE_{\rm in}(1-e_{\rm in}\cos E_{\rm in}) = dE_{\rm in}\left(\frac{r}{a_{\rm in}}\right), \tag{A.7}$$

and

$$dM_{\rm out} = dE_{\rm out}(1-e_{\rm out}\cos E_{\rm out}) = dE_{\rm out}\left(\frac{R}{a_{\rm out}}\right). \tag{A.8}$$

Therefore, the Hansen coefficients can be rewritten as

$$\begin{aligned} X_n^{l,m}(e_{\rm in}) &= \frac{1}{2\pi}\int_0^{2\pi} r^{l+1}(\cos f_{\rm in} + {\rm i}\sin f_{\rm in})^m {\rm e}^{-{\rm i}n(E_{\rm in}-e_{\rm in}\sin E_{\rm in})} dE_{\rm in} \\ &= \frac{1}{2\pi}\int_0^{2\pi} dE_{\rm in}(1-e_{\rm in}\cos E_{\rm in})^{l+1} \\ &\times \left(\frac{\cos E_{\rm in}-e_{\rm in}}{1-e_{\rm in}\cos E_{\rm in}} + {\rm i}\frac{\sqrt{1-e_{\rm in}^2}\sin E_{\rm in}}{1-e_{\rm in}\cos E_{\rm in}}\right)^m {\rm e}^{-{\rm i}n(E_{\rm in}-e_{\rm in}\sin E_{\rm in})} \end{aligned} \tag{A.9}$$

and

$$\begin{aligned} X_{n'}^{-(l+1),m}(e_{\rm out}) &= \frac{1}{2\pi}\int_0^{2\pi} R^{-l}(\cos f_{\rm out} - {\rm i}\sin f_{\rm out})^m {\rm e}^{{\rm i}n'(E_{\rm out}-e_{\rm out}\sin E_{\rm out})} dE_{\rm out} \\ &= \frac{1}{2\pi}\int_0^{2\pi} dE_{\rm out}(1-e_{\rm out}\cos E_{\rm out})^{-l} \\ &\times \left(\frac{\cos E_{\rm out}-e_{\rm out}}{1-e_{\rm out}\cos E_{\rm out}} - {\rm i}\frac{\sqrt{1-e_{\rm out}^2}\sin E_{\rm out}}{1-e_{\rm out}\cos E_{\rm out}}\right)^m {\rm e}^{{\rm i}n'(E_{\rm out}-e_{\rm out}\sin E_{\rm out})}. \end{aligned} \tag{A.10}$$

If we expand the integrants in equations (A.9) and (A.10) with respect to $e_{\rm in}$ and $e_{\rm out}$ up to the order we consider, we can obtain the approximate values of the Hansen coefficients explicitly. It is known that the the leading order of the Hansen coefficients are (e.g. Hughes 1981)

$$X_n^{l,m}(e_{\rm in}) = \mathcal{O}(e_{\rm in}^{|m-n|}) \tag{A.11}$$

and

$$X_{n'}^{-(l+1),m}(e_{\rm out}) = \mathcal{O}(e_{\rm out}^{|m-n'|}). \tag{A.12}$$

A.2 The list of the Hansen coefficients

In Chapter 3, we neglect the higher order terms than $\mathcal{O}(e^2)$. Thus, the required Hansen coefficients are up to $\mathcal{O}(e)$. Considering equations (A.11) and (A.12), it is enough to consider $|m-n|, |m-n'| < 2$ up to $\mathcal{O}(e_{\rm in})$ and $\mathcal{O}(e_{\rm out})$ for this procedure. The following is the list of the Hansen coefficients with $l = 2$ to $\mathcal{O}(e_{\rm in})$ and $\mathcal{O}(e_{\rm out})$.

$$X_0^{2,0}(e_{\rm in}) = 1 \tag{A.13}$$
$$X_1^{2,0}(e_{\rm in}) = -e_{\rm in} \tag{A.14}$$
$$X_{-1}^{2,0}(e_{\rm in}) = -e_{\rm in} \tag{A.15}$$
$$X_2^{2,2}(e_{\rm in}) = 1 \tag{A.16}$$
$$X_1^{2,2}(e_{\rm in}) = -3e_{\rm in} \tag{A.17}$$
$$X_3^{2,2}(e_{\rm in}) = e_{\rm in} \tag{A.18}$$
$$X_0^{-(2+1),0}(e_{\rm out}) = 1 \tag{A.19}$$
$$X_1^{-(2+1),0}(e_{\rm out}) = \frac{3}{2}e_{\rm out} \tag{A.20}$$
$$X_{-1}^{-(2+1),0}(e_{\rm out}) = \frac{3}{2}e_{\rm out} \tag{A.21}$$
$$X_2^{-(2+1),2}(e_{\rm out}) = 1 \tag{A.22}$$
$$X_1^{-(2+1),2}(e_{\rm out}) = -\frac{1}{2}e_{\rm out} \tag{A.23}$$
$$X_3^{-(2+1),2}(e_{\rm out}) = \frac{7}{2}e_{\rm out} \tag{A.24}$$

Substituting these equations into disturbing function $\mathcal{R}$ (see equation (3.179)), we obtain the approximate disturbing function used in this thesis.

Appendix B

Full comparison with numerical simulation

The following figures show the comparison between each mode in approximation and the data from numerical simulation after subtracting the previous mode one by one. All parameters used in this section are summarized in Table 4.3 and each RV mode is listed in Table 4.2.

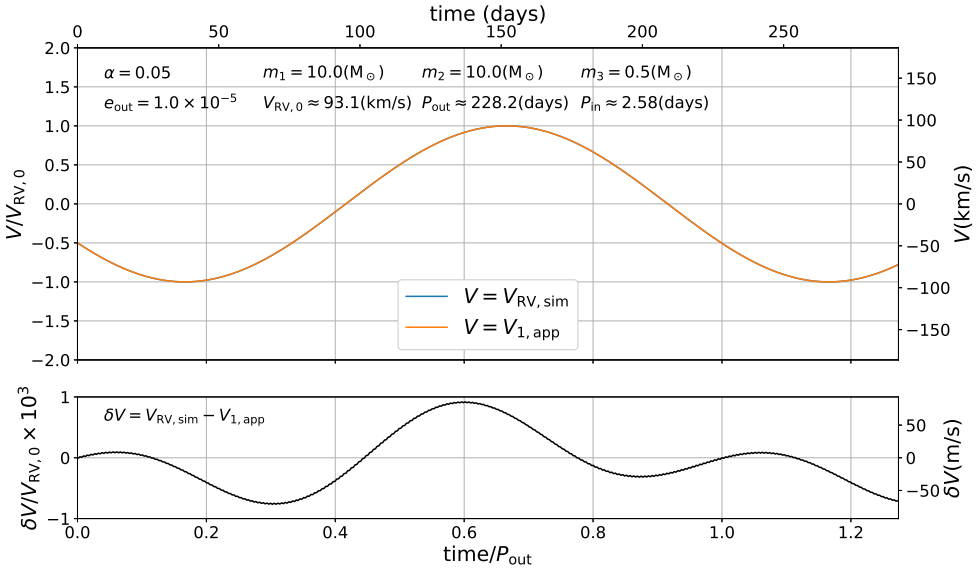

Figure B.1: Comparison of $V_{\mathrm{RV,sim}}$ against $V_{\mathrm{1,app}}$ for a system with initial parameters listed in Table 4.3.

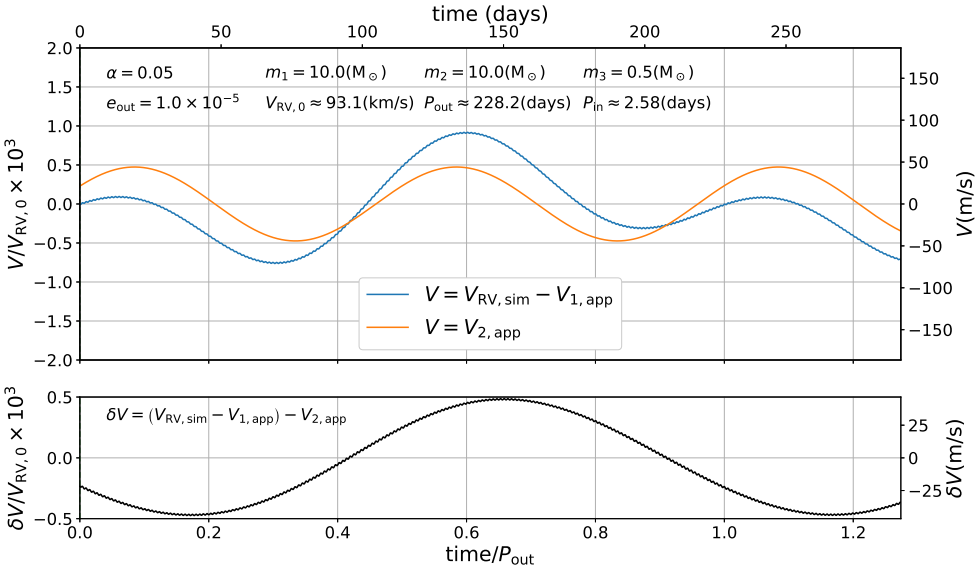

Figure B.2: Same as Figure B.1 but for $V_{\mathrm{RV,sim}} - V_{1,\mathrm{app}}$ against $V_{2,\mathrm{app}}$.

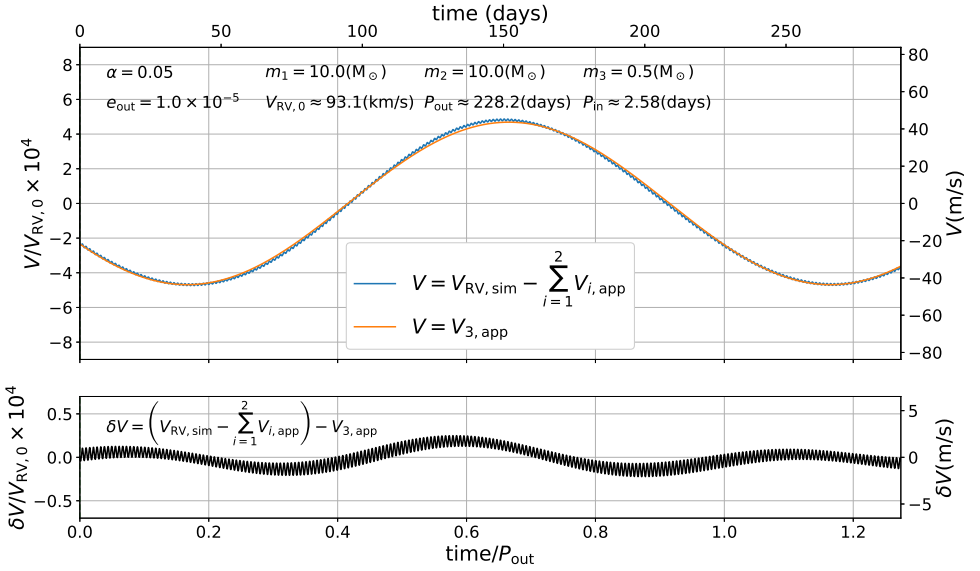

Figure B.3: Same as Figure B.2 but for $V_{\mathrm{RV,sim}} - \sum_{i=1}^{2} V_{i,\mathrm{app}}$ against $V_{3,\mathrm{app}}$.

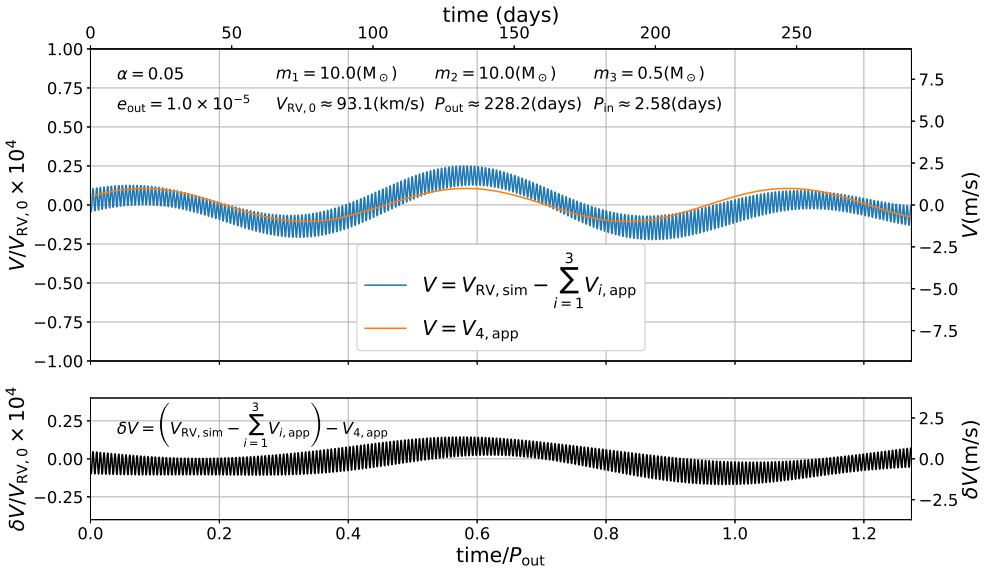

Figure B.4: Same as Figure B.2 but for $V_{\mathrm{RV,sim}} - \sum_{i=1}^{3} V_{i,\mathrm{app}}$ against $V_{4,\mathrm{app}}$.

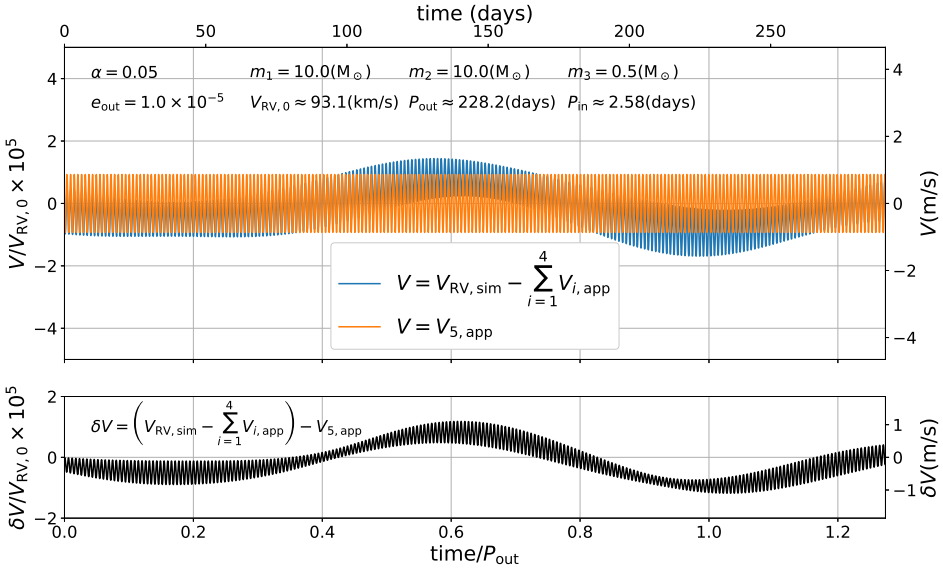

Figure B.5: Same as Figure B.2 but for $V_{\mathrm{RV,sim}} - \sum_{i=1}^{4} V_{i,\mathrm{app}}$ against $V_{5,\mathrm{app}}$.

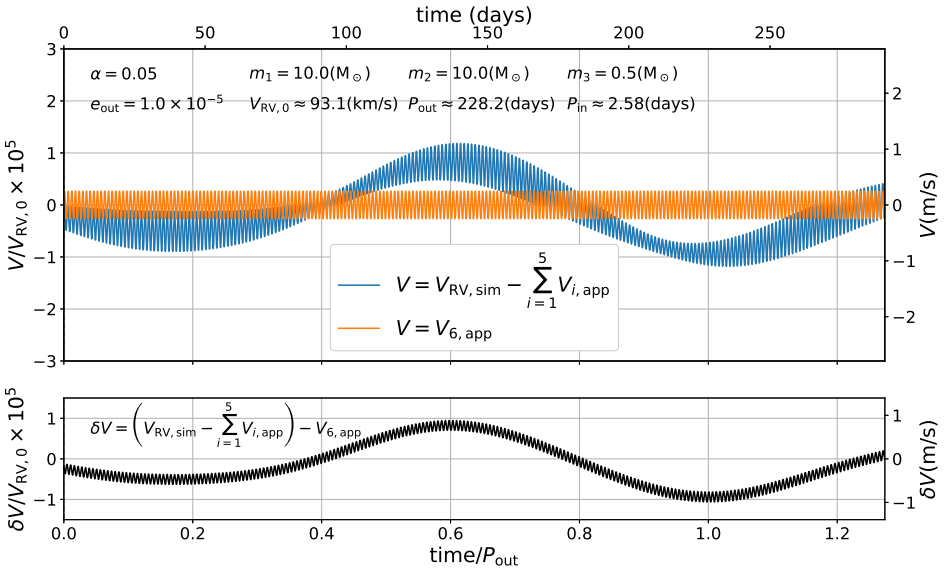

Figure B.6: Same as Figure B.2 but for $V_{\mathrm{RV,sim}} - \sum_{i=1}^{5} V_{i,\mathrm{app}}$ against $V_{6,\mathrm{app}}$.

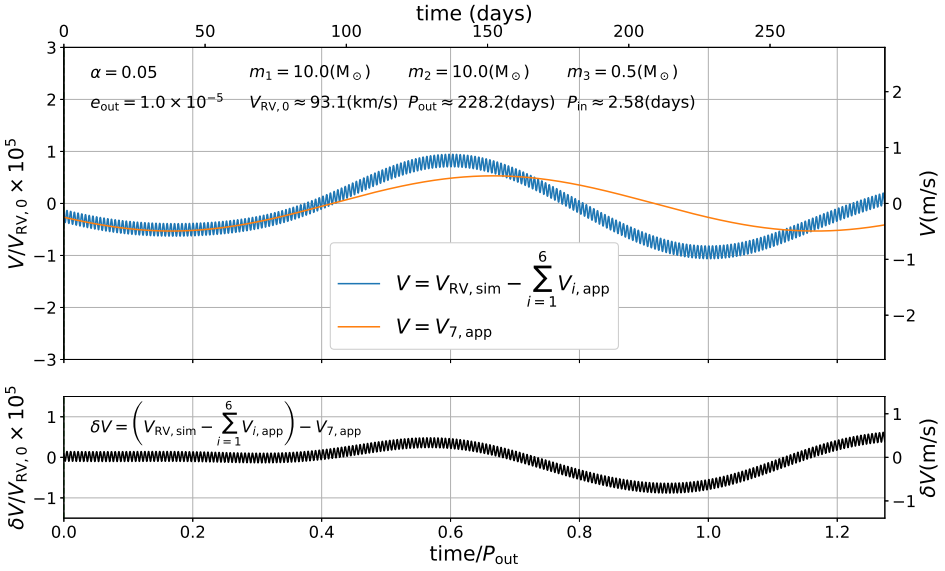

Figure B.7: Same as Figure B.2 but for $V_{\mathrm{RV,sim}} - \sum_{i=1}^{6} V_{i,\mathrm{app}}$ against $V_{7,\mathrm{app}}$.

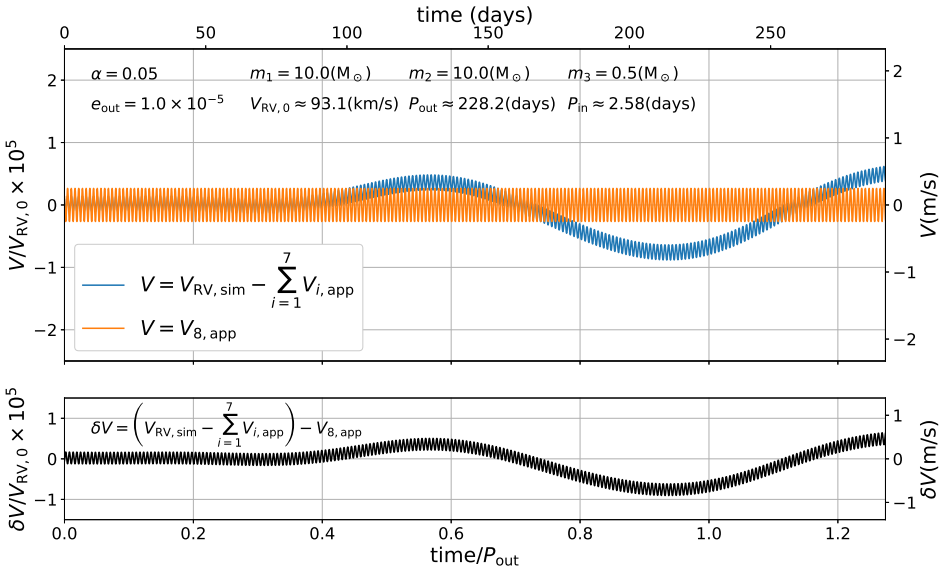

Figure B.8: Same as Figure B.2 but for $V_{\mathrm{RV,sim}} - \sum_{i=1}^{7} V_{i,\mathrm{app}}$ against $V_{8,\mathrm{app}}$.

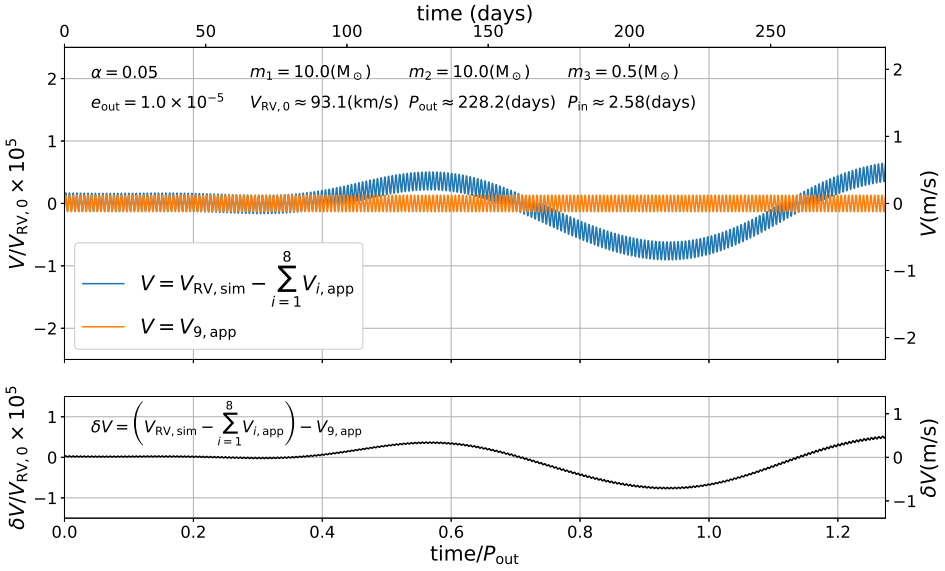

Figure B.9: Same as Figure B.2 but for $V_{\mathrm{RV,sim}} - \sum_{i=1}^{8} V_{i,\mathrm{app}}$ against $V_{9,\mathrm{app}}$.

Appendix C

Derivation of the Lagrange planetary equations using variation of constants

We previously used the Hamilton - Jacobi equation to derive the Lagrange planetary equations. Here, we consider another method called variation of constants for derivation. The detail discussion is available in many standard textbooks in celestial mechanics. This section normally follows the descripsion in Kinoshita (2007). Consider a Hamiltonian $\mathcal{H}$ written as

$$\mathcal{H} = \mathcal{H}_{\rm Kep} - \mathcal{R}, \tag{C.1}$$

where $\mathcal{H}_{\rm Kep}$ is a Hamiltonian describing the Keplerian motion, and $\mathcal{R}$ is a disturbing function. The canonical equations of motion are

$$\dot{q}_i = \frac{\partial \mathcal{H}}{\partial p_i} = \frac{\partial \mathcal{H}_{\rm Kep}}{\partial p_i} - \frac{\partial \mathcal{R}}{\partial p_i} \quad (i = 1, 2, 3) \tag{C.2}$$

and

$$\dot{p}_i = -\frac{\partial \mathcal{H}}{\partial q_i} = -\frac{\partial \mathcal{H}_{\rm Kep}}{\partial q_i} + \frac{\partial \mathcal{R}}{\partial q_i} \quad (i = 1, 2, 3), \tag{C.3}$$

where q_i are canonical coordinates, and p_i are corresponding momenta. Considering the result for a two-body problem, if $\mathcal{R} = 0$, the solutions can be written by constant 6 orbital elements and time,

$$q_i = f_i(\boldsymbol{c}, t), \quad p_i = g_i(\boldsymbol{c}, t) \quad (i = 1, 2, 3), \tag{C.4}$$

where f_i and g_i are solution functions, t is time, and $\boldsymbol{c} \equiv (c_1, c_2, c_3, c_4, c_5, c_6)$ is a set of 6 orbital elements. While $\boldsymbol{c}$ is constant in pure two-body problem, it varies with time if the perturbations exist. In this case, the time derivative of q_i and p_i are

$$\frac{dq_i}{dt} = \frac{\partial f_i}{\partial t} + \sum_{j=1}^{6} \frac{\partial f_i}{\partial c_j} \dot{c}_j \tag{C.5}$$

and

$$\frac{dp_i}{dt} = \frac{\partial g_i}{\partial t} + \sum_{j=1}^{6} \frac{\partial g_i}{\partial c_j}\dot{c}_j. \tag{C.6}$$

In order for $\boldsymbol{c}$ to denote the osculating elements, we can use the following relations:

$$\frac{\partial f_i}{\partial t} = \frac{\partial \mathcal{H}_{\mathrm{Kep}}}{\partial p_i}, \quad \frac{\partial g_i}{\partial t} = -\frac{\partial \mathcal{H}_{\mathrm{Kep}}}{\partial q_i} \quad (i = 1, 2, 3). \tag{C.7}$$

Substituting equations (C.5) - (C.7) into equations (C.2) and (C.3), we obtain

$$\sum_{j=1}^{6} \frac{\partial f_i}{\partial c_j}\dot{c}_j = -\frac{\partial \mathcal{R}}{\partial p_i}, \quad \sum_{j=1}^{6} \frac{\partial g_i}{\partial c_j}\dot{c}_j = \frac{\partial \mathcal{R}}{\partial q_i} \quad (i = 1, 2, 3). \tag{C.8}$$

After some calculations, equation (C.8) reduces to

$$\sum_{j=1}^{6} [c_i, c_j]\dot{c}_j = \frac{\partial \mathcal{R}}{\partial c_i} \quad (i = 1, 2, 3, 4, 5, 6). \tag{C.9}$$

In equation (C.9), $[c_i, c_j]$ is called the "Lagrange bracket" and defined as

$$[c_i, c_j] = \sum_{k=1}^{3} \left(\frac{\partial f_k}{\partial c_i}\frac{\partial g_k}{\partial c_j} - \frac{\partial g_k}{\partial c_i}\frac{\partial f_k}{\partial c_j} \right). \tag{C.10}$$

Here, consider taking $(a, \varpi, e, \Omega, \tilde{\epsilon}, I)$ as a set of 6 orbital elements. In general, if we take an arbitrary canonical coordinates, calculating the Lagrange brackets requires tedious work. Thus, we consider using the Delauney variables as canonical coordinates here:

$$\begin{pmatrix} q_1 \\ q_2 \\ q_3 \\ p_1 \\ p_2 \\ p_3 \end{pmatrix} = \begin{pmatrix} M \\ \omega \\ \Omega \\ \mu\sqrt{Gm_{\mathrm{tot}}a} \\ \mu\sqrt{Gm_{\mathrm{tot}}a(1-e^2)} \\ \mu\sqrt{Gm_{\mathrm{tot}}a(1-e^2)}\cos I \end{pmatrix} = \begin{pmatrix} \nu t + \tilde{\epsilon} - \varpi \\ \varpi - \Omega \\ \Omega \\ \mu\sqrt{Gm_{\mathrm{tot}}a} \\ \mu\sqrt{Gm_{\mathrm{tot}}a(1-e^2)} \\ \mu\sqrt{Gm_{\mathrm{tot}}a(1-e^2)}\cos I \end{pmatrix}. \tag{C.11}$$

Then, we obtain the values of the Lagrange brackets as follows:

$$[a, \varpi] = -[\varpi, a] = \frac{1}{2}\mu\nu a(1 - \sqrt{1-e^2}), \tag{C.12}$$

$$[a, \Omega] = -[\Omega, a] = \frac{1}{2}\mu\nu a\sqrt{1-e^2}(1 - \cos I), \tag{C.13}$$

$$[a, \tilde{\epsilon}] = -[\tilde{\epsilon}, a] = -\frac{1}{2}\mu\nu a, \tag{C.14}$$

$$[\varpi, e] = -[e, \varpi] = -\frac{\mu\nu a^2 e}{\sqrt{1-e^2}}, \tag{C.15}$$

$$[e, \Omega] = -[\Omega, e] = \frac{\mu\nu a^2 e}{\sqrt{1-e^2}}(\cos I - 1), \tag{C.16}$$

$$[\Omega, I] = -[I, \Omega] = -\mu\nu a^2\sqrt{1-e^2}\sin I, \tag{C.17}$$

where ν is the mean motion. The other components of the Lagrange brackets have zero values. Substituting these into the equation (C.9),

$$\frac{1}{2}\mu\nu a(1-\sqrt{1-e^2})\dot{\varpi} + \frac{1}{2}\mu\nu\sqrt{1-e^2}(1-\cos I)\dot{\Omega} - \frac{1}{2}\mu\nu a\dot{\tilde{\epsilon}} = \frac{\partial\mathcal{R}}{\partial a}, \tag{C.18}$$

$$-\frac{1}{2}\mu\nu a(1-\sqrt{1-e^2})\dot{a} - \frac{\mu\nu a^2 e}{\sqrt{1-e^2}}\dot{e} = \frac{\partial\mathcal{R}}{\partial\varpi}, \tag{C.19}$$

$$\frac{\mu\nu a^2 e}{\sqrt{1-e^2}}\dot{\varpi} + \frac{\mu\nu a^2 e}{\sqrt{1-e^2}}(\cos I - 1)\dot{\Omega} = \frac{\partial\mathcal{R}}{\partial e}, \tag{C.20}$$

$$-\frac{1}{2}\mu\nu a\sqrt{1-e^2}(1-\cos I)\dot{a} + \frac{\mu\nu a^2 e}{\sqrt{1-e^2}}(1-\cos I)\dot{e} - \mu\nu a^2\sqrt{1-e^2}\sin I\dot{I} = \frac{\partial\mathcal{R}}{\partial\Omega}, \tag{C.21}$$

$$\frac{1}{2}\mu\nu a\dot{a} = \frac{\partial\mathcal{R}}{\partial\tilde{\epsilon}}, \tag{C.22}$$

and

$$\mu\nu a^2\sqrt{1-e^2}\sin I\dot{\Omega} = \frac{\partial\mathcal{R}}{\partial I}. \tag{C.23}$$

Note that it is necessary to consider implicit a dependence on ν when evaluating $\frac{\partial\mathcal{R}}{\partial a}$ here. Since ν dependence in $\mathcal{R}$ is always inside $\lambda \equiv \nu t + \tilde{\epsilon}$ in celestial mechanics,

$$\frac{\partial}{\partial\tilde{\epsilon}} = \frac{\partial}{\partial\lambda} \tag{C.24}$$

and

$$\frac{\partial\mathcal{R}}{\partial a} = \left(\frac{\partial\mathcal{R}}{\partial a}\right)_\nu + \frac{\partial\mathcal{R}}{\partial\lambda}t\frac{\dot{\nu}}{\dot{a}}, \tag{C.25}$$

where $\left(\frac{\partial\mathcal{R}}{\partial a}\right)_\nu$ is the a derivative of $\mathcal{R}$ with ν fixed. Using equation (C.22), equation (C.25) reduces to

$$\frac{\partial\mathcal{R}}{\partial a} = \left(\frac{\partial\mathcal{R}}{\partial a}\right)_\nu + \frac{\mu\nu a}{2}\dot{\nu}t. \tag{C.26}$$

Therefore, using equations (C.24) and (C.26), equations (C.18) - (C.23) result in the Lagrange planetary equations (3.129) - (3.134). It is possible to avoid a secular term in the Lagrange planetary equations using the same technique as that in Chapter 3.

Bibliography

Abbott, B. P., Abbott, R., Abbott, T. D., et al. 2016, Physical Review Letters, 116, 061102

Antonini, F., Murray, N., & Mikkola, S. 2014, ApJ, 781, 45

Belczyński, K., & Bulik, T. 1999, A&A, 346, 91

Belczynski, K., Dominik, M., Repetto, S., Holz, D. E., & Fryer, C. L. 2012, ArXiv e-prints, arXiv:1208.0358

Belczynski, K., Holz, D. E., Bulik, T., & O'Shaughnessy, R. 2016, Nature, 534, 512

Belczynski, K., Kalogera, V., & Bulik, T. 2002, ApJ, 572, 407

Belczynski, K., Taam, R. E., Kalogera, V., Rasio, F. A., & Bulik, T. 2007, ApJ, 662, 504

Binney, J., & Tremaine, S. 2008, Galactic Dynamics: Second Edition (Princeton University Press)

Bird, S., Cholis, I., Muñoz, J. B., et al. 2016, Physical Review Letters, 116, 201301

Blaes, O., Lee, M. H., & Socrates, A. 2002, ApJ, 578, 775

Boquet, F. 1889, Annales de l'Observatoire de Paris, 19, B.1

Breivik, K., Chatterjee, S., & Larson, S. L. 2017, ApJ, 850, L13

Brouwer, D., & Clemence, G. M. 1961, Methods of celestial mechanics

Brown, E. W., & Shook, C. A. 1933, Planetary theory

Danby, J. M. A. 1988, Fundamentals of celestial mechanics

Dominik, M., Belczynski, K., Fryer, C., et al. 2012, ApJ, 759, 52

—. 2013, ApJ, 779, 72

Fryer, C. L., Belczynski, K., Wiktorowicz, G., et al. 2012, ApJ, 749, 91

Gaia Collaboration, Prusti, T., de Bruijne, J. H. J., et al. 2016, A&A, 595, A1

Hagihara, Y. 1970, Celestial mechanics. Vol.1: Dynamical principles and transformation theory

Heggie, D. C. 1975, MNRAS, 173, 729

Hughes, S. 1981, Celestial Mechanics, 25, 101

Jackson, J. D. 1975, Classical electrodynamics

Kaula, W. M. 1962, AJ, 67, 300

Kawanaka, N., Yamaguchi, M., Piran, T., & Bulik, T. 2017, in IAU Symposium, Vol. 324, New Frontiers in Black Hole Astrophysics, ed. A. Gomboc, 41–42

Kinoshita, H. 2007, Tentai to kido no rikigaku (in Japanese), 3rd edn. (University of Tokyo Press)

Kinugawa, T., Inayoshi, K., Hotokezaka, K., Nakauchi, D., & Nakamura, T. 2014, MNRAS, 442, 2963

Kinugawa, T., Miyamoto, A., Kanda, N., & Nakamura, T. 2016, MNRAS, 456, 1093

Kozai, Y. 1962, AJ, 67, 591

Kulkarni, S. R., Hut, P., & McMillan, S. 1993, Nature, 364, 421

Le Verrier, U.-J. 1855, Annales de l'Observatoire de Paris, 1, 258

Lewis, K. M., Ochiai, H., Nagasawa, M., & Ida, S. 2015, ApJ, 805, 27

Lidov, M. L. 1962, Planet. Space Sci., 9, 719

Liu, B., & Lai, D. 2017, ApJ, 846, L11

—. 2018, ApJ, 863, 68

Mardling, R. A. 2013, MNRAS, 435, 2187

Mardling, R. A., & Aarseth, S. J. 2001, MNRAS, 321, 398

Mashian, N., & Loeb, A. 2017, MNRAS, 470, 2611

Masuda, K., & Hotokezaka, K. 2018, ArXiv e-prints, arXiv:1808.10856

Miller, M. C., & Hamilton, D. P. 2002, ApJ, 576, 894

Morris, M. 1993, ApJ, 408, 496

Motalebi, F., Udry, S., Gillon, M., et al. 2015, A&A, 584, A72

Moulton, F. R. 1914, An introduction to celestial mechanics

Murray, C. D. 1985, Celestial Mechanics, 36, 163

Murray, C. D., & Dermott, S. F. 2000, Solar System Dynamics

Newcomb, S. 1895, [United States. Nautical Almanac Office. Astronomical paper ; v.5, pt. 1 (1895)], [Washington : U.S. Nautical Almanac Office, 1895], p. 1-48 ; 30 X 23 cm., 5, 1

Ochiai, H., Nagasawa, M., & Ida, S. 2014, ApJ, 790, 92

O'Leary, R. M., Kocsis, B., & Loeb, A. 2009, MNRAS, 395, 2127

O'Leary, R. M., Rasio, F. A., Fregeau, J. M., Ivanova, N., & O'Shaughnessy, R. 2006, ApJ, 637, 937

Peirce, B. 1849, AJ, 1, 1

Portegies Zwart, S. F., & McMillan, S. L. W. 2000, ApJ, 528, L17

Ransom, S. M., Stairs, I. H., Archibald, A. M., et al. 2014, Nature, 505, 520

Rappaport, N. J., Giampieri, G., & Anderson, J. D. 2001, Icarus, 150, 168

Rodriguez, C. L., Haster, C.-J., Chatterjee, S., Kalogera, V., & Rasio, F. A. 2016, ApJ, 824, L8

Roy, A. E. 2005, Orbital motion

Sasaki, M., Suyama, T., Tanaka, T., & Yokoyama, S. 2016, Physical Review Letters, 117, 061101

—. 2018, Classical and Quantum Gravity, 35, 063001

Silsbee, K., & Tremaine, S. 2017, ApJ, 836, 39

Stassun, K. G., Oelkers, R. J., Pepper, J., et al. 2018, AJ, 156, 102

Sullivan, P. W., Winn, J. N., Berta-Thompson, Z. K., et al. 2015, ApJ, 809, 77

Tagawa, H., Umemura, M., & Gouda, N. 2016, MNRAS, 462, 3812

Thompson, T. A. 2011, ApJ, 741, 82

Thompson, T. A., Kochanek, C. S., Stanek, K. Z., et al. 2018, ArXiv e-prints, arXiv:1806.02751

Valtonen, M., & Karttunen, H. 2006, The Three-Body Problem

Yamaguchi, M. S., Kawanaka, N., Bulik, T., & Piran, T. 2018, ApJ, 861, 21

Zevin, M., Samsing, J., Rodriguez, C., Haster, C.-J., & Ramirez-Ruiz, E. 2018, arXiv e-prints, arXiv:1810.00901